UNIVERSITY OF OKLAHOMA

GRADUATE COLLEGE

CONTROL AND OPTIMIZATION OF VARIABLE-SPEED WIND TURBINES AND LARGE-SCALE WIND FARMS

A DISSERTATION

SUBMITTED TO THE GRADUATE FACULTY

in partial fulfillment of the requirements for the

Degree of

DOCTOR OF PHILOSOPHY

By

YI GUO
Norman, Oklahoma
2012

CONTROL AND OPTIMIZATION OF VARIABLE-SPEED WIND TURBINES AND LARGE-SCALE WIND FARMS

A DISSERTATION APPROVED FOR THE
SCHOOL OF ELECTRICAL AND COMPUTER ENGINEERING

BY

Dr. Choon Yik Tang, Chair

Dr. John S. Greene

Dr. Sesh Commuri

Dr. John N. Jiang

Dr. Rama G. Ramakumar

Dr. Thordur Runolfsson

To my family

Acknowledgements

I would like to express my deepest gratitude to my advisor, Dr. Choon Yik Tang, for his continuous guidance, support, and patience throughout the course of my graduate studies. He has always been there to listen and give insightful advice.

I am grateful to Dr. John S. Greene, Dr. Sesh Commuri, Dr. John N. Jiang, Dr. Rama G. Ramakumar, and Dr. Thordur Runolfsson for their time and effort in serving on my graduate committee. Their invaluable suggestions and recommendations have significantly improved the quality of my research and dissertation.

I want to thank my colleagues, Mr. S. Hossein Hosseini and Ms. Wei Wang, for their kind help during my Ph.D. studies.

Moreover, I wish to thank my parents, Minsheng Guo and Naili Liu, as well as my lovely wife, Jinfeng Wang. Without their unconditional love and selfless support, I would have no chance of achieving all this.

Finally, financial support from the National Science Foundation is gratefully acknowledged.

Table of Contents

List of Tables

List of Figures

Abstract

CONTROL AND OPTIMIZATION OF VARIABLE-SPEED WIND TURBINES AND LARGE-SCALE WIND FARMS

Yi Guo, Ph.D.
The University of Oklahoma, 2012

Supervisor: Choon Yik Tang

Motivated by the vast potential of wind power as a renewable energy source and the reliability issues arising from its integration into a power system, this dissertation designs and analyzes a novel, diverse collection of controllers, which significantly enhance the capability and performance of variable-speed wind turbines and large-scale wind farms.

In the dissertation, we consider a number of key problems and pressing issues in the area and develop, for each of them, a solution based on systems and control theory as well as optimization methods. More specifically, we first devise a nonlinear controller using feedback linearization and a gradient-based approach, which enables wind turbines with doubly fed induction generators to jointly control their active and reactive powers in both the maximum power tracking and power regulation modes. We also extend the controller by incorporating bias estimation and exploiting timescale separation, so that it can cope with turbines with uncertainties, and evaluate our controller via simulations with realistic wind profiles, demonstrating its effectiveness.

Building upon single turbine controllers by other researchers and by us, we next turn to the emerging problem of wind farm power control, in which there is a lack of models that appropriately simplify the complex overall wind farm dynamics. To fill this void, we use system identification approaches to construct a structurally simple, approximate wind turbine control system (WTCS) model, which attempts to mimic the complex active and reactive power dynamics of generic analytical and empirical WTCS models. Through extensive validation, we show that the approximate model is accurate and versatile, capable of closely imitating several WTCS models from the literature and from real data.

Based on the approximate model, we subsequently develop a centralized wind farm controller, which makes the wind farm power output accurately and smoothly track a desired reference from the power grid operator. The wind farm controller is made up of a model predictive controller on the outer loop, which uses various forecasts and feedbacks to iteratively plan the desired power trajectories for optimal tracking, and an adaptive controller on the inner loop, which uses estimated wind speed characteristics to adaptively tune the controller gains for optimal smoothness. We also carry out a series of simulations, which illustrate the salient features of our wind farm controller.

Finally, we study how a wind turbine equipped with a maximum power tracking controller and a proportional inertia response controller may affect the power system frequency from a control standpoint, including the resulting system equilibria, pole-zero locations, and stability properties.

Chapter 1 Introduction

1.1 Background and Motivation

Wind power is gaining ever-increasing attention in recent years as a clean, safe, and renewable energy source. With the fast growth of wind generation in power systems, wind power is becoming a significant portion of the generation portfolio in the United States as well as many countries in Europe and Asia [6]. Indeed, wind power penetration is planned to surpass 20% of the United States' total energy production by 2030—a figure that is way beyond the current level of less than 5% [7]. Hence, to realize this vision, it is necessary to develop large-scale wind farms that effectively produce electric power from wind, and integrate them with the power systems.

The integration of large-scale wind farms into a power system, however, changes the fundamental principle of its operation, which is to maintain reliability by balancing load variation with "controllable" generation resources. When a portion of these resources comes from "uncontrollable" wind generation, that portion of the resources can hardly be guaranteed due to the intermittency of wind. As a result, the power system may fail to achieve the required balance. When the level of wind power penetration is small, this issue may be safely neglected. However, with the anticipated increase in penetration, the issue becomes critical for power system reliability. Therefore, sophisticated control technologies for both wind turbines and wind farms, which enable seamless integration of large-scale wind energy into a power system without affecting its reliability, are highly desirable.

Today, most large-scale wind farms operate in the *maximum power tracking* (MPT) mode, making wind turbines in the farm harvest as much wind energy as they possibly could, following the "let it be when the wind blows" philosophy of operation. Operation in this mode, however, may produce excessive power that destabilizes the grid. As a case in point, when half of the European grids experienced a severe difficulty in 2006, the wind farms operating in the MPT mode complicated the process of returning to normal system conditions [8]. This event took place even though the wind penetration level, at that time, was low at only 6%. Therefore, it is highly desirable that wind farms can also operate in the so-called *power regulation* (PR) mode, whereby its total power output from the wind turbines is continuously and closely regulated at some desired setpoint, despite the fluctuating wind conditions.

The ability to operate in the PR mode in addition to the MPT mode, as well as the ability to *seamlessly* switch between the two, offers many important advantages: not only does the PR mode provide a cushion to absorb the impact of wind fluctuations on the total power output through power regulation, it also enables a power system to effectively respond to changes in reliability conditions and economic signals. For instance, during system contingencies in which a sudden drop in load occurs, the power system may ask the wind farm to switch from the MPT to the PR mode and generate less power, rather than rely on expensive down-regulation generation. As another example, the PR mode, when properly designed, allows the power output of a wind farm to smoothly and accurately follow system dispatch requests, thus reducing its reliance on ancillary services such as reliability reserves.

To enable large-scale wind farms to operate well in these two modes and switch seamlessly between them while maintaining a desired power factor, a high-performance individual wind turbine controller is essential. A key challenge facing the development of such a controller is the fact that the mechanical and electrical parts of a wind turbine with a Doubly Fed Induction Generator (DFIG)—which is the prevalent generator used today—are tightly coupled. Nevertheless, most studies have adopted a standard approach in the analysis and control of synchronous electric machines, where the active and reactive powers are considered decoupled. With this approach, the active and reactive powers are adjusted via control of the mechanical and electrical parts, respectively, independent of each other. However, although a DFIG has some features of a synchronous machine, it is by nature an induction machine with strong electromechanical coupling among its rotor excitation current, rotor angular velocity, and electromagnetic torque. Hence, for performance reasons, both the mechanical and electrical parts should be considered synergistically in controller design.

Another major challenge is the fact that the aerodynamic and mechanical parameters of a wind turbine are inherently uncertain, due to modeling and measurement errors and other ambient factors. For example, the so-called C_p-surface of a wind turbine is typically assumed to be known—or, at least, its optimal point is assumed to be known—in many existing controller designs. Unfortunately, such a surface is an empirical, statistical approximation, obtained based on long-term experiments [9]. Thus, it may not be precisely known for control purposes. Other factors, such as changes in air density and friction due to weather, and measurement errors due to anemometer location, also contribute to the uncertainties. Indeed, a report from the National Renewable

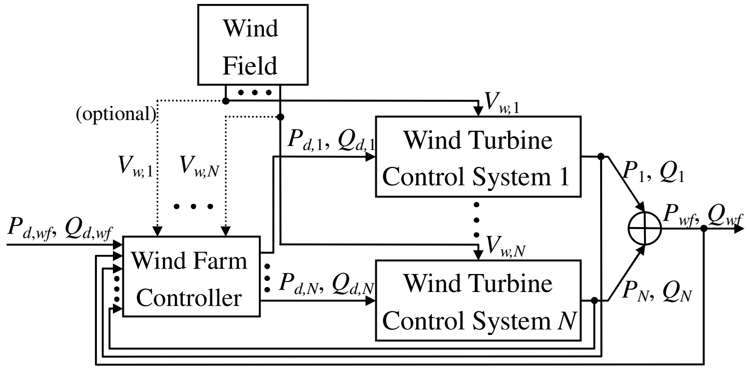

Figure 1.1: Hierarchical architecture of a wind farm control system.

Energy Laboratory (NREL) [10] shows that the impact of these uncertainties on wind turbine controller performance is significant and should be accounted for in the design stage.

On wind farm level, being able to control a wind farm so that its power output is cooperatively maximized, or smoothly regulated, is imperative to successful and reliable integration of large-scale wind generation into the power grid. The design of a sophisticated *wind farm control system* (WFCS) for such control, however, is challenging for a variety of reasons. First, a wind turbine, by itself, is already a fairly complex system with highly nonlinear dynamics, strong electromechanical coupling, inherently uncertain parameters, and multiple control variables. Second, when hundreds of such turbines are immersed in a wind field across a geographical region, they produce turbulence and wake effects that affect downstream turbines, causing their overall behavior to be complicated. Third, the large number of control variables to simultaneously handle, and the rich set of approaches to possibly use, further compound the complexity.

One way to cope with the complexities is to introduce a hierarchical architecture, which as shown in Figure 1.1 divides a WFCS into two parts:

a central *wind farm controller* (WFC) and N individual *wind turbine control systems* (WTCSs), each comprising a wind turbine and its controller. With this architecture, we may first design, for each $i \in \{1, 2, \ldots, N\}$, a WTCS i that tries to regulate its millisecond-to-second-timescale active and reactive power outputs P_i and Q_i at some desired $P_{d,i}$ and $Q_{d,i}$, regardless of its incoming wind speed $V_{w,i}$. Upon completion, we may then design a WFC that tries to regulate the second-to-minute-timescale wind farm power outputs $P_{wf} \triangleq \sum_{i=1}^{N} P_i$ and $Q_{wf} \triangleq \sum_{i=1}^{N} Q_i$ at some desired $P_{d,wf}$ and $Q_{d,wf}$, presumably from a grid operator, by adjusting the $P_{d,i}$'s and $Q_{d,i}$'s based on feedback of the P_i's and Q_i's and possibly estimates of the $V_{w,i}$'s. Hence, the architecture simplifies the design of a WFCS, allowing us to sequentially tackle two (seemingly) easier problems on different timescales, as opposed to tackling a harder one. The architecture also offers us the option of designing a new single-turbine controller for each WTCS i, or applying an existing one that accepts $P_{d,i}$ and $Q_{d,i}$ as inputs[1]. Furthermore, it allows us to view the WFC as a second-to-minute-timescale supervisor that tells every WTCS i how much power to generate, and focus on its design without delving too much into millisecond-to-second, turbine-level details.

Although the hierarchical architecture makes the problem more manageable, it does not remove the fact that each WTCS—being a composition of an already-complex wind turbine and a possibly-complicated controller—typically has complex dynamics. As a result, the subsequent design and analysis of a supervisory WFC may prove to be difficult, depending on our goal: if we are content with a simple design (e.g., distribute $P_{d,wf}$ and $Q_{d,wf}$ evenly among

---

[1] Single-turbine controllers that do not accept $P_{d,i}$ and $Q_{d,i}$, such as those that always attempt maximum power tracking, may not fit well with this architecture.

the $P_{d,i}$'s and $Q_{d,i}$'s, or $P_{d,wf}$ proportionally based on the $V_{w,i}$'s) and a basic analysis (e.g., simulation studies only), then how complex a WTCS is probably does not matter. However, if we aim for a nifty design (e.g., adjust the $P_{d,i}$'s and $Q_{d,i}$'s so that the WTCSs can exploit their correlation, interaction, and/or diversity to cooperatively achieve faster transient responses and better steady-state smoothness in P_{wf} and Q_{wf}) and a deeper analysis and understanding (e.g., theoretical characterization of the resulting transient and steady-state behaviors), then an overly complex WTCS may render the process very difficult or even impossible. Therefore, to achieve the latter, it is necessary to build a suitably simplified WTCS model, based on which a high-performing WFC may be developed.

Another pressing issue that has attracted considerable research attention in recent years is the potential of variable-speed wind turbines in providing short-term frequency support through inertia response—a task that currently is being carried out by conventional synchronous generators. Although the benefit and challenge of incorporating inertia response have already been addressed, a number of questions remain open from a control perspective, such as what are the equilibrium points of the resulting system, whether they are asymptotically stable or not, and how the power system frequency behaves with new control design. Answers to these questions are of interest and would serve as complement to other research efforts on wind power.

1.2 Literature Review

To date, a significant amount of research has been performed on control of variable-speed wind turbines. To streamline the review of the current literature, we note that variable-speed wind turbines typically have three different regions of operation: *Region 1* corresponds to a turbine that is starting up or winding down; *Region 2* corresponds to the normal operating region where the wind speed is below the rated value and the typical objective is to maximize turbine power output (i.e., the MPT mode); and *Region 3* corresponds to the region where the wind speed is above the rated value, so that the turbine must limit the captured wind power to ensure safe electrical and mechanical operations. With these three regions defined, we provide below a review of the current literature.

For operation in Region 2, several MPT algorithms have been proposed in the literature, which can be broadly classified into the following types:

(a) *Tip-Speed-Ratio Control.* The power coefficient C_p of a wind turbine is a function $C_p(\lambda, \beta)$ of the tip speed ratio λ and the blade pitch angle β. For most wind turbines, the function $C_p(\lambda, \beta)$ attains its maximum C_p^* at optimal values of λ and β, denoted as λ^* and β^*. While the blade pitch angle β can be maintained at the optimal β^*, the tip speed ratio λ is not, because λ depends on both the rotor angular velocity ω_r and the incoming wind speed V_w, which typically changes much faster than ω_r. The tip-speed-ratio control algorithms attempt to maintain the optimal tip speed ratio λ^* by regulating the rotor angular velocity ω_r (e.g., [11]). These algorithms usually require knowledge of λ^* and the measurements of both ω_r and V_w. Hence, there are two drawbacks of implementing them. First, due to the spatial and temporal variability of wind and the large swept area of a modern wind turbine [12], an accurate wind speed measurement may be difficult to obtain. Second, the optimal tip speed ratio may be different from one turbine to another and may change significantly over time due to icing, aging, and blade erosion.

(b) *Optimal Torque Control.* The optimal torque control algorithms attempt to drive the generator torque to its optimal value, which is proportional to the square of the turbine rotor angular velocity. References [4,13] propose an adaptive torque controller, which adaptively determines the optimal gain without *a prior* knowledge of C_p^* and λ^*; [14] presents a robust control algorithm that simultaneously seeks the optimal blade pitch angle and generator torque; [15] proposes an adaptive fuzzy controller that estimates the maximum power output from the measurements of the rotor angular velocity and the output power.

(c) *Hill Climb Searching Control.* The hill climb searching control algorithms attempt to "climb" the output power-rotor angular velocity curve by perturbing the rotor angular velocity in small steps and using feedback on the output power to adjust subsequent perturbations. Hence, Hill Climb Searching Control is also referred to as Perturb and Observe Control. The advantage of Hill Climb Searching Control is that it requires neither the measurement of wind speed nor any prior knowledge of the wind turbine characteristics. The disadvantage, however, is that it is only suitable for wind turbines with small inertia. Several applications of this control technology to achieve MPT have been reported in [16–19]. In addition, Extremum Seeking Control, which is closely related to Hill Climb Searching Control and is considered a dynamic realization of the gradient search, has been implemented in [20,21] to maximize wind energy capture by searching for both the optimal blade pitch angle and the optimal rotor angular velocity.

For operation in Region 3, the turbine power output is typically maintained at the rated power, which is often achieved by applying a constant generator torque and maintaining the turbine rotor angular velocity at the desired value, the latter being accomplished by collectively or separately pitching the turbine blades [22], suggesting the following classification:

(a) *Collective Blade Pitch Control.* Classical Proportional-Integral-Derivative (PID) control algorithms are often used to design the collective blade pitch controller to regulate the turbine speed in Region 3 [23]. Systematic methods for selecting the PID controller gains have been presented in [24, 25]. Moreover, disturbance accommodating control [26, 27], adaptive control [28–30], robust control [31], and model predictive control [32] have also been investigated. Such collective blade pitch control is a widely accepted approach to regulating rotor angular velocity and responding to fast wind speed changes. However, it cannot compensate for the asymmetric loads caused by a nonuniform wind speed field, given the large rotor swept area.

(b) *Individual Blade Pitch Control.* Since many modern utility-scale wind turbines allow the blades to be pitched independently to reduce mechanical loads, individual blade pitch control has also been reported recently in [33–38]. Specifically, classical PID control has been studied in [33–35], while multi-variable control theory has been applied in [36–38].

Recently, the use of DFIGs with two back-to-back PWM converters in the rotor circuit is becoming more and more popular in wind energy generation systems. Reasons for the popularity of DFIGs stem from advantages over other types of generators [39–42], including lower converter cost, higher system efficiency, and nearly-decoupled control of active and reactive power of the generator. Today, several power control algorithms for DFIGs have been proposed in the literature:

(a) *Vector Control*. Vector control, also called field orientation control, is a relatively mature, standard AC motor control method. Based on a synchronously rotating dq frame, the vector control algorithms achieve decoupled control of the stator-side active and reactive power. There are two field orientation schemes for DFIG power control, stator-flux-orientation and stator-voltage-orientation. The former aligns the d-axis with the stator flux vector. Neglecting the stator resistance, this scheme enables the electromagnetic torque and stator active power, and stator reactive power to be controlled by the q-component and d-component of the rotor current vector, respectively [39,43]. Several different approaches for the implementation of the stator-flux-orientation scheme have been discussed in [43]. The latter, the stator-voltage-orientation scheme, aligns the d-axis with the stator voltage vector [40, 44]. Since the stator voltage can easily be measured accurately, this scheme is independent of the DFIG parameters. Note that if the stator resistance is negligible compared to the stator reactance as in the case of high-power DFIGs, the stator voltage vector is $\pi/2$ in advance of the stator flux vector. No matter which field orientation scheme is used, the resulting control strategy is usually realized in a cascaded manner: the outer loop implements the power control, while the inner one carries out the current control, which receives the desired current commands from the outer loop. Moreover, classical PID controllers are often adopted here.

(b) *Direct Power Control.* In direct power control, converter switching states are selected from an optimal switching table based on instantaneous errors of active and reactive powers and the position of the converter terminal voltage vector or virtual flux (the flux is the integration of the converter output voltage). More recently, the direct power control algorithms of DFIG-based wind turbine systems have been proposed in [45, 46].

(c) *Passivity-Based Control.* Passivity-based control algorithms attempt to achieve stabilization of currents and rotor angular velocity via energy-balancing, regulating the power in a system automatically. In [47], such a controller is designed to achieve unity power factor at the stator of the DFIG and to track the optimal rotor angular velocity by regulating the generator torque.

In comparison with research on control of single wind turbines, relatively less work has been done on wind farm power control. Reference [48] describes a hierarchical wind farm control architecture consisting of a supervisory centralized wind farm controller and a set of turbine-level controllers, which is arguably the first of its kind. This architecture has been tested on the Horns Rev wind farm in Denmark. In [5,49], a centralized wind farm controller is introduced, which simply distributes the desired wind farm power demand to each wind turbine, in a way that is proportional to the amount of active and reactive power each turbine can produce. In [50], a wind farm-level optimization strategy for wind turbine commitment and for active and reactive power control is described. To realize the wind farm power control, the turbine-level controllers need to closely track the power reference commands provided by the centralized wind farm controller. Finally, [2] provides a performance comparison of three turbine-level control strategies for regulation of active and reactive power. More detailed descriptions of these three controllers can be found in [1, 51, 52].

More recently, researchers are considering using large wind farms with variable-speed wind turbines to achieve other goals. One such goal is to provide short-term frequency support through inertia response. To achieve this goal, research in a number of directions has been carried out, including the following: [53,54] show that variable-speed wind turbines operating in the MPT mode exhibit a negligible inertia response, since the electromagnetic torque is considered to be decoupled from the power system frequency. In contrast, [55] finds that the inertia response of variable-speed wind turbines with doubly fed induction generators (DFIGs) is strongly influenced by the rotor current controller bandwidth. In [53, 54], the inertia response is introduced by adding a supplementary control loop to the electromagnetic torque controller. Reference [56] examines the impact of increasing wind power penetration on frequency control through a comparison of the inertia responses of wind turbines with synchronous generators, with squirrel-cage induction generators, and with DFIGs containing the supplementary control loops. In [57], a control strategy is investigated, which manipulates the angle of the DFIG rotor flux vector in order to change its electromagnetic torque and release its kinetic energy. Two different control schemes for determining the additional electromagnetic torque are described and compared in [58], where the torque is proportional either to the derivative of the system frequency, or to the deviation of the system frequency from its nominal value. Reference [59] quantifies the capability of variable-speed wind turbines in providing short-term excess active power support and shows that, in a hydro dominated power system, the support can reduce the initial frequency drop due to a sudden power imbalance. Reference [60] investigates dynamic contributions of DFIGs to power system frequency responses through simulation and discusses the impact of different parameters on the inertia response of wind turbines with DFIGs. Finally, [61] conducts some static analysis to estimate how much kinetic energy can be made available for inertia response from a turbine over a year and how much energy capture must be sacrificed to do so. In addition, the trade-off of wholesale energy revenue for potential kinetic energy revenue is also explored.

1.3 Dissertation Outline and Original Contributions

This dissertation is devoted to the design and analysis of a novel collection of controllers for variable-speed wind turbines and large-scale wind farms, which significantly advance the state of the art. An outline of the dissertation, along with its original contributions, is provided below.

In Chapter 2, we design a *feedback/feedforward nonlinear controller* for variable-speed wind turbines with DFIGs. By appropriately adjusting the rotor voltages and the blade pitch angle, the controller simultaneously enables: (a) control of the active power in both the MPT and PR modes, (b) seamless switching between the two modes, and (c) control of the reactive power so that a desirable power factor is maintained. Unlike many existing designs, the controller is developed based on original, nonlinear, electromechanically-coupled models of wind turbines, without attempting approximate linearization. Its development consists of three steps: (i) employ feedback linearization to exactly cancel some of the nonlinearities and perform arbitrary pole placement, (ii) design a speed controller that makes the rotor angular velocity track a desired reference whenever possible, and (iii) introduce a Lyapunov-like function and present a gradient-based approach for minimizing this function. The effectiveness of the controller is demonstrated through simulation of a wind turbine operating under several scenarios.

In Chapter 3, we address the same problem as in Chapter 2, but allow most of the aerodynamic and mechanical parameters to be uncertain or unknown—a relaxation that has not been considered in the literature. Using a blend of linear and nonlinear control strategies (including feedback linearization, pole placement, uncertainty estimation, and gradient-based potential function minimization) as well as time-scale separation in the dynamics, we design and analyze a new controller that may be viewed as an extension of the one in Chapter 2. We show that this controller is capable of maximizing the active power in the MPT mode, regulating the active power in the PR mode, seamlessly switching between the two modes, and simultaneously adjusting the reactive power to achieve a desired power factor in the presence of uncertainties and unknowns. More specifically, the controller consists of four cascaded components, uses realistic feedback signals, and operates without knowledge of the C_p-surface, air density, friction coefficient, and wind speed. Finally, the effectiveness of the controller is shown via simulation with realistic wind profiles.

In Chapter 4, using system identification approaches, we develop a simple *approximate model* that attempts to mimic the active and reactive power dynamics of two generic WTCS models: an analytical model described by nonlinear differential equations, and an empirical one by input-output measurement data. The approximate model contains two parts—one for active power and one for reactive—each of which is a third-order system that would have been linear if not for a static nonlinearity. For each generic model, we also provide an identification scheme that sequentially determines the approximate model parameters. Finally, we show via simulation that, despite its structural simplicity, the approximate model is accurate and versatile, capable of closely imitating several different analytical and empirical WTCS models from the literature and from real data. The results suggest that the approximate model may be used to facilitate research on wind farm power control.

In Chapter 5, using advanced control techniques and different timescales in the dynamics of a wind farm control system (WFCS), we develop a *novel wind farm controller* that enables the wind farm power output to accurately and smoothly track a desired reference from the grid operator. This controller consists of two control loops: the outer loop contains a *model predictive* or *receding horizon controller*, which uses forecast of the wind speeds from crude measurements, forecast of the power demand from the grid operator, and feedback of the powers generated by the wind turbines to iteratively determine the desired power trajectories for the WTCSs. The inner loop contains an *adaptive controller* of *self-tuning regulator*-type, which uses estimated wind speed characteristics from measurements to adaptively tune the gains of a fully decentralized bank of proportional controllers. The proposed wind farm controller cooperatively optimizes the deterministic, tracking performance of the wind farm power output on a longer timescale, as well as jointly optimizes the stochastic, steady-state smoothness of the wind farm power output on a shorter timescale. We also carry out a series of simulations, which illustrate the salient features of the proposed controller.

In Chapter 6, we study from a control perspective the behavior of a standard MPT controller augmented with a proportional inertia response controller. We first show that, when there is a bias in the power system frequency, the resulting nonlinear wind turbine control system may have no equilibrium point, causing the turbine to stop rotating, or multiple equilibrium points, causing it to operate in unintended regimes. We then show that the transfer function of the linearized system has a zero at the origin, which may undesirably amplify noise, and yield pole-zero cancellation if a proportional-integral (PI) strategy is used instead. Lastly, we present a preliminary stability analysis on the linearized system, showing that it is guaranteed to be stable when reheat steam turbines are the only type of conventional generation in the power system.

Finally, in Chapter 7, we conclude the dissertation with several remarks and provide a number of possible future research directions.

Chapter 2 Nonlinear Dual-Mode Control of Variable-Speed Wind Turbines with Doubly Fed Induction Generators

2.1 Introduction

As was mentioned in Chapter 1, to enable large-scale wind farms to operate satisfactorily in both the MPT and PR modes and switch seamlessly between them, numerous challenges must be overcome. This chapter is devoted to addressing a subset of these challenges, by presenting an integrated framework for controlling the rotor voltages and the blade pitch angle of variable-speed wind turbines with doubly fed induction generators (DFIGs). The chapter presents a feedback/feedforward nonlinear controller developed based on original, nonlinear, and electromechanically-coupled models of wind turbines, without attempting approximate linearization. The controller simultaneously enables: (a) control of the active power in both the MPT and PR modes, (b) seamless switching between the two modes, and (c) control of the reactive power so that a desirable power factor is ensured. Its development consists of three steps. First, we show that, although dynamics of a wind turbine are highly nonlinear and electromechanically coupled, they offer a structure, which makes the electrical part feedback linearizable, so that arbitrary pole placement can be carried out. Second, we show that because the electrical dynamics can be made very fast, it is possible to perform model order reduction, so that only the first-order mechanical dynamics remain to be considered. For this reduced first-order model, a speed controller is designed, which enables the rotor angular velocity to track a desired reference whenever possible. Finally, we introduce a Lyapunov-like function that measures the difference between the actual and desired powers and present a gradient-based approach for minimizing this function. The effectiveness of the controller is demonstrated through simulation of a wind turbine operating under a changing wind speed, changing desired power outputs, modeling errors, and noisy measurements.

The outline of the chapter is as follows: Section 2.2 describes a model of variable-speed wind turbines with DFIGs. Section 2.3 introduces the proposed feedback/feedforward nonlinear controller. Simulation results are shown in Section 2.4. Finally, Section 2.5 concludes the chapter.

2.2 Problem Formulation

Consider a variable-speed wind turbine consisting of a doubly fed induction generator (DFIG) and a power electronics converter, as shown in Figure 2.1. The DFIG may be regarded as a slip-ring induction machine, whose stator winding is directly connected to the grid, and whose rotor winding is connected to the grid through a bidirectional frequency converter using back-to-back PWM voltage-source converters.

The dynamics of the electrical part of the wind turbine are represented by a fourth-order state space model, constructed using the synchronously rotating reference frame (*dq*-frame), where the relation between the three phase quantities and the *dq* components is defined by Park's transformation [62]. The

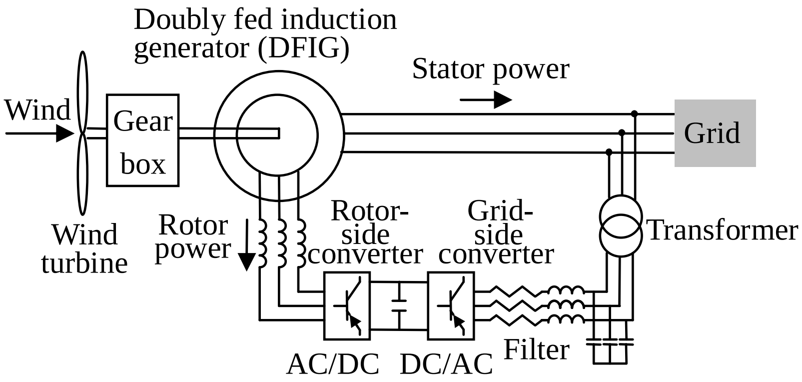

Figure 2.1: Schematic of a typical variable-speed wind turbine with a DFIG.

voltage equations are [63]

$$v_{ds} = R_s i_{ds} - \omega_s \varphi_{qs} + \frac{d}{dt}\varphi_{ds}, \tag{2.1}$$

$$v_{qs} = R_s i_{qs} + \omega_s \varphi_{ds} + \frac{d}{dt}\varphi_{qs}, \tag{2.2}$$

$$v_{dr} = R_r i_{dr} - (\omega_s - \omega_r)\varphi_{qr} + \frac{d}{dt}\varphi_{dr}, \tag{2.3}$$

$$v_{qr} = R_r i_{qr} + (\omega_s - \omega_r)\varphi_{dr} + \frac{d}{dt}\varphi_{qr}, \tag{2.4}$$

where v_{ds}, v_{qs}, v_{dr}, $v_{qr} \in \mathbb{R}$ are the d- and q-axis of the stator and rotor voltages; i_{ds}, i_{qs}, i_{dr}, $i_{qr} \in \mathbb{R}$ are the d- and q-axis of the stator and rotor currents; φ_{ds}, φ_{qs}, φ_{dr}, $\varphi_{qr} \in \mathbb{R}$ are the d- and q-axis of the stator and rotor fluxes; $\omega_s > 0$ is the constant angular velocity of the synchronously rotating reference frame; $\omega_r > 0$ is the rotor angular velocity; and R_s, R_r are the stator and rotor resistances. The flux equations are [63]

$$\varphi_{ds} = L_s i_{ds} + L_m i_{dr}, \tag{2.5}$$

$$\varphi_{qs} = L_s i_{qs} + L_m i_{qr}, \tag{2.6}$$

$$\varphi_{dr} = L_m i_{ds} + L_r i_{dr}, \tag{2.7}$$

$$\varphi_{qr} = L_m i_{qs} + L_r i_{qr}, \tag{2.8}$$

where L_s, L_r, and L_m are the stator, rotor, and mutual inductances, respectively, satisfying $L_s > L_m$ and $L_r > L_m$. From (2.5)–(2.8), the current equations can be written as

$$i_{ds} = \frac{1}{\sigma L_s}\varphi_{ds} - \frac{L_m}{\sigma L_s L_r}\varphi_{dr}, \tag{2.9}$$

$$i_{qs} = \frac{1}{\sigma L_s}\varphi_{qs} - \frac{L_m}{\sigma L_s L_r}\varphi_{qr}, \tag{2.10}$$

$$i_{dr} = -\frac{L_m}{\sigma L_s L_r}\varphi_{ds} + \frac{1}{\sigma L_r}\varphi_{dr}, \tag{2.11}$$

$$i_{qr} = -\frac{L_m}{\sigma L_s L_r}\varphi_{qs} + \frac{1}{\sigma L_r}\varphi_{qr}, \tag{2.12}$$

where $\sigma = (1 - \frac{L_m^2}{L_s L_r})$ is the leak coefficient. Selecting the fluxes as state variables and substituting (2.9)–(2.12) into (2.1)–(2.4), the electrical dynamics in state space form can be written as

$$\frac{d}{dt}\varphi_{ds} = -\frac{R_s}{\sigma L_s}\varphi_{ds} + \omega_s\varphi_{qs} + \frac{R_s L_m}{\sigma L_s L_r}\varphi_{dr} + v_{ds}, \tag{2.13}$$

$$\frac{d}{dt}\varphi_{qs} = -\omega_s\varphi_{ds} - \frac{R_s}{\sigma L_s}\varphi_{qs} + \frac{R_s L_m}{\sigma L_s L_r}\varphi_{qr} + v_{qs}, \tag{2.14}$$

$$\frac{d}{dt}\varphi_{dr} = \frac{R_r L_m}{\sigma L_s L_r}\varphi_{ds} - \frac{R_r}{\sigma L_r}\varphi_{dr} + (\omega_s - \omega_r)\varphi_{qr} + v_{dr}, \tag{2.15}$$

$$\frac{d}{dt}\varphi_{qr} = \frac{R_r L_m}{\sigma L_s L_r}\varphi_{qs} - (\omega_s - \omega_r)\varphi_{dr} - \frac{R_r}{\sigma L_r}\varphi_{qr} + v_{qr}. \tag{2.16}$$

Neglecting power losses associated with the stator and rotor resistances, the active and reactive stator and rotor powers are given by [64]

$$P_s = -v_{ds}i_{ds} - v_{qs}i_{qs}, \tag{2.17}$$

$$Q_s = -v_{qs}i_{ds} + v_{ds}i_{qs}, \tag{2.18}$$

$$P_r = -v_{dr}i_{dr} - v_{qr}i_{qr}, \tag{2.19}$$

$$Q_r = -v_{qr}i_{dr} + v_{dr}i_{qr}, \tag{2.20}$$

and the total active and reactive powers of the turbine are

$$P = P_s + P_r, \tag{2.21}$$

$$Q = Q_s + Q_r, \tag{2.22}$$

where positive (negative) values of P and Q mean that the turbine injects power into (draws power from) the grid.

The dynamics of the mechanical part of the wind turbine are represented by a first-order model

$$J \frac{d}{dt} \omega_r = T_m - T_e - C_f \omega_r, \tag{2.23}$$

where the rotor angular velocity ω_r is another state variable, J is the moment of inertia, C_f is the friction coefficient, T_m is the mechanical torque generated, and T_e is the electromagnetic torque given by [64]

$$T_e = \varphi_{qs} i_{ds} - \varphi_{ds} i_{qs}, \tag{2.24}$$

where positive (negative) values mean the turbine acts as a generator (motor). The mechanical power captured by the wind turbine is given by [65]

$$P_m = T_m \omega_r = \frac{1}{2} \rho A C_p(\lambda, \beta) V_w^3, \tag{2.25}$$

where ρ is the air density; $A = \pi R^2$ is the area swept by the rotor blades of radius R; V_w is the wind speed; and $C_p(\lambda, \beta)$, commonly referred to as the C_p-surface is the performance coefficient of the wind turbine, whose value is a function [65] of the tip speed ratio $\lambda \in (0, \infty)$, defined as

$$\lambda = \frac{\omega_r R}{V_w}, \tag{2.26}$$

as well as the blade pitch angle β, assumed to lie within some mechanical limits $\beta_{\min}$ and $\beta_{\max}$. This function is typically provided by turbine manufacturers and may vary greatly from one turbine to another [65]. Therefore, to make the results of this chapter broadly applicable to a wide variety of turbines, no specific expression of $C_p(\lambda, \beta)$ will be assumed, until it is absolutely necessary in Section 2.4, to carry out simulations. Instead, $C_p(\lambda, \beta)$ will only be assumed to satisfy the following mild conditions for the purpose of analysis:

(A1) Function $C_p(\lambda, \beta)$ is continuously differentiable in both λ and β over $\lambda \in (0, \infty)$ and $\beta \in [\beta_{\min}, \beta_{\max}]$.

(A2) There exists $c \in (0, \infty)$ such that for all $\lambda \in (0, \infty)$ and $\beta \in [\beta_{\min}, \beta_{\max}]$, we have $C_p(\lambda, \beta) \leq c\lambda$. This condition is mild because it is equivalent to saying that the mechanical torque T_m is bounded from above, since $T_m \propto \frac{C_p(\lambda,\beta)}{\lambda}$ according to (2.25) and (2.26).

(A3) For each fixed $\beta \in [\beta_{\min}, \beta_{\max}]$, there exists $\lambda_1 \in (0, \infty)$ such that for all $\lambda \in (0, \lambda_1)$, we have $C_p(\lambda, \beta) > 0$. This condition is also mild because turbines are designed to capture wind power over a wide range of λ, including times when λ is small.

(A4) There exist $\underline{c} \in (-\infty, 0)$ and $\overline{c} \in (0, \infty)$ such that for all $\lambda \in (0, \infty)$ and $\beta \in [\beta_{\min}, \beta_{\max}]$, we have $\underline{c} \leq \frac{\partial}{\partial\lambda}(\frac{C_p(\lambda,\beta)}{\lambda}) \leq \overline{c}$.

As it follows from the above, the wind turbine studied here is modeled as a fifth-order, electromechanically-coupled, nonlinear dynamical system with states $[\varphi_{ds}\ \varphi_{qs}\ \varphi_{dr}\ \varphi_{qr}\ \omega_r]^T$, controls $[v_{dr}\ v_{qr}\ \beta]^T$, outputs $[P\ Q]^T$, exogenous “disturbance” V_w, nonlinear state equations (2.13)–(2.16) and (2.23), and nonlinear output equations (2.17)–(2.22). Notice that the system dynamics are strongly coupled: the “mechanical” state variable ω_r affects the electrical dynamics bilinearly via (2.15) and (2.16), while the “electrical” state variables $[\varphi_{ds}\ \varphi_{qs}\ \varphi_{dr}\ \varphi_{qr}]^T$ affect the mechanical dynamics quadratically via (2.9)–

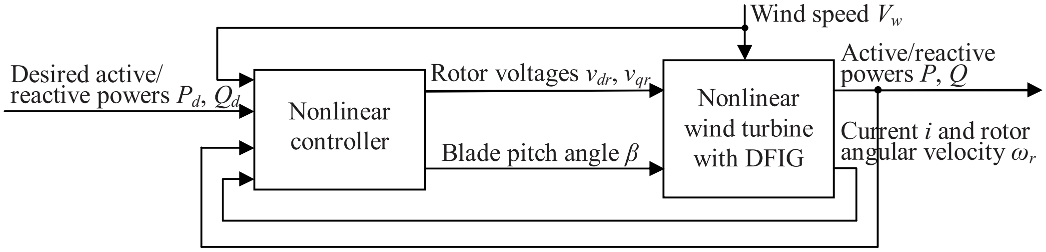

Figure 2.2: Structure of the multivariable, feedback/feedforward nonlinear controller, developed based on original, nonlinear dynamics of the wind turbine.

(2.12), (2.24) and (2.23). Since the stator winding of the DFIG is directly connected to the grid, for reliability reasons $[v_{ds}\ v_{qs}]^T$ are assumed to be fixed, i.e., not to be controlled, in the rest of this chapter. Moreover, since (2.9)–(2.12) represent a bijective mapping between $[\varphi_{ds}\ \varphi_{qs}\ \varphi_{dr}\ \varphi_{qr}]^T$ and $[i_{ds}\ i_{qs}\ i_{dr}\ i_{qr}]^T$ and since the currents $[i_{ds}\ i_{qs}\ i_{dr}\ i_{qr}]^T$, the rotor angular velocity ω_r, and the wind speed V_w can all be measured, a controller for this system has access to its entire states (i.e., full state feedback is available) and its disturbance (i.e., the wind speed V_w). A block diagram of this system is shown on the right-hand side of Figure 2.2.

2.3 Controller Design

In this section, a feedback/feedforward nonlinear controller of the form depicted on the left-hand side of Figure 2.2 is presented. By adjusting the rotor voltages v_{dr} and v_{qr} and the blade pitch angle β, the controller attempts to make the active and reactive powers P and Q track, as closely as possible—limited only by wind strength—some desired, time-varying references P_d and Q_d, presumably provided by a wind farm operator. When P_d is set to sufficiently large, i.e., larger than what the turbine can possibly convert from wind, it means the operator wants the turbine to operate in the MPT mode; otherwise, the PR mode is sought. The value of Q_d, along with that of P_d, reflects a desired power factor $\mathrm{PF}_d = \frac{P_d}{\sqrt{P_d^2+Q_d^2}}$ the operator wants the turbine to also maintain.

The controller development consists of three steps, which are described in Sections 2.3.1–2.3.3, respectively.

2.3.1 Feedback Linearization and Pole Placement

For convenience, let us introduce the variables $\varphi = [\varphi_{ds}\ \varphi_{qs}\ \varphi_{dr}\ \varphi_{qr}]^T$ and $i = [i_{ds}\ i_{qs}\ i_{dr}\ i_{qr}]^T$, and rewrite (2.9)–(2.12) and (2.13)–(2.16) in matrix forms as follows:

$$\dot{\varphi} = \underbrace{\begin{bmatrix} -\frac{R_s}{\sigma L_s} & \omega_s & \frac{R_s L_m}{\sigma L_s L_r} & 0 \\ -\omega_s & -\frac{R_s}{\sigma L_s} & 0 & \frac{R_s L_m}{\sigma L_s L_r} \\ \frac{R_r L_m}{\sigma L_s L_r} & 0 & -\frac{R_r}{\sigma L_r} & \omega_s \\ 0 & \frac{R_r L_m}{\sigma L_s L_r} & -\omega_s & -\frac{R_r}{\sigma L_r} \end{bmatrix}}_{A} \varphi + \underbrace{\begin{bmatrix} 0 & 0 \\ 0 & 0 \\ 1 & 0 \\ 0 & 1 \end{bmatrix}}_{B} \begin{bmatrix} v_{dr} \\ v_{qr} \end{bmatrix} + \begin{bmatrix} v_{ds} \\ v_{qs} \\ -\omega_r \varphi_{qr} \\ \omega_r \varphi_{dr} \end{bmatrix}, \quad (2.27)$$

$$i = \begin{bmatrix} \frac{1}{\sigma L_s} & 0 & -\frac{L_m}{\sigma L_s L_r} & 0 \\ 0 & \frac{1}{\sigma L_s} & 0 & -\frac{L_m}{\sigma L_s L_r} \\ -\frac{L_m}{\sigma L_s L_r} & 0 & \frac{1}{\sigma L_r} & 0 \\ 0 & -\frac{L_m}{\sigma L_s L_r} & 0 & \frac{1}{\sigma L_r} \end{bmatrix} \varphi, \quad (2.28)$$

where A and B are constant matrices and, as was pointed out at the end of Section 2.2, both v_{ds} and v_{qs} are constants not to be controlled. Note that the only nonlinearities in (2.27) are the two products of the state variables, i.e., $-\omega_r\varphi_{qr}$ and $\omega_r\varphi_{dr}$. Also note that these nonlinearities appear on the same rows as the control variables v_{dr} and v_{qr}. Thus, *feedback linearization* [66] may be used to cancel them and subsequently perform arbitrary *pole placement* [67], i.e., let

$$v_{dr} = \omega_r \varphi_{qr} - K_1^T \varphi + u_1, \tag{2.29}$$

$$v_{qr} = -\omega_r \varphi_{dr} - K_2^T \varphi + u_2, \tag{2.30}$$

where $K_1, K_2 \in \mathbb{R}^4$, the first terms on the right-hand side of (2.29) and (2.30) are intended to cancel the nonlinearities, the second terms are for pole placement, and the third are new control variables u_1 and u_2, to be designed later.

To implement (2.29) and (2.30), full state feedback on the fluxes φ and the rotor angular velocity ω_r are needed. While the latter is relatively easy to measure, the former is not. Fortunately, this difficulty can be circumvented by first measuring the currents—which is feasible—and then calculating the fluxes from (2.5)–(2.8). This explains the fourth input of the *nonlinear controller* block in Figure 2.2.

Substituting (2.29) and (2.30) into (2.27) yields

$$\dot{\varphi} = (A - BK)\varphi + \left[v_{ds}\; v_{qs}\; u_1\; u_2\right]^T, \tag{2.31}$$

where $K = [K_1 \quad K_2]^T$ is the state feedback gain matrix. Since the electrical elements in the DFIG are physically allowed to have much faster responses than their mechanical counterparts, K in (2.31) may be chosen so that $A - BK$ is asymptotically stable with very fast eigenvalues. With this choice of K and with relatively slow-varying u_1 and u_2 (recall that v_{ds} and v_{qs} are constants), the fourth-order linear differential equation (2.31) may be approximated by the following static, linear equation:

$$\varphi = -(A - BK)^{-1} \left[v_{ds}\; v_{qs}\; u_1\; u_2\right]^T. \tag{2.32}$$

As a result, the fifth-order model described in (2.13)–(2.16) and (2.23) may be approximated by the first-order model described in (2.23) along with algebraic relationships (2.29), (2.30), and (2.32). As will be shown next, this approximation greatly simplifies the design of u_1 and u_2. Therefore, we will assume, in the sequel, that K is chosen so that the electrical dynamics (2.31) are asymptotically stable and so fast that they may be approximated by (2.32).

2.3.2 Tracking of Desired Angular Velocity

The second step of the controller development involves constructing a speed controller that ensures the angular velocity of the rotor, ω_r, tracks a desired, time-varying reference, ω_{rd}, whenever possible. The construction may be divided into four substeps as described below.

Substep 1. First, we show that the electromagnetic torque T_e defined in (2.24) may be expressed as a *quadratic function* of the new control variables u_1 and u_2. From (2.24) and (2.28),

$$\begin{aligned} T_e &= \varphi_{qs} i_{ds} - \varphi_{ds} i_{qs} = \begin{bmatrix} \varphi_{qs} & -\varphi_{ds} \end{bmatrix} \begin{bmatrix} i_{ds} \\ i_{qs} \end{bmatrix} \\ &= \varphi^T \begin{bmatrix} 0 & -\frac{1}{\sigma L_s} & 0 & \frac{L_m}{\sigma L_s L_r} \\ \frac{1}{\sigma L_s} & 0 & -\frac{L_m}{\sigma L_s L_r} & 0 \\ 0 & 0 & 0 & 0 \\ 0 & 0 & 0 & 0 \end{bmatrix} \varphi. \end{aligned} \tag{2.33}$$

Equation (2.33) suggests that T_e is a quadratic function of φ, while (2.32) suggests that φ, in turn, is an affine function of u_1 and u_2, since v_{ds} and v_{qs} in (2.32) are assumed to be constants. Hence, T_e must be a quadratic function of u_1 and u_2. Indeed, an explicit expression can be obtained as follows: since

$A-BK$ is asymptotically stable and thus nonsingular, it may be written as

$$(A-BK)^{-1} = \begin{bmatrix} d_{11} & d_{12} & d_{13} & d_{14} \\ d_{21} & d_{22} & d_{23} & d_{24} \\ d_{31} & d_{32} & d_{33} & d_{34} \\ d_{41} & d_{42} & d_{43} & d_{44} \end{bmatrix}, \tag{2.34}$$

where each d_{ij} depends on A, B, and K. From (2.32)–(2.34),

$$\begin{aligned} T_e = {} & \frac{L_m}{\sigma L_s L_r}[(d_{11}v_{ds} + d_{12}v_{qs} + d_{13}u_1 + d_{14}u_2)(d_{41}v_{ds} + d_{42}v_{qs} + d_{43}u_1 + d_{44}u_2) \\ & - (d_{21}v_{ds} + d_{22}v_{qs} + d_{23}u_1 + d_{24}u_2)(d_{31}v_{ds} + d_{32}v_{qs} + d_{33}u_1 + d_{34}u_2)] \\ = {} & \begin{bmatrix} u_1 & u_2 \end{bmatrix} \begin{bmatrix} q_1 & q_2 \\ q_2 & q_3 \end{bmatrix} \begin{bmatrix} u_1 \\ u_2 \end{bmatrix} + \begin{bmatrix} b_1 & b_2 \end{bmatrix} \begin{bmatrix} u_1 \\ u_2 \end{bmatrix} + a, \end{aligned} \tag{2.35}$$

where q_1, q_2, q_3, b_1, b_2, and a are constants defined as

$$q_1 = \frac{L_m}{\sigma L_s L_r}(d_{13}d_{43} - d_{23}d_{33}), \tag{2.36}$$

$$q_2 = \frac{1}{2}\frac{L_m}{\sigma L_s L_r}(d_{13}d_{44} + d_{14}d_{43} - d_{23}d_{34} - d_{24}d_{33}), \tag{2.37}$$

$$q_3 = \frac{L_m}{\sigma L_s L_r}(d_{14}d_{44} - d_{24}d_{34}), \tag{2.38}$$

$$\begin{aligned} b_1 = {} & \frac{L_m}{\sigma L_s L_r}\big((d_{11}v_{ds} + d_{12}v_{qs})d_{43} + d_{13}(d_{41}v_{ds} + d_{42}v_{qs}) \\ & - (d_{21}v_{ds} + d_{22}v_{qs})d_{33} - d_{23}(d_{31}v_{ds} + d_{32}v_{qs})\big), \end{aligned} \tag{2.39}$$

$$\begin{aligned} b_2 = {} & \frac{L_m}{\sigma L_s L_r}\big((d_{11}v_{ds} + d_{12}v_{qs})d_{44} + d_{14}(d_{41}v_{ds} + d_{42}v_{qs}) \\ & - (d_{21}v_{ds} + d_{22}v_{qs})d_{34} - d_{24}(d_{31}v_{ds} + d_{32}v_{qs})\big), \end{aligned} \tag{2.40}$$

$$\begin{aligned} a = {} & \frac{L_m}{\sigma L_s L_r}\big((d_{11}v_{ds} + d_{12}v_{qs})(d_{41}v_{ds} + d_{42}v_{qs}) \\ & - (d_{21}v_{ds} + d_{22}v_{qs})(d_{31}v_{ds} + d_{32}v_{qs})\big). \end{aligned} \tag{2.41}$$

Substep 2. Next, we show that the quadratic function (2.35) relating u_1 and u_2 to T_e has a desirable feature: its associated Hessian matrix $\left[\begin{smallmatrix} q_1 & q_2 \\ q_2 & q_3 \end{smallmatrix}\right]$ is always *positive definite*, regardless of the parameters of the electrical part of the DFIG, as well as the choice of the state feedback gain matrix K. The following lemma formally states and proves this assertion:

Lemma 2.1. *The Hessian matrix* $\left[\begin{smallmatrix} q_1 & q_2 \\ q_2 & q_3 \end{smallmatrix}\right]$ *in* (2.35) *is positive definite.*

Proof. From (2.27), (2.31), (2.34), and (2.36)–(2.38), the determinant of $A - BK$ and the leading principal minors q_1 and $q_1 q_3 - q_2^2$ of $\left[\begin{smallmatrix} q_1 & q_2 \\ q_2 & q_3 \end{smallmatrix}\right]$ can be written as

$$|A - BK| = \frac{\Delta}{(L_s L_r - L_m^2)^2}, \tag{2.42}$$

$$q_1 = \frac{R_s L_m^2 (\Delta_1^2 + \Delta_2^2)}{\Delta^2}, \tag{2.43}$$

$$q_1 q_3 - q_2^2 = \frac{R_s^2 L_m^4}{\Delta^2}, \tag{2.44}$$

where

$$\begin{aligned} \Delta = {} & \big(- R_s L_m k_{12} + (L_s L_r - L_m^2) k_{13} - R_s L_r k_{14} + R_r L_s + R_s L_r \big) \Delta_1 \\ & + \big(R_s L_m k_{11} + R_s L_r k_{13} + (L_s L_r - L_m^2) k_{14} + R_s R_r - L_s L_r + L_m^2 \big) \Delta_2, \\ \Delta_1 = {} & R_s L_m k_{21} + R_s L_r k_{23} + (L_s L_r - L_m^2) k_{24} + R_r L_s + R_s L_r, \\ \Delta_2 = {} & R_s L_m k_{22} + (-L_s L_r + L_m^2) k_{23} + R_s L_r k_{24} + R_s R_r - L_s L_r + L_m^2, \end{aligned} \tag{2.45}$$

and k_{ij} is the ij entry of K. Since $A - BK$ is nonsingular, $L_s > L_m$, and $L_r > L_m$, it follows from (2.42) that $\Delta \neq 0$. Since $\Delta \neq 0$, it follows from (2.44) that $q_1 q_3 - q_2^2 > 0$ and from (2.45) that Δ_1 and Δ_2 cannot be zero simultaneously. The latter, along with (2.43), implies that $q_1 > 0$. Since $q_1 > 0$ and $q_1 q_3 - q_2^2 > 0$, $\left[\begin{smallmatrix} q_1 & q_2 \\ q_2 & q_3 \end{smallmatrix}\right]$ in (2.35) must be positive definite. □

Substep 3. Next, we show that there is a *redundancy* in the control variables u_1 and u_2, which may be exposed via a *coordinate change*. Observe from (2.23) that the first-order dynamics of ω_r are driven by T_e. Also observe from Substeps 1 and 2 that T_e is a convex quadratic function of u_1 and u_2. Thus, we have *two* coupled control inputs (i.e., u_1 and u_2) collectively affecting *one* state variable (i.e., ω_r), implying that there is a redundancy in the control inputs, which may be exploited elsewhere (to be discussed in Section 2.3.3). To expose this redundancy, first notice that because the Hessian matrix $\left[\begin{smallmatrix} q_1 & q_2 \\ q_2 & q_3 \end{smallmatrix}\right]$ is positive definite, it can be diagonalized, i.e., there exist an orthogonal matrix M containing its eigenvectors and a diagonal matrix D containing its eigenvalues, such that

$$M^T \begin{bmatrix} q_1 & q_2 \\ q_2 & q_3 \end{bmatrix} M = D. \tag{2.46}$$

Indeed,

$$M = \begin{bmatrix} \frac{q_2}{\sqrt{q_2^2+(\lambda_1-q_1)^2}} & \frac{\lambda_2-q_3}{\sqrt{(\lambda_2-q_3)^2+q_2^2}} \\ \frac{\lambda_1-q_1}{\sqrt{q_2^2+(\lambda_1-q_1)^2}} & \frac{q_2}{\sqrt{(\lambda_2-q_3)^2+q_2^2}} \end{bmatrix}, \quad D = \begin{bmatrix} \lambda_1 & 0 \\ 0 & \lambda_2 \end{bmatrix},$$

where

$$\lambda_{1,2} = \frac{q_1 + q_3 \pm \sqrt{(q_1+q_3)^2 - 4(q_1 q_3 - q_2^2)}}{2}.$$

Next, consider the following coordinate change, which transforms $u_1 \in \mathbb{R}$ and $u_2 \in \mathbb{R}$ in a Cartesian coordinate system into $r \geq 0$ and $\theta \in [0, 2\pi)$ in a polar coordinate system:

$$r = \sqrt{z_1^2 + z_2^2}, \quad \theta = \text{atan2}(z_2, z_1), \tag{2.47}$$

where

$$\begin{bmatrix} z_1 \\ z_2 \end{bmatrix} = D^{1/2} M^T \begin{bmatrix} u_1 \\ u_2 \end{bmatrix} + \frac{1}{2} D^{-1/2} M^T \begin{bmatrix} b_1 \\ b_2 \end{bmatrix}, \tag{2.48}$$

atan2() denotes the four-quadrant arctangent function. In terms of the new coordinates r and θ, it follows from (2.35) and (2.46)–(2.48) that

$$T_e = r^2 + a', \tag{2.49}$$

where

$$a' = a - \frac{1}{4}\begin{bmatrix} b_1 & b_2 \end{bmatrix}\begin{bmatrix} q_1 & q_2 \\ q_2 & q_3 \end{bmatrix}^{-1}\begin{bmatrix} b_1 \\ b_2 \end{bmatrix}.$$

Using (2.36)–(2.41), a' may be simplified to

$$a' = -\frac{v_{ds}^2 + v_{qs}^2}{4\omega_s R_s}, \tag{2.50}$$

implying that it is always negative. Comparing (2.49) with (2.35) shows that the coordinate change (2.47) and (2.48) allows us to decouple the control variables, so that in the new coordinates, r is responsible for driving the first-order dynamics of ω_r through T_e of (2.49), while θ does not at all affect ω_r (and, hence, is redundant as far as the dynamics of ω_r are concerned). The design of r and θ will be discussed in Substep 4 and Section 2.3.3, respectively.

Substep 4. Finally, a *speed controller* is presented, which ensures that the rotor angular velocity ω_r tracks a desired time-varying reference ω_{rd}, to be determined in Section 2.3.3, provided that ω_{rd} is not exceedingly large. Combining (2.23) and (2.49) yields

$$J\dot{\omega}_r = T_m(\omega_r, \beta, V_w) - r^2 - a' - C_f\omega_r, \tag{2.51}$$

where, according to (2.25),

$$T_m(\omega_r, \beta, V_w) = \frac{\frac{1}{2}\rho A C_p(\lambda, \beta) V_w^3}{\omega_r}. \tag{2.52}$$

Here, T_m is written as $T_m(\omega_r, \beta, V_w)$ to emphasize its dependence on ω_r, β, and V_w. Observe from (2.51) that, if the control input r^2 were *real-valued* instead of being nonnegative, feedback linearization may be applied to cancel all the terms on the right-hand side of (2.51) and insert linear dynamics $\alpha(\omega_r - \omega_{rd})$, i.e., we may let

$$r^2 = T_m(\omega_r, \beta, V_w) - a' - C_f\omega_r + \alpha(\omega_r - \omega_{rd}), \tag{2.53}$$

so that

$$J\dot{\omega}_r = -\alpha(\omega_r - \omega_{rd}). \tag{2.54}$$

By letting the controller parameter α be positive, (2.54) implies that ω_r always attempts to go to ω_{rd}. Unfortunately, because r^2 cannot be negative, the speed controller (2.53)—and, hence, the linear dynamics (2.54)—cannot be realized whenever the right-hand side of (2.53) is negative. To alleviate this issue, (2.53) is slightly modified by setting r^2 to zero whenever that occurs, i.e.,

$$r^2 = \max\{T_m(\omega_r, \beta, V_w) - a' - C_f\omega_r + \alpha(\omega_r - \omega_{rd}), 0\}. \tag{2.55}$$

Notice that (2.55) contains a feedforward action involving the "disturbance", i.e., the wind speed V_w. This explains the first input of the *nonlinear controller* block in Figure 2.2.

To analyze the behavior of the speed controller (2.55), suppose ω_{rd}, β, and V_w are constants and consider the function g, defined as

$$g(\omega_r, \beta, V_w) = T_m(\omega_r, \beta, V_w) - a' - C_f\omega_r. \tag{2.56}$$

The following lemma says that $g(\omega_r, \beta, V_w)$, when viewed as a function of ω_r, has a positive root $\omega_r^{(1)}$, below which $g(\omega_r, \beta, V_w)$ is positive:

Lemma 2.2. *For each fixed* $\beta \in [\beta_{\min}, \beta_{\max}]$ *and* $V_w > 0$*, there exists* $\omega_r^{(1)} \in (0, \infty)$ *such that* $g(\omega_r^{(1)}, \beta, V_w) = 0$ *and* $g(\omega_r, \beta, V_w) > 0$ *for all* $\omega_r \in (0, \omega_r^{(1)})$.

Proof. Due to the fact that a' in (2.50) is negative, there exists $\omega_{r,1}$ such that $-a' - C_f\omega_r > 0$ for all $\omega_r \in (0, \omega_{r,1})$. Due to Assumption (A3) of Section 2.2, (2.26), and (2.52), there exists $\omega_{r,2}$ such that $T_m(\omega_r, \beta, V_w) > 0$ for all $\omega_r \in (0, \omega_{r,2})$. Hence, from (2.56), we have $g(\omega_r, \beta, V_w) > 0$ for all

$\omega_r \in (0, \min\{\omega_{r,1}, \omega_{r,2}\})$. In addition, due to Assumption (A2), (2.26), (2.52), (2.56), and $a' < 0$, there exists $\omega_{r,3}$, sufficiently large, such that $g(\omega_{r,3}, \beta, V_w) < 0$. These two properties of g, along with Assumption (A1) and the Intermediate Value Theorem, imply that there exists at least one positive root ω_r satisfying $g(\omega_r, \beta, V_w) = 0$. Letting $\omega_r^{(1)}$ be the first of such roots completes the proof. $\square$

The following theorem, derived based on Lemma 2.2, says that as long as the desired rotor angular velocity ω_{rd} is not exceedingly large, i.e., does not exceed the first root $\omega_r^{(1)}$ of $g(\omega_r, \beta, V_w)$, the closed-loop dynamics (2.51) and (2.55) have an asymptotically stable equilibrium point at ω_{rd}:

Theorem 2.1. *Consider the first-order dynamics* (2.51) *and the speed controller* (2.55)*. Suppose ω_{rd}, β, and V_w are constants, with ω_{rd} satisfying* $0 < \omega_{rd} < \omega_r^{(1)}$. *Then, for all* $\omega_r(0) > 0$, $\lim_{t\to\infty} \omega_r(t) = \omega_{rd}$.

Proof. Substituting (2.55) into (2.51) and using (2.56) yield

$$J\dot{\omega}_r = \min\{\alpha(\omega_{rd} - \omega_r), g(\omega_r, \beta, V_w)\}. \tag{2.57}$$

Suppose $0 < \omega_{rd} < \omega_r^{(1)}$. We first show that $\omega_r = \omega_{rd}$ is the unique equilibrium point of (2.57). Suppose $\omega_r = \omega_{rd}$. Then, $\alpha(\omega_{rd} - \omega_r)$ in (2.57) is zero, whereas $g(\omega_r, \beta, V_w)$ in (2.57) is positive, due to Lemma 2.2. Thus, $\dot{\omega}_r = 0$, implying that ω_{rd} is an equilibrium point. Next, suppose $0 < \omega_r < \omega_{rd}$. Then, $\alpha(\omega_{rd} - \omega_r)$ is positive, and so is $g(\omega_r, \beta, V_w)$, due again to Lemma 2.2. Hence, $\dot{\omega}_r > 0$, implying that there is no equilibrium point to the left of ω_{rd}. Finally, suppose $\omega_r > \omega_{rd}$. Then, $\alpha(\omega_{rd} - \omega_r)$ is negative. Therefore, $\dot{\omega}_r < 0$, implying that there is no equilibrium point to the right of ω_{rd}. From the above analysis, we see that $\omega_r = \omega_{rd}$ is the unique equilibrium point of (2.57). Next, we show that the equilibrium point $\omega_r = \omega_{rd}$ is asymptotically stable in that for all $\omega_r(0) > 0$, $\lim_{t\to\infty} \omega_r(t) = \omega_{rd}$. Consider a quadratic Lyapunov function candidate $V : (0, \infty) \to \mathbb{R}$, defined as

$$V(\omega_r) = \frac{1}{2}(\omega_r - \omega_{rd})^2, \tag{2.58}$$

which is positive definite with respect to the shifted origin $\omega_r = \omega_{rd}$. From (2.57) and (2.58),

$$\dot{V}(\omega_r) = \frac{1}{J}(\omega_r - \omega_{rd}) \min\{\alpha(\omega_{rd} - \omega_r), g(\omega_r, \beta, V_w)\}. \tag{2.59}$$

Note that whenever $0 < \omega_r < \omega_{rd}$, $\alpha(\omega_{rd} - \omega_r) > 0$ and $g(\omega_r, \beta, V_w) > 0$, so that $\dot{V}(\omega_r) < 0$ according to (2.59). On the other hand, whenever $\omega_r > \omega_{rd}$, $\alpha(\omega_{rd} - \omega_r) < 0$, so that $\dot{V}(\omega_r) < 0$. Finally, when $\omega_r = \omega_{rd}$, $\dot{V}(\omega_r) = 0$. Therefore, $\dot{V}(\omega_r)$ is negative definite with respect to the shifted origin $\omega_r = \omega_{rd}$. It follows from [66] that $\omega_r = \omega_{rd}$ is asymptotically stable, i.e., for all $\omega_r(0) > 0$, $\lim_{t\to\infty} \omega_r(t) = \omega_{rd}$. □

Theorem 2.1 says that the first root $\omega_r^{(1)}$ is a *critical root*, for which ω_{rd} should never exceed, if we want $\omega_r(t)$ to go to ω_{rd} regardless of $\omega_r(0)$. Figure 2.3 shows, for the MATLAB/Simulink R2007a model of $C_p(\lambda, \beta)$ given in (2.70) and (2.71), how the critical root $\omega_r^{(1)}$ depends on β and V_w. Notice from the figure that $\omega_r^{(1)}$ is insensitive to β but proportional to V_w, meaning that the larger the wind speed, the higher the "ceiling" on the desired rotor angular velocity. Also notice that $\omega_r^{(1)}$ of more than 3500 in the per-unit system is extremely large, meaning that for this particular turbine there is no need to be concerned about ω_{rd} exceeding $\omega_r^{(1)}$.

2.3.3 Lyapunov-like Function and Gradient-based Approach

The third and final step of the controller development involves introducing a Lyapunov-like function, which measures the difference between the actual

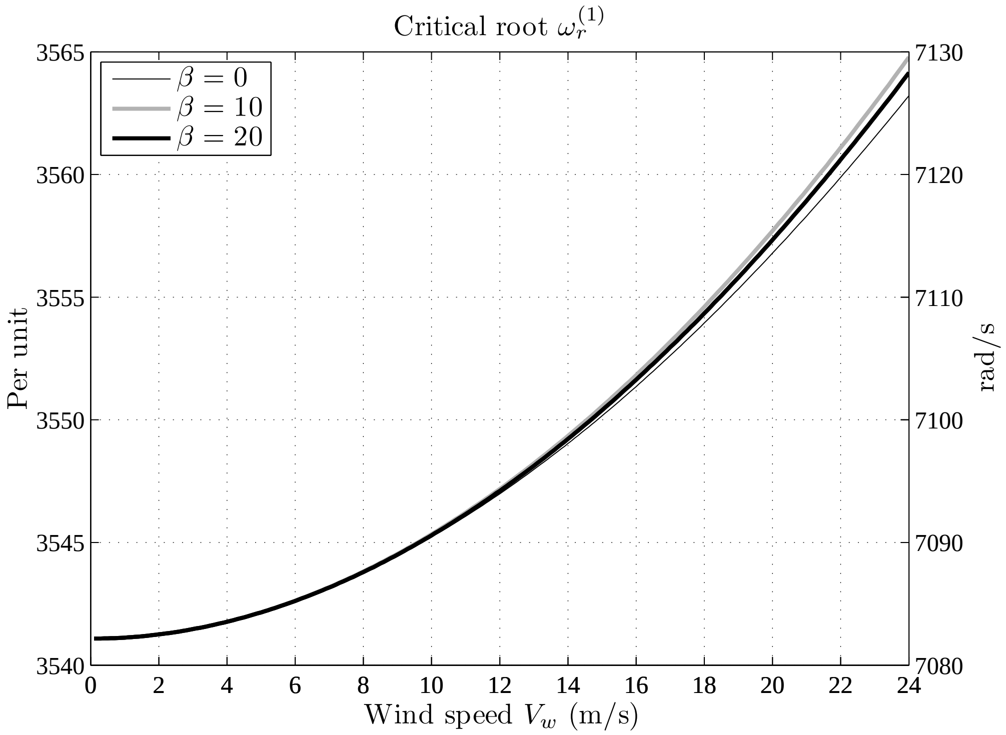

Figure 2.3: Critical root $\omega_r^{(1)}$ as a function of blade pitch angle β and wind speed V_w.

and desired powers, and utilizing a gradient-based approach, which minimizes this function.

Recall from the beginning of Section 2.3 that the objective of the controller is to make the active and reactive powers, P and Q, track some desired references, P_d and Q_d, as closely as possible. In the MPT mode, where the goal is to generate as much active power as possible while maintaining an acceptable power factor, P_d is set to a value that far exceeds what the wind turbine can possibly produce (e.g., in the per-unit system, $P_d > 1$), while Q_d is set to a value representing the desired power factor $\mathrm{PF}_d = \frac{P_d}{\sqrt{P_d^2+Q_d^2}}$. In this mode, making P and Q approach P_d and Q_d is equivalent to maximizing the active power output while preserving the power factor. In the PR mode, where the goal is to regulate the powers, both P_d and Q_d are set to values representing power demands from the grid. In this mode, making P and Q approach P_d and Q_d amounts to achieving power regulation. Hence, the values of P_d and Q_d reflect the mode the wind farm operator wants the wind turbine to operate in. However, as far as the controller is concerned, it does not distinguish between the two modes; all it does is try its best to drive P and Q to P_d and Q_d.

To mathematically describe the aforementioned controller objective, consider the following positive definite, quadratic Lyapunov-like function V of the differences $P - P_d$ and $Q - Q_d$:

$$V = \frac{1}{2} \begin{bmatrix} P - P_d & Q - Q_d \end{bmatrix} \underbrace{\begin{bmatrix} w_p & w_{pq} \\ w_{pq} & w_q \end{bmatrix}}_{>0} \begin{bmatrix} P - P_d \\ Q - Q_d \end{bmatrix}, \tag{2.60}$$

where w_p, w_q, and w_{pq} are design parameters that allow one to specify how the differences $P - P_d$ and $Q - Q_d$, as well as their correlation $(P - P_d)(Q - Q_d)$, should be penalized. With this V, the above controller objective can be restated simply as: *make* V *go to zero*, because when this happens, P and Q must both go to P_d and Q_d. Since it is not always possible to achieve this objective—due to the fact that the wind may not always be strong enough—below we will attempt instead to *make* V *as small as possible by minimizing it.*

To minimize V, we first show that V is a function of ω_{rd}, θ, β, V_w, P_d, and Q_d, i.e.,

$$V = f(\omega_{rd}, \theta, \beta, V_w, P_d, Q_d) \tag{2.61}$$

for some f. Note from (2.60) that V depends on P, Q, P_d, and Q_d. Also note from (2.17)–(2.20), (2.21), and (2.22) that P and Q, in turn, depend on i, v_{dr}, and v_{qr} (recall that v_{ds} and v_{qs} are constants). Thus,

$$V = f_1(i, v_{dr}, v_{qr}, P_d, Q_d) \tag{2.62}$$

for some f_1. Next, note from (2.9)–(2.12) that i depends on φ; from (2.29) and (2.30) that v_{dr} and v_{qr} depend on φ, ω_r, u_1, and u_2; and from (2.32) that φ further depends on u_1 and u_2. Hence,

$$(i, v_{dr}, v_{qr}) = f_2(\omega_r, u_1, u_2) \tag{2.63}$$

for some f_2. Furthermore, note from (2.47) and (2.48) that u_1 and u_2 depend on r and θ, where r, in turn, depends on ω_r, ω_{rd}, β, and V_w through (2.55). Therefore,

$$(u_1, u_2) = f_3(\omega_r, \omega_{rd}, \theta, \beta, V_w) \tag{2.64}$$

for some f_3. Finally, assuming that ω_{rd} does not exceed the first root $\omega_r^{(1)}$ and assuming that ω_{rd}, β, and V_w are all relatively slow-varying (see below for a discussion), Theorem 2.1 says that ω_r goes to ω_{rd}. Thus, after a short transient,

$$\omega_r \approx \omega_{rd}. \tag{2.65}$$

Combining (2.62)–(2.65), (2.61) is obtained as claimed.

Now observe that the first three variables $(\omega_{rd}, \theta, \beta)$ in (2.61) are yet to be determined, while the last three variables (V_w, P_d, Q_d) are exogenous but known. Therefore, for each given (V_w, P_d, Q_d), $(\omega_{rd}, \theta, \beta)$ can be chosen correspondingly in order to minimize V. This defines a mapping from (V_w, P_d, Q_d) to $(\omega_{rd}, \theta, \beta)$, i.e.,

$$(\omega_{rd}, \theta, \beta) = F(V_w, P_d, Q_d) \triangleq \arg\min_{(x_1,x_2,x_3)} f(x_1,x_2,x_3,V_w,P_d,Q_d). \tag{2.66}$$

In principle, the mapping F in (2.66) may be constructed either *analytically*, by setting the gradient of $f(\cdot)$ to zero and solving for the minimizer $(\omega_{rd}, \theta, \beta)$ in terms of (V_w, P_d, Q_d), or *numerically*, by means of a three-dimensional lookup table. Unfortunately, the former is difficult to carry out, since f, being composed of several nonlinear transformations (2.62)–(2.65), has a rather complex expression. On the other hand, the latter is costly to generate and can easily become obsolete due to variations in system parameters. More important, selecting $(\omega_{rd}, \theta, \beta)$ as a *static* function of (V_w, P_d, Q_d) as in (2.66) may lead to steep jumps in $(\omega_{rd}, \theta, \beta)$ because V_w is ever-changing and may change dramatically, and both P_d and Q_d from the wind farm operator may experience step changes. Such steep jumps are undesirable because large fluctuations in ω_{rd} may prevent ω_r from tracking it, while discontinuous changes in β may be mechanically impossible to realize, cause intolerable vibrations, and substantially cut short the lifetime of the turbine blades.

To alleviate the aforementioned deficiencies of selecting $(\omega_{rd}, \theta, \beta)$ according to (2.66), a gradient-based approach is considered for updating $(\omega_{rd}, \theta, \beta)$:

$$\dot{\omega}_{rd} = -\epsilon_1 \frac{\partial f}{\partial \omega_{rd}}, \tag{2.67}$$

$$\dot{\theta} = -\epsilon_2 \frac{\partial f}{\partial \theta}, \tag{2.68}$$

$$\dot{\beta} = -\epsilon_3 \frac{\partial f}{\partial \beta}, \tag{2.69}$$

where $\epsilon_1, \epsilon_2, \epsilon_3 > 0$ are design parameters, which are meant to be relatively small, especially ϵ_1 and ϵ_3, in order to avoid steep changes in ω_{rd} and β. The partial derivatives $\frac{\partial f}{\partial \omega_{rd}}$, $\frac{\partial f}{\partial \theta}$, and $\frac{\partial f}{\partial \beta}$ in (2.67)–(2.69) can be calculated in a straightforward manner using (2.62)–(2.65), but are omitted from this chapter due to space limitations. These partial derivatives are practically implementable since, like f, they depend on ω_{rd}, θ, β, V_w, P_d, and Q_d, all of which are known. With this gradient-based approach, $(\omega_{rd}, \theta, \beta)$ is guaranteed to asymptotically converge to a local minimum when (V_w, P_d, Q_d) is constant, and track a local minimum when (V_w, P_d, Q_d) varies.

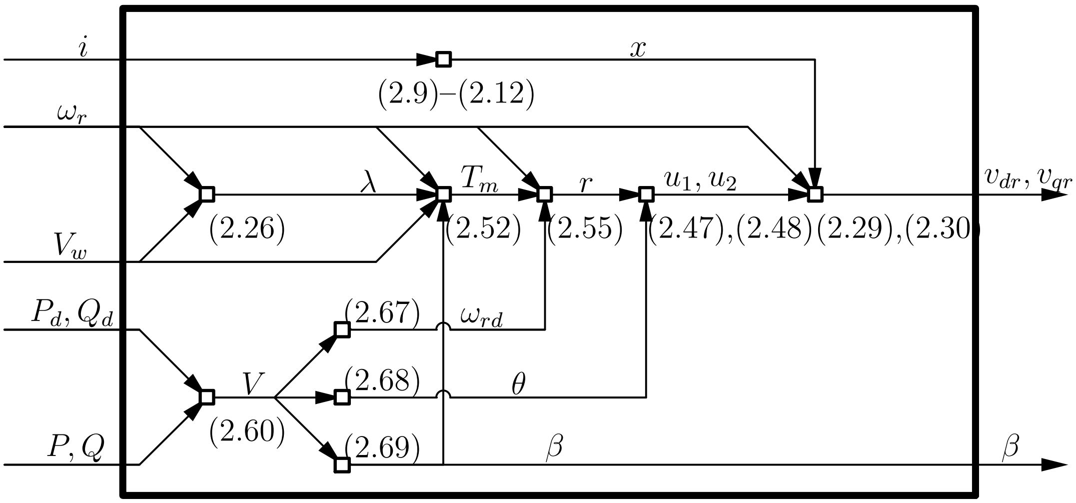

Figure 2.4: Internal structure of the proposed nonlinear controller.

To help the readers better understand the proposed nonlinear controller depicted in Figure 2.2 and described in this section, the internal structure of this controller is revealed in Figure 2.4. Observe that each arrow in this figure represents a signal, whereas each tiny box represents equations relating the signals.

2.4 Simulation Studies

To demonstrate the effectiveness of the controller presented above, MATLAB simulations have been carried out. To describe settings and results of the simulations, both the per-unit system and the physical unit system will be used, given that they are popular in the literature.

The simulation settings are as follows: we consider a 1.5 MW, 575 V, 60 Hz wind turbine that is essentially adopted from the Distributed Resources Library in MATLAB/Simulink R2007a. The values of the wind turbine parameters are: $\omega_s = 1\,\text{pu}$, $R_s = 0.00706\,\text{pu}$, $R_r = 0.005\,\text{pu}$, $L_s = 3.071\,\text{pu}$, $L_r =$

3.056 pu, $L_m = 2.9\,\text{pu}$, $v_{ds} = 1\,\text{pu}$, $v_{qs} = 0\,\text{pu}$, $J = 10.08\,\text{pu}$, $A = 4656.6\,\text{m}^2$, $R = 38.5\,\text{m}$, $\beta_{\min} = 0\,\text{deg}$, $\beta_{\max} = 30\,\text{deg}$, and $C_f = 0.01\,\text{pu}$. The C_p-surface adopted by MATLAB, which is taken from [68], is

$$C_p(\lambda, \beta) = c_1\Big(\frac{c_2}{\lambda_i} - c_3\beta - c_4\Big)e^{\frac{-c_5}{\lambda_i}} + c_6\lambda, \tag{2.70}$$

where

$$\frac{1}{\lambda_i} = \frac{1}{\lambda + 0.08\beta} - \frac{0.035}{\beta^3 + 1}, \tag{2.71}$$

$c_1 = 0.5176$, $c_2 = 116$, $c_3 = 0.4$, $c_4 = 5$, $c_5 = 21$, and $c_6 = 0.0068$. The mechanical power captured by the wind turbine is

$$P_m(\text{pu}) = \frac{P_{\text{nom}} P_{\text{wind\_base}}}{P_{\text{elec\_base}}}\, C_p(\text{pu})\, V_w(\text{pu})^3, \tag{2.72}$$

where $P_m(\text{pu}) = \frac{P_m}{P_{\text{nom}}}$, $P_{\text{nom}} = 1.5\,\text{MW}$ is the nominal mechanical power, $P_{\text{wind\_base}} = 0.73\,\text{pu}$ is the maximum power at the base wind speed, $P_{\text{elec\_base}} = 1.5 \times 10^6/0.9\,\text{VA}$ is the base power of the electrical generator, $C_p(\text{pu}) = \frac{C_p}{C_{p\text{\_nom}}}$, $C_{p\text{\_nom}} = 0.48$ is the peak of the C_p-surface, $V_w(\text{pu}) = \frac{V_w}{V_{w\text{\_base}}}$, and $V_{w\text{\_base}} = 12\,\text{m/s}$ is the base wind speed. Note that the maximum mechanical power, captured at the base wind speed, is 0.657 pu. The tip speed ratio is $\lambda(\text{pu}) = \frac{\frac{\omega_r(\text{pu})}{\omega_{r\text{\_base}}}}{V_w(\text{pu})}$, where $\lambda(\text{pu}) = \frac{\lambda}{\lambda_{\text{nom}}}$, $\lambda_{\text{nom}} = 8.1$ is the λ that yields the peak of the C_p-surface, $\omega_{r\text{\_base}} = 1.2\,\text{pu}$ is the base rotational speed, $\omega_r(\text{pu}) = \frac{\omega_r}{\omega_{r\text{\_nom}}}$, and $\omega_{r\text{\_nom}} = 2.1039\,\text{rad/sec}$ is the nominal rotor angular velocity. For more details on these parameters and values, see the MATLAB documentation.

For the proposed controller, we let the desired poles of the electrical dynamics (2.31) be located at -15, -5, and $-10 \pm 5j$, so that the corresponding state feedback gain matrix K, calculated using MATLAB's `place()` function, is

$$K = \begin{bmatrix} 5135.9 & 259.2 & 20.3 & 1.9 \\ -2676.7 & 4289.9 & -1.3 & 19.7 \end{bmatrix}.$$

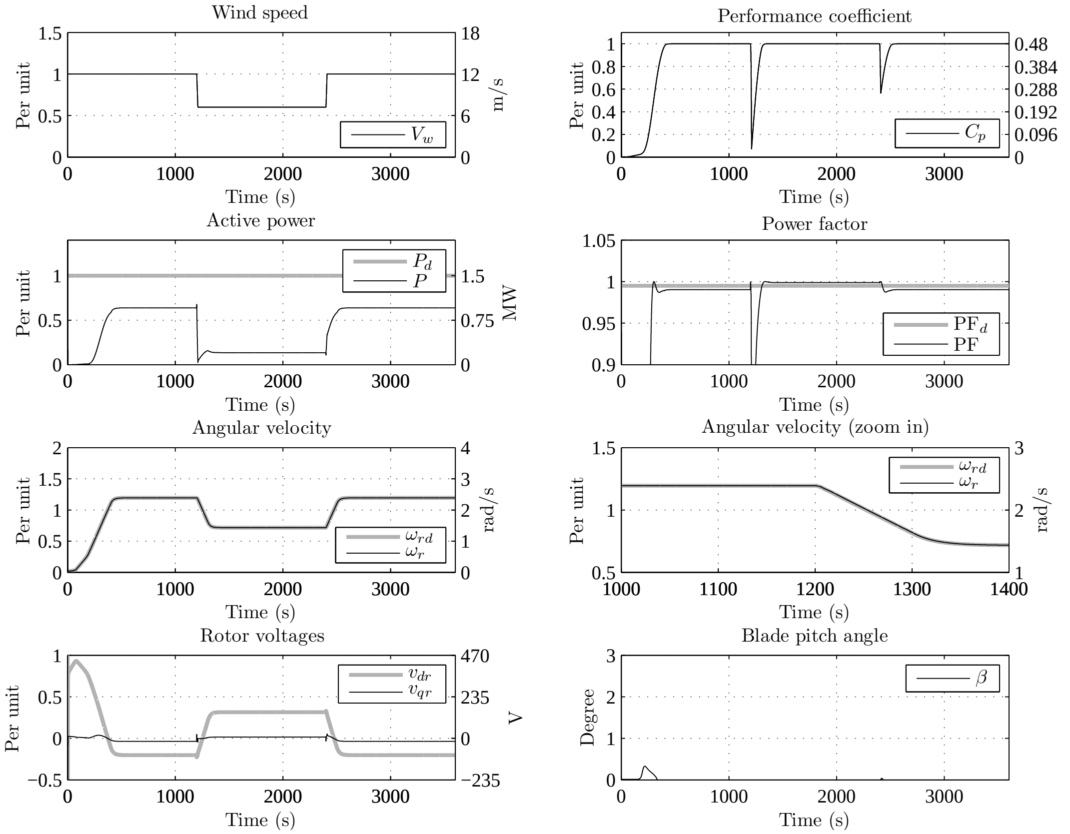

Figure 2.5: Scenario 1 illustrating the maximum power tracking (MPT) mode.

In addition, we let $w_p = 10$, $w_q = 1$, and $w_{pq} = 0$, implying that we penalize the difference between P and P_d much more than we do Q and Q_d. Finally, we choose the rest of the controller parameters as follows: $\alpha = 10$, $\epsilon_1 = 4 \times 10^{-3}$, $\epsilon_2 = 1 \times 10^{-4}$, and $\epsilon_3 = 2$.

Based on the above wind turbine and controller parameters, simulations have been carried out for four different scenarios. Description of each scenario, along with the simulation result, is given below:

Scenario 1: *Maximum power tracking (MPT) mode.* In this scenario, we simulate the situation where the wind speed V_w experiences step changes between 12 m/s and 7.2 m/s, while the desired powers P_d and Q_d are kept constant at 1.5 MW and 0.15 MW, so that the desired power factor is $\text{PF}_d = 0.995$. Since P_m cannot exceed 0.657×1.5 MW at the base wind speed $V_{w\_\text{base}} = 12$ m/s, the wind turbine is expected to operate in the MPT mode. Figure 2.5 shows the simulation result for this scenario, where the key signals are plotted as functions of time in both the per-unit and physical unit systems wherever applicable. Observe that, after a short transient, the wind turbine converts as much wind energy to electric energy as it possibly could, as indicated by C_p approaching its maximum value of 0.48 in subplot 2 (which translates into P approaching its maximum possible value in subplot 3). Also observe that, when V_w goes from 12 m/s to 7.2 m/s and from 7.2 m/s back to 12 m/s, C_p drops sharply but quickly returns to its maximum value. Note from subplot 4 that, regardless of V_w, the power factor PF is maintained near the desired level of 0.995. Moreover, note from subplots 5 and 6 that the angular velocity ω_r tracks the desired time-varying reference ω_{rd} closely (subplot 6 is a zoom-in version of subplot 5). Finally, the control inputs v_{dr}, v_{qr}, and β are shown in subplots 7 and 8, respectively. Note that, to maximize C_p, β is kept at its minimum value $\beta_{\min} = 0$ deg.

Scenario 2: *Power regulation (PR) mode.* In this scenario, we simulate the situation where V_w is kept constant at the base value of 12 m/s, while P_d experiences step changes from 0.45 MW to 0.3 MW and then to 0.6 MW, and Q_d is such that $\text{PF}_d = 0.995$. Since P_d is always less than 0.657×1.5 MW at the base wind speed of 12 m/s, the wind turbine is expected to operate in the PR mode with different setpoints P_d. Figure 2.6 shows the simulation result for this scenario. Observe from subplot 2 that C_p is less than its maximum value of 0.48. This suggests that the wind turbine attempts to capture less power than what it possibly could from wind, since P_d is relatively small. Indeed, as

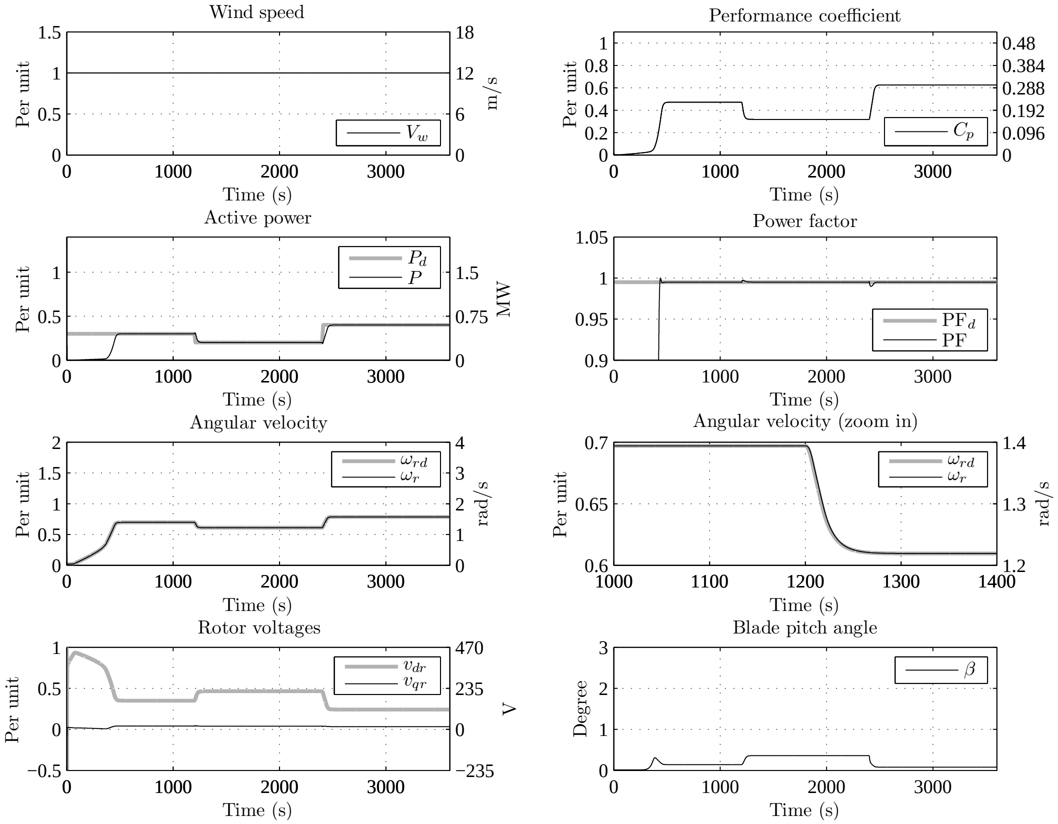

Figure 2.6: Scenario 2 illustrating the power regulation (PR) mode.

can be seen from subplots 3 and 4, the turbine produces just enough active and reactive powers, making P track P_d closely while maintaining PF at PF$_d$. Also observe from subplots 5 and 6 that ω_r closely follows ω_{rd}, as desired. Finally, note from subplot 8 that β increases slightly in order to capture less power between 1200s and 2400s, when P_d is smallest.

Scenario 3: *Seamless switching between the MPT and PR modes.* In this scenario, we simulate the situation where P_d experiences large step changes between 1.5 MW and 0.75 MW, Q_d again is such that PF$_d$ is 0.995, and an actual wind profile from a wind farm located in northwest Oklahoma is used to define V_w. The actual wind profile consists of 145 samples, taken at the

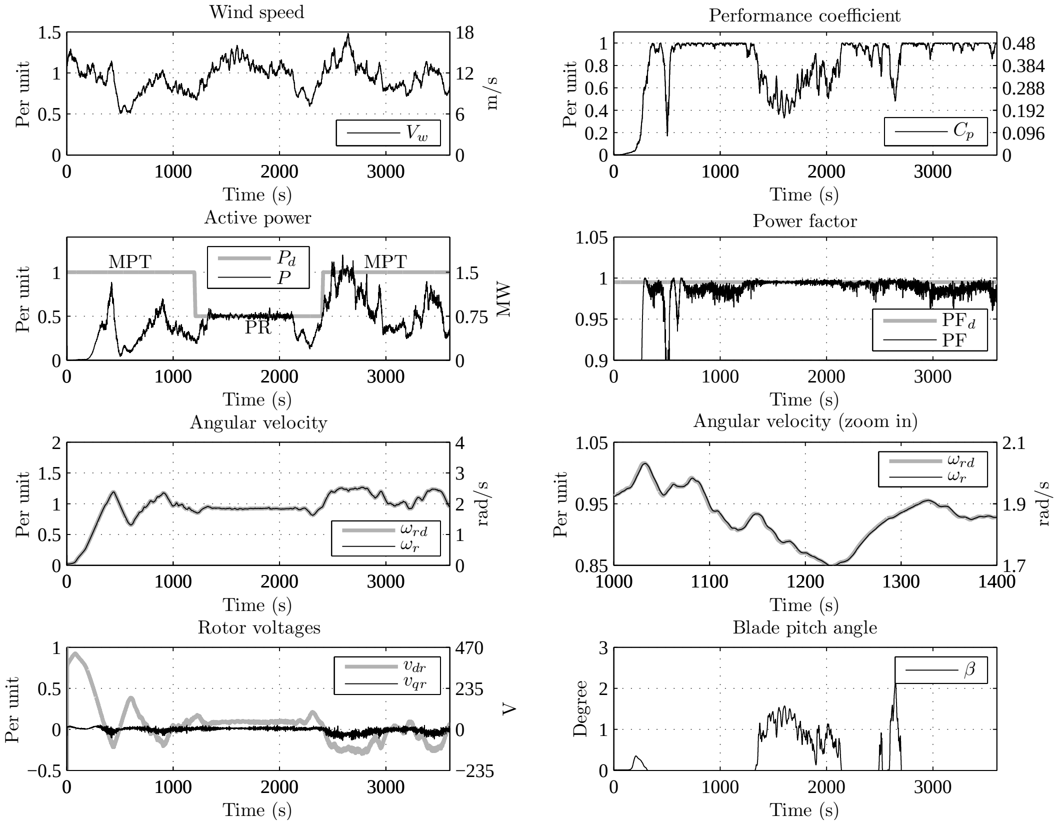

Figure 2.7: Scenario 3 illustrating the seamless switching between the MPT and PR modes under an actual wind profile from a wind farm located in northwest Oklahoma.

rate of one sample per 10 minutes, over a 24-hour period. In order to use this wind profile in a 1-hour simulation (as in Scenarios 1 and 2), we compress the time scale, assuming that the samples were taken over a 1-hour period. Note that compressing the time scale in this way makes the problem more challenging because the wind speed varies faster than it actually does. Figure 2.7 shows the simulation result for this scenario, with subplot 1 displaying the wind profile. Observe from subplots 2 and 3 that, for the first 1200 seconds during which P_d is 1.5 MW, the turbine operates in the MPT mode, grabbing as much wind energy as it possibly could, by driving C_p to 0.48 and maximizing P. At time 1200s when P_d abruptly drops from 1.5 MW to 0.75 MW, the turbine seamlessly

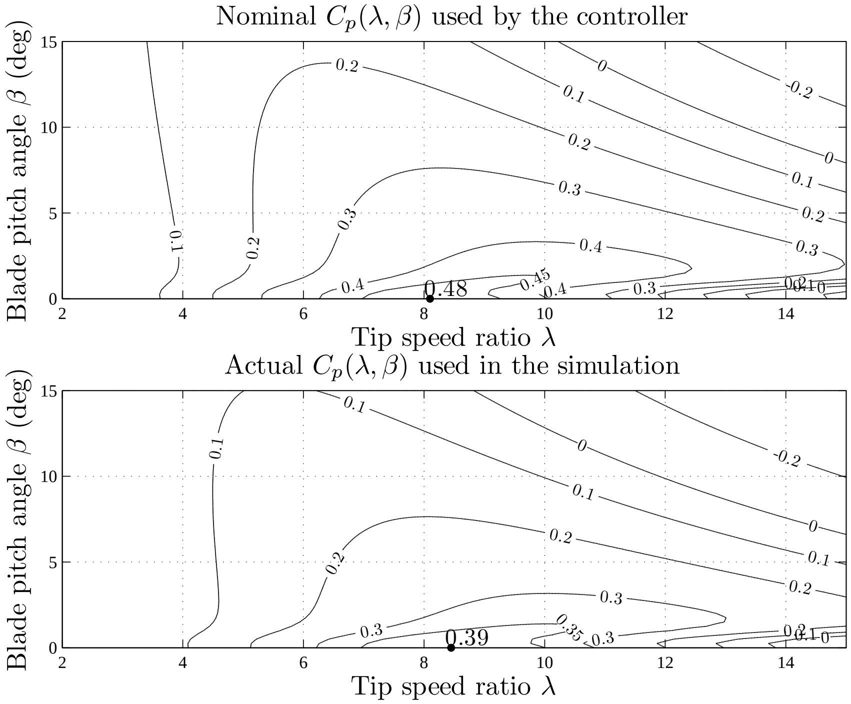

Figure 2.8: Contour plots of the nominal and actual $C_p(\lambda, \beta)$ for Scenario 4.

switches from the MPT mode to the PR mode, quickly reducing C_p, accurately regulating P around P_d, and effectively rejecting the "disturbance" V_w. Note that between 2100s and 2400s, the wind is not strong enough to sustain the PR mode. As a result, the MPT mode resumes seamlessly, as indicated by C_p returning immediately to its maximum value of 0.48. Finally, at time 2400s when P_d goes from 0.75 MW back to 1.5 MW, the turbine keeps working in the MPT mode, continuing to maximize both C_p and P. Notice from subplots 4–6 that, over the course of the simulation, both PF and ω_r are maintained at PF_d and ω_{rd}, respectively, despite the random wind fluctuations. Also notice from subplot 8 that β increases somewhat during the PR mode in order to help capture less power.

Scenario 4: *Robustness of the proposed controller.* In this scenario, we simulate the exact same situation as that of Scenario 3 (i.e., with the same V_w, P_d, and Q_d) but with modeling errors and measurement noise. That is, we allow for modeling errors in the friction coefficient C_f and the performance coefficient C_p (due, for example, to changing weather conditions, blade erosions, and aging) as well as measurement noise in the wind speed V_w (since V_w is usually measured by an anemometer located on the nacelle behind the blades of a wind turbine). Specifically, we assume that the nominal C_f used by the controller is 0.01(pu), whereas the actual C_f used in the simulation is 0.012(pu), so that C_f has a 20% modeling error. Moreover, we assume that the nominal C_p used by the controller is given by (2.70) and (2.71) with $c_1 = 0.5176$, $c_2 = 116$, $c_3 = 0.4$, $c_4 = 5$, $c_5 = 21$, and $c_6 = 0.0068$, whereas the actual C_p used in the simulation is also given by (2.70) and (2.71) but with $c_1 = 0.45$, $c_2 = 115$, $c_3 = 0.5$, $c_4 = 4.5$, $c_5 = 22$, and $c_6 = 0.003$. Figure 2.8 displays the contour plots of the nominal and actual $C_p(\lambda, \beta)$ for $\lambda \in [2, 15]$ and $\beta \in [0, 15]$, showing that C_p has noticeable modeling errors. In particular, the nominal C_p attains its maximum of 0.48 at $(\lambda, \beta) = (8.1, 0)$, whereas the actual C_p attains its maximum of 0.39 at $(\lambda, \beta) = (8.45, 0)$. Finally, we assume that the measured V_w used by the controller, denoted as V_{w_meas}, is related to the actual V_w used in the simulation via

$$V_{w\_\text{meas}}(t) = V_w(t) + 0.5 + 0.5\sin(0.5t) + 0.25\cos(t),$$

where the second term on the right-hand side represents a constant measurement bias, while the third and fourth represent measurement noises with different amplitudes and frequencies. Figure 2.9 shows the simulation result for this scenario. Comparing this figure with Figure 2.7, the following observations can be made: first, C_p in Figure 2.9 attains its maximum value of 0.39 in the MPT

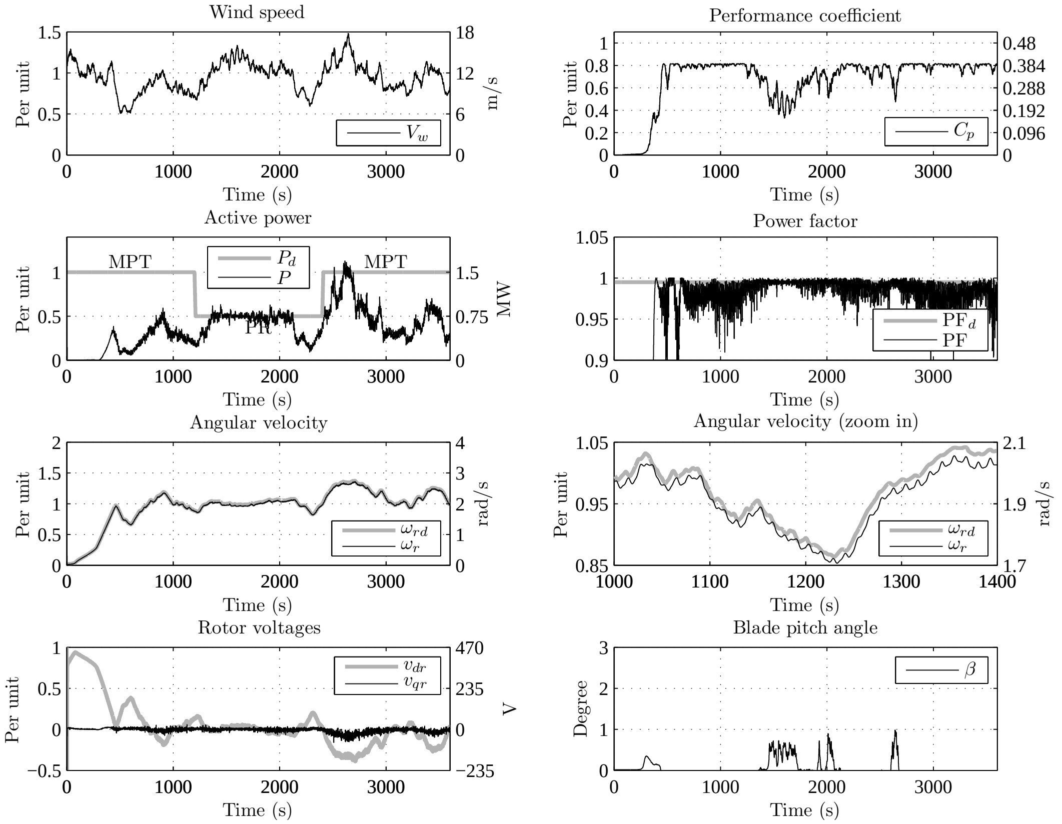

Figure 2.9: Scenario 4 illustrating the robustness of the proposed controller to modeling errors in C_f and C_p and noisy measurements in V_w.

mode, as opposed to the 0.48 attained by C_p in Figure 2.7. Second, PF in Figure 2.9 has a larger fluctuation compared to PF in Figure 2.7, but nonetheless is maintained around PF_d. Third, ω_r in Figure 2.9 does not track ω_{rd} as closely as ω_r in Figure 2.7 does. Nevertheless, despite the wind fluctuations, modeling errors, and noisy measurements, the controller performs reasonably well, as evident by how close C_p is to its maximum value of 0.39 in the MPT mode, how close P is to P_d in the PR mode, and how close PF is to PF_d throughout the simulation. Therefore, the controller is fairly robust.

As it follows from Figures 2.5–2.9 and the above discussions, the proposed controller exhibits excellent performance. Specifically, the controller works well in both the MPT mode under step changes in the wind speed (Scenario 1) and the PR mode under step changes in the power commands (Scenario 2). In addition, it is capable of seamlessly switching between the two modes in the presence of changing power commands and a realistic, fluctuating wind profile (Scenario 3). Finally, the controller is robust to small modeling errors and noisy measurements commonly encountered in practice (Scenario 4).

2.5 Conclusion

In this chapter, we have developed a feedback/feedforward nonlinear controller, which accounts for the nonlinearities of variable-speed wind turbines with doubly fed induction generators, and bypasses the need for approximate linearization. Its development is based on applying a mixture of linear and nonlinear control design techniques on three time scales, including feedback linearization, pole placement, and gradient-based minimization of a Lyapunov-like potential function. Simulation results have shown that the proposed scheme not only effectively controls the active and reactive powers in both the MPT and PR modes, it also ensures seamless switching between the two modes. Therefore, the proposed controller may be recommended as a candidate for future wind turbine control.

Chapter 3 Voltage/Pitch Control for Maximization and Regulation of Active/Reactive Powers in Wind Turbines with Uncertainties

3.1 Introduction

In the previous chapter, we developed a nonlinear controller that simultaneously enables control of the active power in both the MPT and PR modes, seamless switching between the two, and control of the reactive power so that a desirable power factor is maintained. These objectives were achieved by adjusting the rotor voltages of the electrical part and the blade pitch angle of the mechanical part, where the coupling between the two parts were taken into account in the controller design. Like most of the existing work in wind turbine control, however, the controller assumed that the aerodynamic and mechanical parameters were known.

In this chapter, we develop a controller that achieves such objectives and, at the same time, addresses the two aforementioned challenges, on uncertainties in the aerodynamic and mechanical parameters, and coupling between the mechanical and electrical parts. For the former, we show that the parametric uncertainties can be lumped into a scalar term, estimated via an uncertainty estimator in an inner loop, and circumvented in an outer, gradient-based minimization loop. For the latter, we show that the electromechanical coupling can be eliminated via feedback linearization on the electrical dynamics, following ideas from the previous chapter. Finally, we analyze the controller developed and demonstrate its effectiveness through simulation with realistic wind profiles from a wind farm in Oklahoma.

The outline of this chapter is as follows: Section 3.2 formulates the problem. Section 3.3 describes the proposed controller. Section 3.4 presents the simulation results. Finally, Section 3.5 concludes this chapter.

3.2 Problem Formulation

Given the wind turbine model described in Section 2.2, the problem addressed in this chapter is: design a feedback controller, so that the active and reactive powers P and Q closely track some desired, possibly time-varying references P_d and Q_d, assumed to be provided by a wind farm operator. When P_d is larger than what the wind turbine is capable of generating, it means that the operator wants the turbine to operate in the MPT mode; otherwise, the PR mode is sought. By also providing Q_d, the operator indirectly specifies a desired power factor $\text{PF}_d = \frac{P_d}{\sqrt{P_d^2+Q_d^2}}$, around which the actual power factor $\text{PF} = \frac{P}{\sqrt{P^2+Q^2}}$ should be regulated. The controller may use i, ω_r, P, and Q, which are all measurable, as feedback. The fluxes φ may also be viewed as feedback, since they are bijectively related to i through (2.5)–(2.8). Moreover, the controller may use values of all the electrical parameters (i.e., ω_s, R_s, R_r, L_s, L_r, L_m, v_{ds}, and v_{qs}) and turbine-geometry-dependent parameters (i.e., J, A, R, $\beta_{\min}$, and $\beta_{\max}$), since these values are typically quite accurately known. However, it may not use values of the C_p-surface, the air density ρ, and the friction coefficient C_f, since these values are inherently uncertain and can change over time. Furthermore, the controller should not rely on the wind

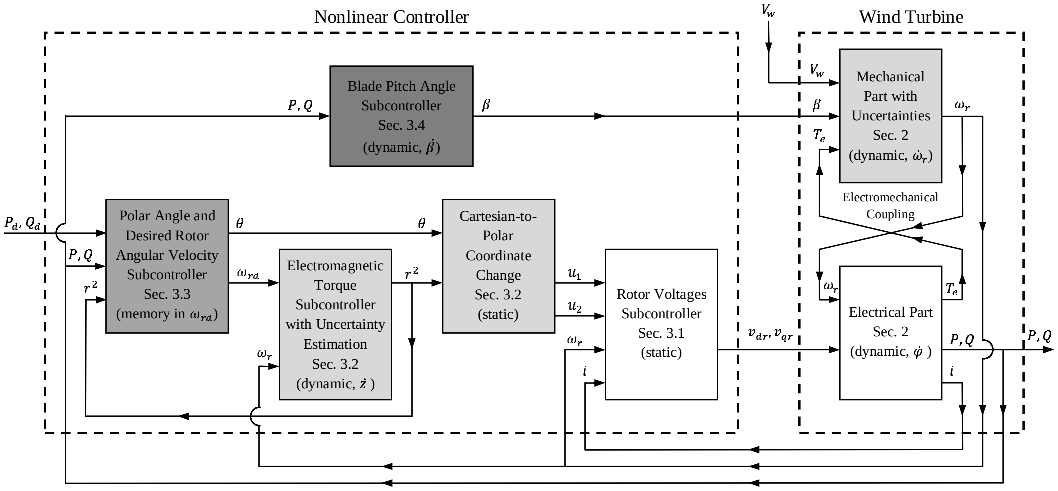

Figure 3.1: Model of the wind turbine and architecture of the nonlinear controller.

speed V_w, since it may not be accurately measured.

3.3 Controller Design

In this section, we address the aforementioned problem by developing a nonlinear controller consisting of four subcontrollers. Figure 3.1 shows the architecture of the nonlinear controller, which accepts P_d and Q_d as reference inputs, uses i, ω_r, P, and Q as feedback, and produces v_{dr}, v_{qr}, and β as control inputs to the wind turbine. Moreover, the different gray levels of the blocks in Figure 3.1 represent our intended time-scale separation in the closed-loop dynamics: the darker a block, the slower its dynamics. The subcontrollers will be described in Sections 3.3.1–3.3.4.

3.3.1 Rotor Voltages Subcontroller

Observe that although the electrical dynamics (2.27) are nonlinear, they possess a nice structure: the first and second rows of (2.27) are affine, consisting of linear terms and the constants v_{ds} and v_{qs}, while the third and fourth are nonlinear, consisting of linear terms, the control variables v_{dr} and v_{qr}, and the nonlinearities $-\omega_r\varphi_{qr}$ and $\omega_r\varphi_{dr}$. Since the nonlinearities enter the dynamics the same way the control variables v_{dr} and v_{qr} do, we may use feedback linearization [66] to cancel them and perform pole placement [67], i.e., let

$$v_{dr} = \omega_r\varphi_{qr} - K_1^T\varphi + u_1, \tag{3.1}$$

$$v_{qr} = -\omega_r\varphi_{dr} - K_2^T\varphi + u_2, \tag{3.2}$$

where $\omega_r\varphi_{qr}$ and $-\omega_r\varphi_{dr}$ are intended to cancel the nonlinearities, $-K_1^T\varphi$ and $-K_2^T\varphi$ with $K_1, K_2 \in \mathbb{R}^4$ are for pole placement, and u_1 and u_2 are new control variables to be designed in Section 3.3.2.

Substituting (3.1) and (3.2) into (2.27), we get

$$\dot{\varphi} = (A - BK)\varphi + \begin{bmatrix} v_{ds} \; v_{qs} \; u_1 \; u_2 \end{bmatrix}^T, \tag{3.3}$$

where $K = [K_1 \quad K_2]^T$ is the state feedback gain matrix. Since the electrical dynamics are physically allowed to be much faster than the mechanicals, we may choose K in (3.3) to be such that $A - BK$ is asymptotically stable with very fast eigenvalues. With K chosen as such and with relatively slow-varying u_1 and u_2, the linear differential equation (3.3) may be approximated by a linear algebraic equation:

$$\varphi = -(A - BK)^{-1} \begin{bmatrix} v_{ds} \; v_{qs} \; u_1 \; u_2 \end{bmatrix}^T. \tag{3.4}$$

Consequently, the fifth-order state equations (2.27) and (2.23) may be approximated by the first-order state equation (2.23) along with algebraic relationships

(3.1), (3.2), and (3.4). This approximation will be made in all subsequent development (but not in simulation).

Note that (2.5)–(2.8), (3.1), and (3.2) describe the Rotor Voltages Subcontroller block in Figure 3.1.

3.3.2 Electromagnetic Torque Subcontroller with Uncertainty Estimation

Having addressed the electrical dynamics, we now consider the mechanicals, where the goal is to construct a subcontroller, which makes the rotor angular velocity ω_r track a desired, slow-varying reference ω_{rd}, despite not knowing the aerodynamic and mechanical parameters listed at the end of Section 3.2.

To come up with such a subcontroller, we first introduce a coordinate change. As was shown in the previous chapter, the electromagnetic torque T_e may be expressed as a quadratic function of the new control variables u_1 and u_2, i.e.,

$$T_e = \begin{bmatrix} u_1 & u_2 \end{bmatrix} \begin{bmatrix} q_1 & q_2 \\ q_2 & q_3 \end{bmatrix} \begin{bmatrix} u_1 \\ u_2 \end{bmatrix} + \begin{bmatrix} b_1 & b_2 \end{bmatrix} \begin{bmatrix} u_1 \\ u_2 \end{bmatrix} + a, \tag{3.5}$$

where q_1, q_2, q_3, b_1, b_2, and a depend on the electrical parameters and the state feedback gain matrix K. Moreover, this quadratic function is always convex because its associated Hessian matrix $\left[\begin{smallmatrix} q_1 & q_2 \\ q_2 & q_3 \end{smallmatrix}\right]$ is always positive definite. Since the mechanical dynamics (2.23), in ω_r, are driven by T_e, while T_e in (3.5) is a quadratic function of u_1 and u_2, the two new control variables u_1 and u_2 collectively affect one state variable ω_r. This implies that there is a redundancy in u_1 and u_2. Since the quadratic function is always convex, this redundancy may be exposed via the following coordinate change:

$$r = \sqrt{z_1^2 + z_2^2}, \quad \theta = \operatorname{atan2}(z_2, z_1), \tag{3.6}$$

where

$$\begin{bmatrix} z_1 \\ z_2 \end{bmatrix} = D^{1/2} M^T \begin{bmatrix} u_1 \\ u_2 \end{bmatrix} + \frac{1}{2} D^{-1/2} M^T \begin{bmatrix} b_1 \\ b_2 \end{bmatrix}, \tag{3.7}$$

atan2() denotes the four-quadrant arctangent function, and M and D contain the eigenvectors and eigenvalues of $\left[\begin{smallmatrix} q_1 & q_2 \\ q_2 & q_3 \end{smallmatrix}\right]$ on their columns and diagonal, respectively. In the polar coordinates, it follows from (3.5)–(3.7) that

$$T_e = r^2 + a', \tag{3.8}$$

where $a' = -\frac{v_{ds}^2 + v_{qs}^2}{4\omega_s R_s}$ is always negative. From (2.23) and (3.8), we see that in the polar coordinates, r^2 is responsible for driving the mechanical dynamics in ω_r and, hence, may be viewed as an equivalent electromagnetic torque, differed from T_e only by a constant a'. On the other hand, the polar angle θ has no impact on the mechanical dynamics and, thus, represents the redundancy that will be exploited later, in Section 3.3.3.

Note that (3.6) and (3.7) describe the Cartesian-to-Polar Coordinate Change block in Figure 3.1.

Having introduced the coordinate change, we next show that the unknown aerodynamic and mechanical parameters can be lumped into a scalar term, simplifying the problem. Combining (2.23), (2.25), (2.26), and (2.49),

$$J\dot{\omega}_r = \frac{\frac{1}{2}\rho A C_p(\frac{\omega_r R}{V_w}, \beta) V_w^3}{\omega_r} - r^2 - a' - C_f \omega_r. \tag{3.9}$$

Notice that the unknown parameters—namely, the C_p-surface, the air density ρ, the friction coefficient C_f, and the wind speed V_w—all appear in (3.9). Moreover, these unknown parameters can be separated from the "control input" r^2 and lumped into a scalar function $g(\omega_r, \beta, V_w)$, defined in (2.56) and rewritten as

$$g(\omega_r, \beta, V_w) = \frac{\frac{1}{2}\rho A C_p(\frac{\omega_r R}{V_w}, \beta) V_w^3}{\omega_r} - a' - C_f \omega_r. \tag{3.10}$$

With $g(\omega_r, \beta, V_w)$ in (3.10) representing the aggregated uncertainties, the first-order dynamics (3.9) are simplified to

$$\dot{\omega}_r = \frac{1}{J}(g(\omega_r, \beta, V_w) - r^2). \tag{3.11}$$

To design a controller, which allows the rotor angular velocity ω_r to track a desired, slow-varying reference ω_{rd} despite the unknown scalar function $g(\omega_r, \beta, V_w)$, consider a first-order nonlinear system

$$\dot{x} = \frac{1}{J}(f(x) + u), \tag{3.12}$$

where $x \in \mathbb{R}$ is the state, $u \in \mathbb{R}$ is the input, and $f(x)$ is a known function of x. Obviously, to drive x to some desired value $x_d \in \mathbb{R}$, we may apply feedback linearization [66] to cancel $f(x)$ and insert linear dynamics, i.e., let

$$u = -f(x) - \alpha(x - x_d), \tag{3.13}$$

where $\alpha \in \mathbb{R}$ is the controller gain. Combining (3.12) with (3.13) yields the closed-loop dynamics

$$\dot{x} = -\frac{\alpha}{J}(x - x_d). \tag{3.14}$$

Thus, if α is positive, x in (3.14) asymptotically goes to x_d.

Now suppose $f(x)$ in (3.12) is unknown but a constant, denoted simply as $f \in \mathbb{R}$ (we will relax the assumption that it is a constant shortly). With f being unknown, the controller (3.13) is no longer applicable. To overcome this limitation, we may first introduce a reduced-order estimator [69], which calculates an estimate $\hat{f} \in \mathbb{R}$ of f, and then replace $f(x)$ in (3.13) by the estimate $\hat{f}$:

$$\dot{z} = -\frac{h}{J}(u + \hat{f}), \tag{3.15}$$

$$\hat{f} = z + hx, \tag{3.16}$$

$$u = -\hat{f} - \alpha(x - x_d), \tag{3.17}$$

where $z \in \mathbb{R}$ is the estimator state and $h \in \mathbb{R}$ is the estimator gain. Defining the estimation error as $\tilde{f} = f - \hat{f}$ and combining (3.12) with (3.15)–(3.17) yield closed-loop dynamics

$$\dot{\tilde{f}} = -\dot{\hat{f}} = -\dot{z} - h\dot{x} = -\frac{h}{J}\tilde{f}, \tag{3.18}$$

$$\dot{x} = \frac{1}{J}(f - \hat{f} - \alpha(x - x_d)) = \frac{1}{J}(\tilde{f} - \alpha(x - x_d)). \tag{3.19}$$

Hence, by letting both α and h be positive, both $\tilde{f}$ and x in (3.18) and (3.19) asymptotically go to 0 and x_d, respectively.

Next, suppose both the state x and the desired value x_d must be positive, instead of being anywhere in $\mathbb{R}$. With this restriction, the controller with uncertainy estimation (3.15)–(3.17) needs to be modified, because for some initial conditions, it is possible that x can become nonpositive. One way to modify the controller is to replace the linear term $x - x_d$ in (3.17) by a logarithmic one $\ln \frac{x}{x_d}$, resulting in

$$u = -\hat{f} - \alpha \ln \frac{x}{x_d}. \tag{3.20}$$

With (3.15), (3.16), and (3.20), the closed-loop dynamics become

$$\dot{\tilde{f}} = -\frac{h}{J}\tilde{f}, \tag{3.21}$$

$$\dot{x} = \frac{1}{J}(\tilde{f} - \alpha \ln \frac{x}{x_d}). \tag{3.22}$$

Note from (3.22) that for any $\tilde{f} \in \mathbb{R}$, there exists positive x, sufficiently small, such that $\dot{x}$ is positive. Therefore, for any initial condition $(\tilde{f}(0), x(0))$ with positive $x(0)$, $x(t)$ will remain positive, suggesting that the modification (3.20) satisfies the restriction.

Now suppose the input u must be nonpositive. With this additional restriction, (3.20) needs to be further modified. One way to do so is to force the right-hand side of (3.20) to be nonpositive, leading to

$$u = -\max\{\hat{f} + \alpha \ln \frac{x}{x_d}, 0\}. \tag{3.23}$$

Clearly, with (3.23), u is always nonpositive.

Finally, suppose f is an unknown function of x, denoted as $f(x)$. With this relaxation, we may associate the first-order nonlinear system (3.12) with the first-order dynamics (3.11) by viewing x as ω_r, x_d as ω_{rd}, u as $-r^2$, $f(x)$ as $g(\omega_r, \beta, V_w)$ (treating β and V_w as constants), and $\hat{f}$ as $\hat{g}$ (i.e., $\hat{g}$ is an estimate of $g(\omega_r, \beta, V_w)$). Based on this association, (3.15), (3.16), and (3.23) can be written as

$$\dot{z} = -\frac{h}{J}(-r^2 + \hat{g}), \tag{3.24}$$

$$\hat{g} = z + h\omega_r, \tag{3.25}$$

$$r^2 = \max\{\hat{g} + \alpha \ln \frac{\omega_r}{\omega_{rd}}, 0\}. \tag{3.26}$$

Having derived the controller with uncertainty estimation (3.24)–(3.26), we now analyze its behavior. To do so, some setup is needed: first, suppose ω_{rd}, β, and V_w are constants. Second, as was shown in Chapter 2, because of Assumptions (A1)–(A3) in Section 2.2, there exists $\omega_r^{(1)} \in (0, \infty)$ such that $g(\omega_r^{(1)}, \beta, V_w) = 0$ and $g(\omega_r, \beta, V_w) > 0$ for all $\omega_r \in (0, \omega_r^{(1)})$. Third, using

(2.26), (3.10), and Assumptions (A1) and (A4), it is straightforward to show that there exist $\underline{\gamma} \in (-\infty, 0)$ and $\overline{\gamma} \in (0, \infty)$ such that $\underline{\gamma} \leq \frac{\partial}{\partial \omega_r} g(\omega_r, \beta, V_w) \leq \overline{\gamma}$ for all $\omega_r \in (0, \infty)$. Finally, with (3.11) and (3.24)–(3.26) and with $(\omega_r, \hat{g})$ as state variables (instead of (ω_r, z)), the closed-loop dynamics can be expressed as

$$\dot{\omega}_r = \frac{1}{J}(g(\omega_r, \beta, V_w) - \max\{\hat{g} + \alpha \ln \frac{\omega_r}{\omega_{rd}}, 0\}), \tag{3.27}$$

$$\dot{\hat{g}} = \dot{z} + h\dot{\omega}_r = \frac{h}{J}(g(\omega_r, \beta, V_w) - \hat{g}). \tag{3.28}$$

The following theorem characterizes the stability properties of the closed-loop system (3.27) and (3.28):

Theorem 3.1. *Consider the closed-loop system* (3.27) *and* (3.28). *Suppose* ω_{rd}, β, *and* V_w *are constants with* $0 < \omega_{rd} \leq \omega_r^{(1)}$, *where* $\omega_r^{(1)}$, *along with* $\underline{\gamma}$ *and* $\overline{\gamma}$, *is as defined above. Let* $D = \{(\omega_r, \hat{g}) | 0 < \omega_r \leq \omega_r^{(1)}, \hat{g} \in \mathbb{R}\} \subset \mathbb{R}^2$. *If the controller gain* α *is positive and the estimator gain* h *is sufficiently large, i.e.,*

$$\begin{array}{ll} h > \overline{\gamma} & \textit{if} \quad \overline{\gamma} \geq -\frac{1}{3}\underline{\gamma}, \\ h > -\frac{(\overline{\gamma}-\underline{\gamma})^2}{8(\underline{\gamma}+\overline{\gamma})} & \textit{otherwise,} \end{array} \tag{3.29}$$

then: (i) the system has a unique equilibrium point at $(\omega_{rd}, g(\omega_{rd}, \beta, V_w))$ *in* D*; (ii) the set* D *is a positively invariant set, i.e., if* $(\omega_r(0), \hat{g}(0)) \in D$*, then* $(\omega_r(t), \hat{g}(t)) \in D \ \forall t \geq 0$*; and (iii) the equilibrium point* $(\omega_{rd}, g(\omega_{rd}, \beta, V_w))$ *is locally asymptotically stable with a domain of attraction* D.

Proof. First, we show (i). Setting $\dot{\omega}_r$ and $\dot{\hat{g}}$ in (3.27) and (3.28) to zero yields $g(\omega_r, \beta, V_w) = \max\{\hat{g} + \alpha \ln \frac{\omega_r}{\omega_{rd}}, 0\}$ and $\hat{g} = g(\omega_r, \beta, V_w)$. When $\hat{g} + \alpha \ln \frac{\omega_r}{\omega_{rd}} \geq 0$, we have $\omega_r = \omega_{rd}$ and $\hat{g} = g(\omega_{rd}, \beta, V_w)$. Thus, $(\omega_{rd}, g(\omega_{rd}, \beta, V_w))$ is an equilibrium point, which is in D, since $0 < \omega_{rd} \leq \omega_r^{(1)}$. On the other hand, when $\hat{g} + \alpha \ln \frac{\omega_r}{\omega_{rd}} < 0$, we have $\omega_r \in \Omega$ and $\hat{g} = 0$, where $\Omega = \{\omega \in (0, \infty) :$

$g(\omega, \beta, V_w) = 0\}$ and $\omega_r^{(1)} = \min \Omega$. Since $\hat{g} + \alpha \ln \frac{\omega_r}{\omega_{rd}} < 0$ and $\hat{g} = 0$, we have $\omega_r < \omega_{rd}$. Since $\omega_r \in \Omega$, $\omega_r^{(1)} = \min \Omega$, and $\omega_{rd} \leq \omega_r^{(1)}$, we have $\omega_r \geq \omega_{rd}$. Hence, there is a contradiction, implying that when $\hat{g} + \alpha \ln \frac{\omega_r}{\omega_{rd}} < 0$, there is no equilibrium point in D. This proves (i).

Next, we show (ii). To do so, it is useful to think of D as a vertical strip in the state space $(\omega_r, \hat{g})$. Notice that on the right boundary of the strip where $\omega_r = \omega_r^{(1)}$, because of (3.27) and because $g(\omega_r^{(1)}, \beta, V_w) = 0$ and $\max\{\hat{g} + \alpha \ln \frac{\omega_r^{(1)}}{\omega_{rd}}, 0\} \geq 0$, we have $\dot{\omega}_r \leq 0$. Thus, the state $(\omega_r, \hat{g})$ cannot escape D through the right boundary. Next, note that for each fixed $\hat{g} \in \mathbb{R}$, there exists $\omega_r^\star > 0$ such that for all $\omega_r \in (0, \omega_r^\star)$, $\hat{g} + \alpha \ln \frac{\omega_r}{\omega_{rd}} < 0$. This, along with (3.27) and the fact that $g(\omega, \beta, V_w) > 0$ for all $\omega \in (0, \omega_r^{(1)})$, implies that near the left boundary of the strip where ω_r is arbitrarily small but positive, we have $\dot{\omega}_r > 0$. Hence, the state $(\omega_r, \hat{g})$ cannot escape D through the left boundary. This proves (ii).

Finally, we show (iii). Consider a Lyapunov function candidate $V : D \to \mathbb{R}$, defined as $V(\omega_r, \hat{g}) = \alpha c(\omega_r \ln \frac{\omega_r}{\omega_{rd}} - \omega_r + \omega_{rd}) + \frac{1}{2}(g(\omega_r, \beta, V_w) - \hat{g})^2$, where $c > 0$ is to be determined. Note that V is continuously differentiable over D. Moreover, V is positive definite over D with respect to the equilibrium point $(\omega_{rd}, g(\omega_{rd}, \beta, V_w))$, since $V(\omega_{rd}, g(\omega_{rd}, \beta, V_w)) = 0$ and $V(\omega_r, \hat{g}) > 0$ for all $(\omega_r, \hat{g}) \neq (\omega_{rd}, g(\omega_{rd}, \beta, V_w))$ due to the property $\omega_r \ln \frac{\omega_r}{\omega_{rd}} - \omega_r + \omega_{rd} > 0$ for all $\omega_r \neq \omega_{rd}$. Furthermore, V is unbounded toward the top, bottom, and left boundary of the vertical strip D, but not so toward the right boundary of D. This is because for each fixed $\omega_r \in (0, \omega_r^{(1)}]$, $\lim_{|\hat{g}| \to \infty} V(\omega_r, \hat{g}) = \infty$, and for each fixed $\hat{g} \in \mathbb{R}$, $\lim_{\omega_r \to 0} V(\omega_r, \hat{g}) = \infty$ and $V(\omega_r^{(1)}, \hat{g}) < \infty$. Note that although V is not unbounded toward the right boundary of D, the state $(\omega_r, \hat{g})$ cannot cross this boundary due to (ii).

Differentiating V and using (3.27) and (3.28), we get

$$J\dot{V}=\begin{bmatrix}\alpha c\ln\frac{\omega_r}{\omega_{rd}}+(g-\hat{g})\frac{\partial g}{\partial\omega_r}\\ -(g-\hat{g})\end{bmatrix}^T\begin{bmatrix}g-\max\{\hat{g}+\alpha\ln\frac{\omega_r}{\omega_{rd}},0\}\\ h(g-\hat{g})\end{bmatrix},$$

where the function arguments are omitted. Note that because of (ii) and the above properties of V, to show (iii), it suffices to show that $\dot{V}$ is negative definite over D with respect to the equilibrium point $(\omega_{rd}, g(\omega_{rd}, \beta, V_w))$. To this end, let D be partitioned into two disjoint sets $D_1 = \{(\omega_r, \hat{g}) \in D : \hat{g} + \alpha \ln \frac{\omega_r}{\omega_{rd}} \geq 0\}$ and $D_2 = \{(\omega_r, \hat{g}) \in D : \hat{g} + \alpha \ln \frac{\omega_r}{\omega_{rd}} < 0\}$. Note that the equilibrium point $(\omega_{rd}, g(\omega_{rd}, \beta, V_w))$ is in D_1.

Suppose $(\omega_r, \hat{g}) \in D_1$. Then, $\dot{V}$ takes a quadratic form:

$$J\dot{V} = = -\begin{bmatrix}\ln\frac{\omega_r}{\omega_{rd}}\\ g-\hat{g}\end{bmatrix}^T\begin{bmatrix}\alpha^2 c & \frac{\alpha}{2}(\frac{\partial g}{\partial\omega_r}-c)\\ \frac{\alpha}{2}(\frac{\partial g}{\partial\omega_r}-c) & h-\frac{\partial g}{\partial\omega_r}\end{bmatrix}\begin{bmatrix}\ln\frac{\omega_r}{\omega_{rd}}\\ g-\hat{g}\end{bmatrix}.$$

Note that if $(\omega_r, \hat{g}) = (\omega_{rd}, g(\omega_{rd}, \beta, V_w))$, $\dot{V} = 0$. Also, the leading principal minors of the above symmetric matrix are $\alpha^2 c$ and $\alpha^2 c(h - \frac{1}{4c}(\frac{\partial g}{\partial\omega_r} + c)^2)$. Thus, if h and c satisfy

$$h - \frac{1}{4c}(\frac{\partial}{\partial\omega}g(\omega, \beta, V_w) + c)^2 > 0, \quad \forall\omega \in (0, \infty), \tag{3.30}$$

then this symmetric matrix is positive definite, so that $\dot{V} < 0$ for any $(\omega_r, \hat{g}) \neq (\omega_{rd}, g(\omega_{rd}, \beta, V_w))$. Therefore, if h and c satisfy (3.30), $\dot{V}$ is negative definite over D_1 with respect to $(\omega_{rd}, g(\omega_{rd}, \beta, V_w))$.

Next, suppose $(\omega_r, \hat{g}) \in D_2$. Then, $\dot{V}$ is bounded from above by a quadratic form:

$$\begin{aligned}J\dot{V} &= -h\hat{g}^2 + (2h - \frac{\partial g}{\partial\omega_r})g\hat{g} + (\frac{\partial g}{\partial\omega_r} - h)g^2 + \alpha c g \ln\frac{\omega_r}{\omega_{rd}}\\ &\leq -h\hat{g}^2 + (2h - \frac{\partial g}{\partial\omega_r})g\hat{g} + (\frac{\partial g}{\partial\omega_r} - h)g^2 - cg\hat{g}\\ &= -\begin{bmatrix}\hat{g}\\ g\end{bmatrix}^T\begin{bmatrix}h & \frac{1}{2}(\frac{\partial g}{\partial\omega_r}+c-2h)\\ \frac{1}{2}(\frac{\partial g}{\partial\omega_r}+c-2h) & h-\frac{\partial g}{\partial\omega_r}\end{bmatrix}\begin{bmatrix}\hat{g}\\ g\end{bmatrix}.\end{aligned}$$

Note that the leading principal minors of the above symmetric matrix are h and $c(h - \frac{1}{4c}(\frac{\partial g}{\partial \omega_r} + c)^2)$. Thus, if h and c satisfy (3.30), then this symmetric matrix is positive definite. Since $(\omega_r, \hat{g}) \in D_2$ and $\omega_{rd} \leq \omega_r^{(1)}$, if $\hat{g} = 0$, then $g > 0$. Thus, $\hat{g}$ and g cannot be zero simultaneously. Hence, $\dot{V} < 0$. Therefore, if h and c satisfy (3.30), $\dot{V}$ is negative over D_2.

As it follows from the above, if h and c satisfy (3.30), $\dot{V}$ is negative definite over D with respect to the equilibrium point $(\omega_{rd}, g(\omega_{rd}, \beta, V_w))$, so that (iii) holds.

It remains to show that if h satisfies (3.29), then there exists $c > 0$ such that (3.30) holds. Suppose h satisfies (3.29). Let $F(\underline{\gamma}, \overline{\gamma}) = \overline{\gamma}$ if $\overline{\gamma} \geq -\frac{1}{3}\underline{\gamma}$ and $F(\underline{\gamma}, \overline{\gamma}) = -\frac{(\overline{\gamma}-\underline{\gamma})^2}{8(\underline{\gamma}+\overline{\gamma})}$ otherwise. Then, $h > F(\underline{\gamma}, \overline{\gamma})$. Let $f(x, \underline{\gamma}, \overline{\gamma}) = \frac{1}{4x}\max\{(\underline{\gamma}+x)^2, (\overline{\gamma}+x)^2\}$, where $x > 0$. Then, it can be shown that $F(\underline{\gamma}, \overline{\gamma}) = \min_{x>0} f(x, \underline{\gamma}, \overline{\gamma})$ by considering the following three cases separately: $\overline{\gamma} \geq -\underline{\gamma}$, $-\underline{\gamma} > \overline{\gamma} \geq -\frac{1}{3}\underline{\gamma}$, and $-\frac{1}{3}\underline{\gamma} > \overline{\gamma}$. Because $h > F(\underline{\gamma}, \overline{\gamma})$, there exists $c > 0$, given by $c = \arg\min_{x>0} f(x, \underline{\gamma}, \overline{\gamma})$, such that $h > f(c, \underline{\gamma}, \overline{\gamma})$. Because $\underline{\gamma} \leq \frac{\partial}{\partial \omega} g(\omega, \beta, V_w) \leq \overline{\gamma}$ for all $\omega \in (0, \infty)$ and by definition of $f(x, \underline{\gamma}, \overline{\gamma})$, we have $\frac{1}{4c}(\frac{\partial}{\partial \omega} g(\omega, \beta, V_w) + c)^2 \leq f(c, \underline{\gamma}, \overline{\gamma})$ for all $\omega \in (0, \infty)$. Since $h > f(c, \underline{\gamma}, \overline{\gamma})$, (3.30) holds, as desired. □

Theorem 3.1 says that, by using the electromagnetic torque subcontroller with uncertainty estimation (3.24)–(3.26), if the gains α and h are positive and sufficiently large and if the desired reference ω_{rd} does not exceed $\omega_r^{(1)}$, then the rotor angular velocity ω_r asymptotically converges to ω_{rd} if ω_{rd}, β, and V_w are constants and closely tracks ω_{rd} if they are slow-varying. Notice that the gains α and h can be chosen independently of each other. Also, the condition "$\omega_{rd} \leq \omega_r^{(1)}$" is practically always satisfied, as $\omega_r^{(1)}$ is extremely large (see Figure 2.3).

Note that (3.24)–(3.26) describe the Electromagnetic Torque Subcontroller with Uncertainty Estimation block in Figure 3.1.

3.3.3 Polar Angle and Desired Rotor Angular Velocity Subcontroller

Up to this point in the chapter, we have yet to specify how θ, ω_{rd}, and β are determined. To do so, we first introduce a scalar performance measure and express this measure as a function of θ, ω_{rd}, and β. We then present a method for choosing these variables, which optimizes the measure.

Recall that the ultimate goal is to make the active and reactive powers P and Q closely track some desired references P_d and Q_d. Hence, it is useful to introduce a scalar performance measure, which characterizes how far P and Q are from P_d and Q_d. One such measure, denoted as U, is given by (2.60)

$$U = \frac{1}{2}\begin{bmatrix} P - P_d & Q - Q_d \end{bmatrix} \begin{bmatrix} w_p & w_{pq} \\ w_{pq} & w_q \end{bmatrix} \begin{bmatrix} P - P_d \\ Q - Q_d \end{bmatrix},$$

where w_p, w_q, and w_{pq} are design parameters satisfying $w_p > 0$ and $w_p w_q > w_{pq}^2$, so that $\left[\begin{smallmatrix} w_p & w_{pq} \\ w_{pq} & w_q \end{smallmatrix}\right]$ is a positive definite matrix. With these design parameters, one may specify how the differences $P - P_d$ and $Q - Q_d$ and their product $(P - P_d)(Q - Q_d)$ are penalized. Moreover, with U being a quadratic, positive definite function of $P - P_d$ and $Q - Q_d$, the smaller U is, the better the ultimate goal is achieved.

Having defined the performance measure U, we next establish the following statement: if the subcontrollers in Sections 3.3.1 and 3.3.2 are used with K chosen so that $A - BK$ has very fast eigenvalues, α chosen to be positive, and h chosen to satisfy (3.29), and if θ, ω_{rd}, β, V_w, P_d, and Q_d are all constants,

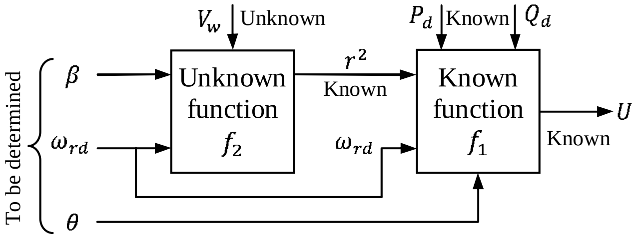

Figure 3.2: Relationships among the performance measure U, the to-be-determined variables θ, ω_{rd}, and β, and the exogenous variables V_w, P_d, and Q_d.

then after a short transient, U may be expressed as a known function f_1 of r^2, θ, ω_{rd}, P_d, and Q_d, while r^2, in turn, may be expressed as an unknown function f_2 of ω_{rd}, β, and V_w, i.e.,

$$U = f_1(r^2, \theta, \omega_{rd}, P_d, Q_d), \tag{3.31}$$

$$r^2 = f_2(\omega_{rd}, \beta, V_w), \tag{3.32}$$

as shown in Figure 3.2. To establish this statement, suppose the hypothesis is true. Then, after a short transient, it follows from (2.60) that U is a known function of P, Q, P_d, and Q_d; from (2.5)–(2.8), (2.17)–(2.22), (2.29), and (2.30) that P and Q are known functions of φ, ω_r, u_1, and u_2; from (2.32) that φ is a known function of u_1 and u_2; from (2.47) and (2.48) that u_1 and u_2 are known functions of r^2 and θ; and from Theorem 3.1 that $\omega_r = \omega_{rd}$. Thus, (3.31) holds with f_1 being known. On the other hand, it follows from (3.26) and Theorem 3.1 that $r^2 = g(\omega_{rd}, \beta, V_w)$. Hence, (3.32) holds with f_2 being unknown.

Equations (3.31) and (3.32), which are represented in Figure 3.2, suggest that U is a function of the to-be-determined variables θ, ω_{rd}, and β as well as the exogenous variables V_w, P_d, and Q_d. Given that the smaller U is the better, these to-be-determined variables may be chosen to minimize U.

However, such minimization is difficult to carry out because although P_d and Q_d are known, V_w is not. To make matter worse, since f_1 is known but f_2 is not, the objective function is not entirely known. Somewhat fortunately, as was shown in Figure 3.2, θ affects U only through f_1 and not f_2. Therefore, θ may be chosen to minimize U for any given r^2, ω_{rd}, P_d, and Q_d, i.e.,

$$\theta = \arg\min_{x \in [-\pi,\pi)} f_1(r^2, x, \omega_{rd}, P_d, Q_d), \tag{3.33}$$

which is implementable since r^2, ω_{rd}, P_d, and Q_d are all known. Alternatively, θ may be chosen as in (3.33) but with a low-pass filter inserted to reduce chattering, such as a moving-average filter, i.e.,

$$\theta(t) = \frac{1}{T_{ma}} \int_{t-T_{ma}}^{t} \arg\min_{x \in [-\pi,\pi)} f_1\big(r^2(\tau), x, \omega_{rd}(\tau), P_d(\tau), Q_d(\tau)\big) d\tau. \tag{3.34}$$

With θ chosen as in (3.34), the minimization problem reduces from a three-dimensional problem to a two-dimensional one, depending only on ω_{rd} and β. Since the objective function upon absorbing θ is unknown and since V_w may change quickly, instead of minimizing U with respect to both ω_{rd} and β—which may take a long time—we decide to sacrifice freedom for speed, minimizing U only with respect to ω_{rd} and updating β in a relatively slower fashion, which will be described in Section 3.3.4.

The minimization of U with respect to ω_{rd} is carried out based on a gradient-like approach as shown in Figure 3.3. To explain the rationale behind this approach, suppose β, V_w, P_d, and Q_d are constants. Then, according to (3.31)–(3.34), U is an unknown function of ω_{rd}. Because this function is not known, its gradient $\frac{\partial U}{\partial \omega_{rd}}$ at any ω_{rd} cannot be evaluated. To alleviate this issue, we evaluate U at two nearby ω_{rd}'s, use the two evaluated U's to obtain an estimate of the gradient $\frac{\partial U}{\partial \omega_{rd}}$, and move ω_{rd} along the direction where U

decreases, by an amount which depends on the gradient estimate. This idea is illustrated in Figure 3.3 and described precisely as follows: the desired rotor angular velocity $\omega_{rd}(t)$ is set to an initial value $\omega_{rd}(0)$ at time $t = 0$ and held constant until $t = T_1$, where T_1 should be sufficiently large so that both the electrical and mechanical dynamics have a chance to reach steady-state, but not too large which causes the minimization to be too slow. From time $t = T_1 - T_0$ to $t = T_1$, the average of $U(t)$, i.e., $\frac{1}{T_0}\int_{T_1-T_0}^{T_1} U(t)dt$, is recorded as the first value needed to obtain a gradient estimate. Similar to T_1, T_0 should be large enough so that small fluctuations in $U(t)$ (induced perhaps by a noisy V_w) are averaged out, but not too large which causes transient in the dynamics to be included. The variable $\omega_{rd}(t)$ is then changed gradually in an S-shape manner from $\omega_{rd}(0)$ at time $t = T_1$ to a nearby $\omega_{rd}(0) + \Delta\omega_{rd}(T_1)$ at $t = T_1 + T_2$, where $\Delta\omega_{rd}(T_1)$ is an initial stepsize, and T_2 should be sufficiently large but not overly so, so that the transition in $\omega_{rd}(t)$ is smooth and yet not too slow. The variable $\omega_{rd}(t)$ is then held constant until $t = 2T_1 + T_2$, and the average of $U(t)$ from $t = 2T_1 + T_2 - T_0$ to $t = 2T_1 + T_2$, i.e., $\frac{1}{T_0}\int_{2T_1+T_2-T_0}^{2T_1+T_2} U(t)dt$, is recorded as the second value needed to obtain the gradient estimate. At time $t = 2T_1 + T_2$, the two recorded values are used to form the gradient estimate, which is in turn used to decide a new stepsize $\Delta\omega_{rd}(2T_1 + T_2)$ through

$$\Delta\omega_{rd}(2T_1 + T_2) = -\epsilon_1 \operatorname{sat}\left(\frac{\frac{1}{T_0}\int_{2T_1+T_2-T_0}^{2T_1+T_2} U(t)dt - \frac{1}{T_0}\int_{T_1-T_0}^{T_1} U(t)dt}{\epsilon_2\Delta\omega_{rd}(T_1)}\right), \quad (3.35)$$

where $\epsilon_1 > 0$ and $\epsilon_2 > 0$ are design parameters that define the new stepsize $\Delta\omega_{rd}(2T_1 + T_2)$, and sat() denotes the standard saturation function that limits $\Delta\omega_{rd}(2T_1 + T_2)$ to $\pm\epsilon_1$. Upon deciding $\Delta\omega_{rd}(2T_1 + T_2)$, $\omega_{rd}(t)$ is again changed in an S-shape manner from $\omega_{rd}(0) + \Delta\omega_{rd}(T_1)$ at $t = 2T_1 + T_2$ to $\omega_{rd}(0) + \Delta\omega_{rd}(T_1) + \Delta\omega_{rd}(2T_1 + T_2)$ at $t = 2T_1 + 2T_2$, in a way similar to the time

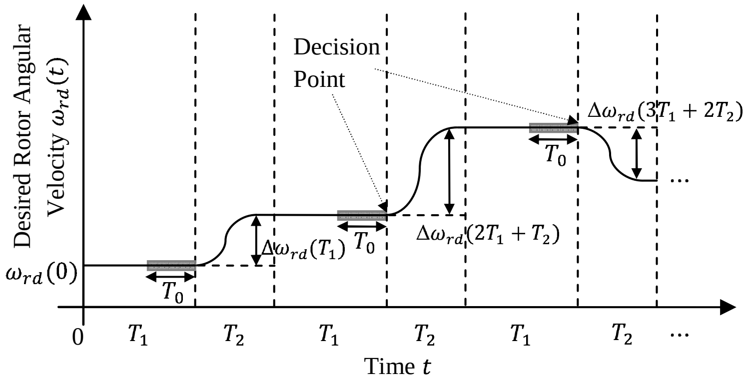

Figure 3.3: A graphical illustration of the gradient-like approach.

interval $[T_1, T_1+T_2]$. The process then repeats with the second recorded value from the previous cycle $[0, 2T_1+T_2]$ becoming the first recorded value for the next cycle $[T_1+T_2, 3T_1+2T_2]$, and so on. Therefore, with this gradient-like approach, ω_{rd} is guaranteed to approach a local minimum when β, V_w, P_d, and Q_d are constants, and track a local minimum when they are slow-varying.

Note that (2.60), (3.34), and (3.35) describe the Polar Angle and Desired Rotor Angular Velocity Subcontroller block in Figure 3.1.

3.3.4 Blade Pitch Angle Subcontroller

As was mentioned, to speed up the minimization, we have decided to minimize U only with respect to ω_{rd}, leaving the blade pitch angle β as the remaining undetermined variable. Given that an active power P that is larger than the rated value P_{rated} of the turbine may cause damage, we decide to use β to prevent P from exceeding P_{rated}. Specifically, we let β be updated according to

$$\dot{\beta} = \begin{cases} 0 & \text{if } \beta = \beta_{\min} \text{ and } P < P_{\text{rated}}, \\ 0 & \text{if } \beta = \beta_{\max} \text{ and } P > P_{\text{rated}}, \\ -\epsilon_3(P_{\text{rated}} - P) & \text{otherwise,} \end{cases} \tag{3.36}$$

where $\epsilon_3 > 0$ is a design parameter that dictates the rate at which β changes. Note that with (3.36), β is guaranteed to lie between β_{min} and β_{max}. Moreover, when P is above (below) P_{rated}, β increases (decreases) if possible, in order to try to capture less (more) wind power, which leads to a smaller (larger) P.

Note that (3.36) describes the Blade Pitch Angle Subcontroller block in Figure 3.1.

3.4 Simulation Results

To demonstrate the capability and effectiveness of the proposed controller, simulation has been carried out in MATLAB. To describe the simulation settings and results, both the per-unit and physical unit systems will be used interchangeably.

As for the proposed controller, we choose its parameters as follows: for the Rotor Voltages Subcontroller, we let the desired closed-loop eigenvalues of the electrical dynamics be at -5, $-10 \pm 5j$, and -15. Using MATLAB's `place()` function, the state feedback gain matrix K that yields these eigenvalues is

$$K = \begin{bmatrix} 5135.9 & 259.2 & 20.3 & 1.9 \\ -2676.7 & 4289.9 & -1.3 & 19.7 \end{bmatrix}.$$

Moreover, we let $\alpha = 5$ and $h = 17.5$ for the Electromagnetic Torque Subcontroller with Uncertainty Estimation; let $w_p = 10$, $w_q = 1$, $w_{pq} = 0$, $\epsilon_1 = 0.025$, $\epsilon_2 = 2$, $T_0 = 1\,\text{s}$, $T_1 = 4\,\text{s}$, and $T_2 = 6\,\text{s}$ and use (3.34) with $T_{ma} = 0.75\,\text{s}$ for the Polar Angle and Desired Rotor Angular Velocity Subcontroller; and let $\epsilon_3 = 3$ and $P_{\text{rated}} = 1\,\text{pu}$ for the Blade Pitch Angle Subcontroller.

The simulation results are as follows: we consider a scenario where the wind speed V_w is derived from actual wind profiles from a wind farm located

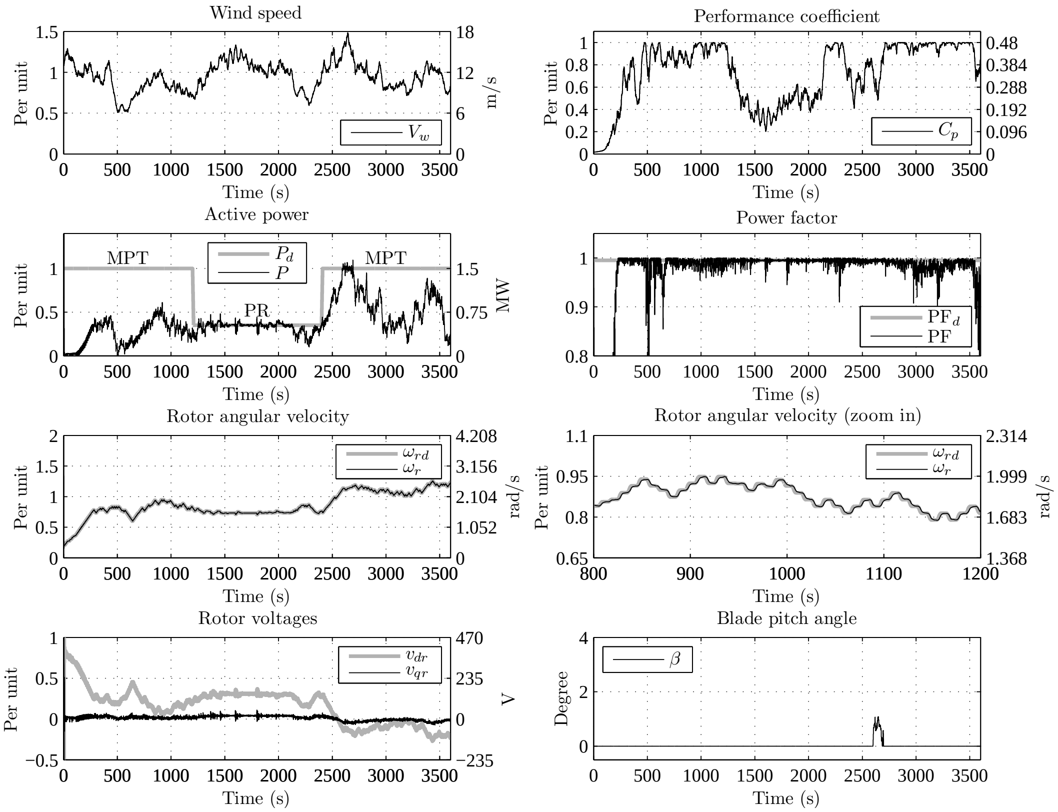

Figure 3.4: Effective operation in both the MPT and PR modes and seamless switching between them under an actual wind profile from a wind farm located in northwest Oklahoma.

in northwest Oklahoma, the desired active power P_d experiences large step changes, and the desired reactive power Q_d is such that the desired power factor PF$_d$ is fixed at 0.995. As will be explained below, the values of P_d force the turbine to operate in both the MPT and PR modes, along with switching between them, under realistic wind profiles. Figures 3.4 and 3.5 show the simulation results for this scenario in both the per-unit and physical unit systems. Note that in Figure 3.4, for the first 1200 seconds during which P_d is unachievable at 1 pu, the turbine operates in the MPT mode and maximizes P, as indicated by the value of C_p approaching its maximum of 0.48 after a short transient (the turbine is initially at rest). At time 1200s when P_d

drops sharply from 1 pu to an achievable value of 0.35 pu, the turbine quickly reduces the value of C_p, accurately regulates P around P_d, and effectively rejects the “disturbance” V_w, thereby smoothly switches from the MPT mode to the PR mode. At time 2400s when P_d goes from 0.35 pu back to 1 pu, the MPT mode resumes. Because V_w is strong enough at that time, P approaches P_d. Moreover, the moment P exceeds P_d (which is equal to P_{rated}), the blade pitch angle β increases in order to clip the power and protect the turbine. At time 2700s when V_w becomes weaker, β returns to $\beta_{\min} = 0\,\text{deg}$, thereby allowing the value of C_p to return to its maximum of 0.48 and P to be maximized. As can be seen from the figure, throughout the simulation, PF is maintained near PF_d, affected only slightly and relatively shortly by the random wind fluctuations. Moreover, the angular velocity ω_r tracks the desired time-varying reference ω_{rd} closely. As expected, the small S-shape variations in ω_{rd} resemble those in Figure 3.3. Notice that similar observations can be made in Figure 3.5, which shows additional simulation results with a different wind profile and different desired active and reactive powers.

The above simulation results suggest that the proposed controller not only is capable of operating effectively in both the MPT and PR modes, it is also capable of switching smoothly between them—all while not knowing the C_p-surface, air density, friction coefficient, and wind speed.

3.5 Conclusion

In this chapter, we have designed a controller for a variable-speed wind turbine with a DFIG. The controller has been developed based on a fifth-order, electromechanically-coupled, nonlinear model of the wind turbine by

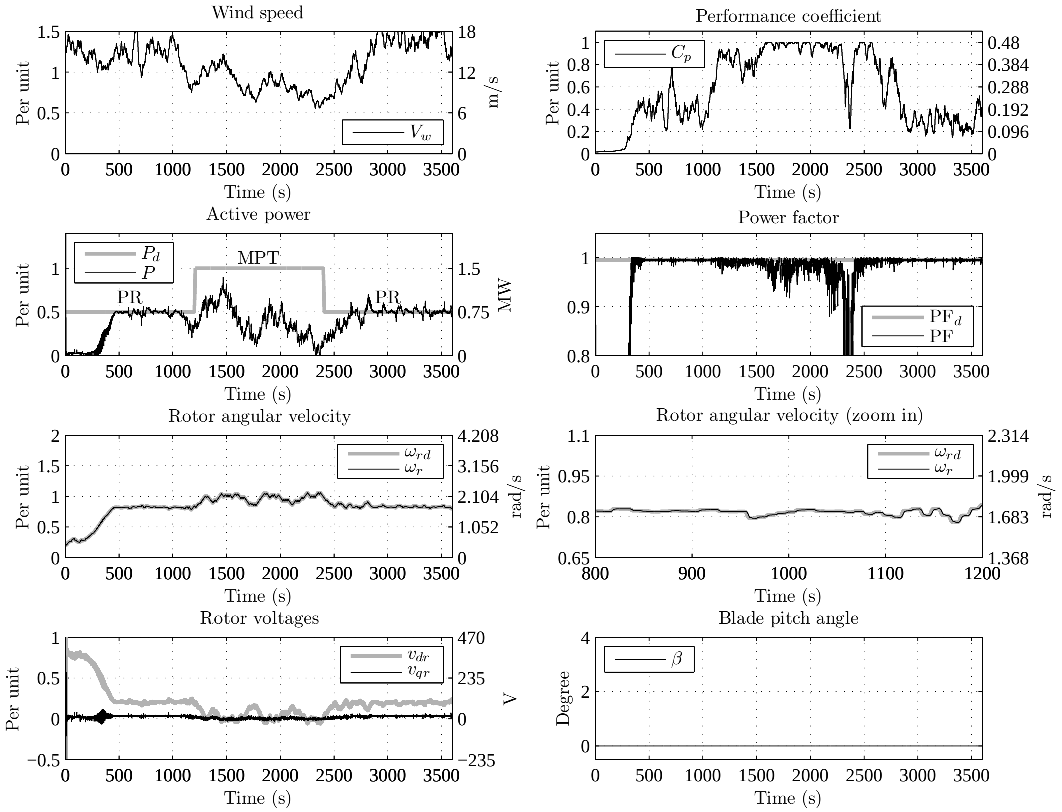

Figure 3.5: Operation with a different wind profile and different desired active and reactive powers.

integrating several control strategies and exploiting time-scale separation in the dynamics. We have shown that the controller is able to make the wind turbine operate in both the MPT and PR modes and switch smoothly between them, while maintaining a desired power factor. Furthermore, the controller does not require knowledge of the C_p-surface, air density, friction coefficient, and wind speed. Simulation has been carried out using realistic wind profiles, and the results demonstrate the capability and effectiveness of the controller.

Chapter 4 An Approximate Wind Turbine Control System Model for Wind Farm Power Control

4.1 Introduction

In this chapter, we propose a mathematical wind turbine control system (WTCS) model that is aimed at a nifty design and deep analysis and understanding of a supervisory wind farm controller. To this end, suppose we have developed, or are given, a WTCS—call it WTCS*—and wish to design a WFC. Also suppose, at our disposal, is a mathematical model parameterized by a vector θ—call it WTCS$^\theta$—which, like WTCS* (or each WTCS in Figure 1.1), maps inputs (P_d, Q_d, V_w) to outputs (P, Q), i.e., $(P, Q) = \text{WTCS}^\theta(P_d, Q_d, V_w)$. Consider the following conditions on the model WTCS$^\theta$:

(C1) There exists a θ such that whenever WTCS$^\theta$ and WTCS* are driven by the same inputs (P_d, Q_d, V_w), they produce approximately the same outputs (P, Q).

(C2) WTCS$^\theta$ may be a nonlinear dynamical system but has a favorable structure conducive to control systems analysis and design.

(C3) There is a set of WTCSs in the literature such that for each WTCS in the set, there exists a θ such that whenever WTCS$^\theta$ and the WTCS are driven by the same inputs (P_d, Q_d, V_w), they produce approximately the same outputs (P, Q).

Note that if (C1) holds, WTCS^{θ}—with the specific value of θ—would be an accurate approximation of WTCS^{*} and, thus, may be used in place of WTCS^{*} in the WFC design and WFCS analysis. If, in addition, (C2) holds, the design and analysis would be more likely to succeed due to the favorable structure of WTCS^{θ}. If (C3) holds as well, WTCS^{θ}—with different values of θ—would be able to also approximate a number of different WTCSs in the literature (or by different manufacturers), making it a versatile model that brings WTCS^{*} and those WTCSs under the same umbrella, distinguished only by θ. It follows that the design and analysis outcomes (e.g., new control techniques, stability criteria, and performance formulas) are applicable not only to WTCS^{*}, but perhaps also to those WTCSs, increasing their impact. Hence, having an approximate model WTCS^{θ} that satisfies conditions (C1)–(C3) is extremely valuable.

This chapter is devoted to the development of such a model. We first assume, in Section 4.2, that two generic models of WTCS^{*} are given, namely, an *analytical model* described by a set of continuous-time nonlinear differential equations, and an *empirical model* described by a set of input-output measurement data. The latter is motivated by the fact that in practice, what is available may just be a set of data, rather than a mathematical model, due to legacy and proprietary reasons. Based on standard system identification approaches [70] and typical WTCS characteristics, we then develop, in Section 4.3, an *approximate model* WTCS^{θ}, which attempts to imitate both the analytical and empirical models. For each of these two models, we also provide a parameter identification scheme that sequentially determines the θ required in (C1), which is a vector of 10 parameters (two functions and eight scalars). The approximate model, depicted in Figure 4.2(c), may be regarded as satisfying (C2) because it is made up of two structurally identical parts—one for active power and the other for reactive—each of which is a third-order system that would have been linear if not for a static nonlinear component at its inputs (i.e., a modified Hammerstein model [70, 71]). Next, we validate, in Section 4.4, the approximate model via simulation, showing that it has enough ingredients to closely imitate several different analytical and empirical models from the literature [1–4] and from real data taken from an Oklahoma wind farm. The encouraging results suggest that the approximate model satisfies (C3) and, hence, may be used to facilitate the design and analysis of a second-to-minute-timescale supervisory WFC that yields a sophisticated WFCS. Finally, Section 4.5 concludes the chapter.

4.2 Models of Wind Turbine Control Systems

In this section, we describe a generic analytical model and a generic empirical model of a WTCS. These two models set the stage for the development of an approximate model that mimics the dynamic performance of the WTCS, when it provides primary generation services to the grid.

4.2.1 Analytical Model

To control a variable-speed wind turbine, a standard approach is to first model its dynamics based on first principles, and then design a controller based on known techniques. Regardless of the model and design, the resulting WTCS typically can be represented in a block diagram form as in Figure 4.1, and described generically by a set of continuous-time, nonlinear differential

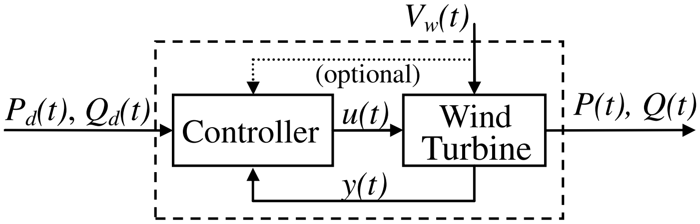

Figure 4.1: Block diagram of a wind turbine control system.

equations in state-space form as follows:

$$\dot{x}(t) = f(x(t), P_d(t), Q_d(t), V_w(t)),\ x(0) = x_0, \tag{4.1}$$

$$(P(t), Q(t)) = g(x(t), P_d(t), Q_d(t), V_w(t)). \tag{4.2}$$

Here, $t \geq 0$ denotes time; $x(t) \in \mathbb{R}^n$ is the system states combining the wind turbine states (e.g., stator and rotor fluxes or currents, rotor angular velocity) and controller states (if any); $x(0)$ is the initial states; f and g are functions depending on the particular wind turbine model (e.g., fourth-order [63] or second-order [64] doubly fed induction generator (DFIG) dynamics or second-order permanent magnet synchronous generator (PMSG) dynamics [72], and rigid-shaft or flexible-shaft [64] mechanical dynamics) and the particular controller design (e.g., one of the designs in [1, 3, 5, 51, 52, 73–77]) including their parameters (e.g., resistances, inductances, rotor moment of inertia, rotor swept area, C_p-surface, air density, friction coefficient, controller gains); $P_d(t)$, $Q_d(t)$, $P(t)$, and $Q(t)$ are, respectively, the system inputs and outputs representing the desired and actual active and reactive powers, where positive values mean toward the grid; $V_w(t)$ is another system input representing the wind speed; $u(t)$ is the internal control signals (e.g., rotor voltages, blade pitch angle, electromagnetic torque); and $y(t)$ is the internal feedback signals (e.g., various voltages and currents, rotor angular velocity, actual powers).

In this chapter, we assume that a generic *analytical model* of a WTCS, in the form of (4.1) and (4.2), is given as the first of two models considered. In order to represent as many WTCSs in the literature as possible, we make only two assumptions about the analytical model (4.1) and (4.2): first, the inputs $(P_d(t), Q_d(t), V_w(t))$ are always in an *operating region* $\mathcal{S} \triangleq [0, P_{d,\text{MAX}}] \times [-Q_{d,\text{MAX}}, Q_{d,\text{MAX}}] \times [0, V_{w,\text{MAX}}]$. Second, the WTCS is reasonably well-designed, i.e., the functions f and g are such that for each constant $(P_d(t), Q_d(t), V_w(t)) = (\bar{P}_d, \bar{Q}_d, \bar{V}_w) \in \mathcal{S}$, there exist steady-state values (P_{ss}, Q_{ss}), depending possibly on $(\bar{P}_d, \bar{Q}_d, \bar{V}_w)$, such that for every $x(0)$, $\lim_{t\to\infty}(P(t), Q(t)) = (P_{ss}, Q_{ss})$. Finally, we allow $Q_d(t)$ and $Q(t)$ to be absent, since many existing WTCSs do not consider the reactive power (e.g., [74–76]), and $P_d(t)$ to be absent as well, since some existing WTCSs do not require it to be specified (e.g., [4, 15, 21, 78, 79]). However, we require $P(t)$ and $V_w(t)$ to be present, since they are essential to WTCSs.

4.2.2 Empirical Model

Although it is common to work with a mathematical model in research on WTCSs, in practice we may not have access to the inner working of a WTCS, due perhaps to legacy and proprietary reasons. Instead, what may be available to us is a set of input-output measurement data, so that we have no choice but to treat the WTCS as a “black box.” The set of data can take various forms, but more often than not includes the following information:

Inputs			Outputs	
$P_d(0)$	$Q_d(0)$	$V_w(0)$	$P(0)$	$Q(0)$
$P_d(\Delta)$	$Q_d(\Delta)$	$V_w(\Delta)$	$P(\Delta)$	$Q(\Delta)$
$\vdots$	$\vdots$	$\vdots$	$\vdots$	$\vdots$
$P_d((D-1)\Delta)$	$Q_d((D-1)\Delta)$	$V_w((D-1)\Delta)$	$P((D-1)\Delta)$	$Q((D-1)\Delta)$

(4.3)

where $\Delta > 0$ is the sampling period which is usually on the order of seconds or minutes, and D is the number of data points which is usually large.

In this chapter, we assume that a generic *empirical model* of a WTCS, in the form of (4.3), is given as the second of the two models considered. Similar to the analytical model (4.1) and (4.2), in the empirical model (4.3) the columns $P_d(i\Delta)$, $Q_d(i\Delta)$, and $Q(i\Delta)$ are optional but the columns $V_w(i\Delta)$ and $P(i\Delta)$ are mandatory. However, unlike the analytical one where the inputs $(P_d(t), Q_d(t), V_w(t))$ can be arbitrarily specified, with this empirical model we have no control over the inputs $(P_d(i\Delta), Q_d(i\Delta), V_w(i\Delta))$, as they are simply given, in the first three columns. This difference will be accounted for shortly.

Remark 4.1. The two models of WTCSs in this section may be thought of as the WTCS* in Section 4.1.

4.2.3 Discussion

The analytical model (4.1) and (4.2) and the empirical model (4.3) are what our approximate model intends to imitate. As will be described in Section 4.3, our approach is based on postulating a static nonlinear model that matches the steady-state input-output characteristics, followed by enriching the model with linear dynamics so that it also matches the transient input-output behaviors. A benefit of this input-output approach is that it bypasses the need to consider the internal dynamics and specific details of the underlying WTCS, thereby allowing major types of generation technologies such as DFIG, PMSG, and IG to be approximately described using a simple, consistent model. More important, such a model enables one to approximately describe a large number of same or different types of WTCSs within a wind farm in a unified fashion, so that researchers may focus on other pressing issues when designing a comprehensive WFCS and understanding its attainable performance.

4.3 Proposed Approximate Model

In this section, we develop a simple mathematical model that approximates the analytical and empirical WTCS models in Section 4.2, and a parameter identification scheme that determines the model parameters in each case. The development consists of three steps in both cases, as described below.

4.3.1 Approximating the Analytical Model

Step 1: Mimicking the steady-state responses to constant inputs

In general, to create a system that mimics another system, it is reasonable to demand that the two systems exhibit the same steady-state responses to constant inputs. With this in mind, we note that whenever the analytical model (4.1) and (4.2) is subject to constant inputs $(P_d(t), Q_d(t), V_w(t)) = (\bar{P}_d, \bar{Q}_d, \bar{V}_w)$, its outputs $(P(t), Q(t))$ asymptotically converge to some steady-state values (P_{ss}, Q_{ss}), which depend only on $(\bar{P}_d, \bar{Q}_d, \bar{V}_w)$ and not on the initial states $x(0)$. This dependency suggests that there exist functions $\varphi_1 : \mathcal{S} \to \mathbb{R}$ and $\varphi_2 : \mathcal{S} \to \mathbb{R}$, such that $P_{ss} = \varphi_1(\bar{P}_d, \bar{Q}_d, \bar{V}_w)$ and $Q_{ss} = \varphi_2(\bar{P}_d, \bar{Q}_d, \bar{V}_w)$. It also suggests a static nonlinear model of the form

$$P(t) = \varphi_1(P_d(t), Q_d(t), V_w(t)), \tag{4.4}$$

$$Q(t) = \varphi_2(P_d(t), Q_d(t), V_w(t)), \tag{4.5}$$

which is capable of mimicking—at the very least—the steady-state outputs of the analytical model (4.1) and (4.2) whenever the inputs are constant, or slow-varying. To visually connect this Step 1 with subsequent steps of the

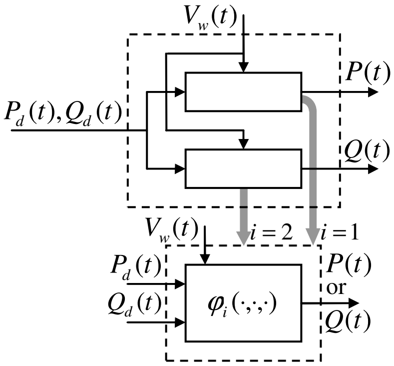

(a) Block diagram after Step 1 of 3.

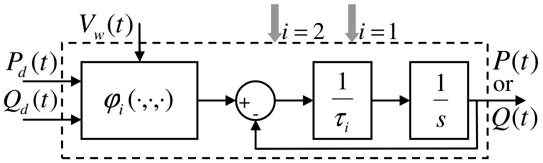

(b) Block diagram after Step 2 of 3.

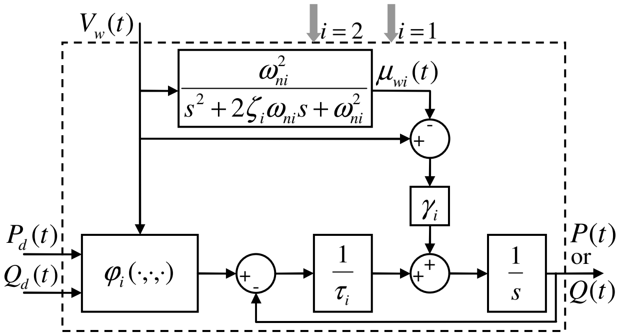

(c) Block diagram after Step 3 of 3.

Figure 4.2: Step-by-step development of the proposed approximate model.

development, a block diagram of the model (4.4) and (4.5) is shown in Figure 4.2(a).

Remark 4.2. Throughout the chapter, the subscripts 1 and 2 are used to distinguish between similar parameters or variables associated with the *active* and *reactive* powers (e.g., φ_1 is for active and φ_2 is for reactive in Figure 4.2(a)).

The functions φ_1 and φ_2 are (infinite-dimensional) parameters of the model (4.4) and (4.5), which can be identified by simulating the analytical model (4.1) and (4.2) with various constant inputs sufficiently covering the operating region $\mathcal{S}$, observing the steady-state outputs, and employing interpolation. The following procedure provides the details:

Procedure for Step 1

```
Pick a large $N_1 \in \mathbb{N} = \{1, 2, \dots\}$.
Pick $(P_d^{(i)}, Q_d^{(i)}, V_w^{(i)}) \in \mathcal{S}$ for $i = 1, 2, \dots, N_1$.
Pick a large $T > 0$.
Loop over $i = 1, 2, \dots, N_1$.
    Let $(P_d(t), Q_d(t), V_w(t)) = (P_d^{(i)}, Q_d^{(i)}, V_w^{(i)}) \, \forall \, t \in [0, \, T]$.
    Pick any $x(0)$.
    Simulate the analytical model (4.1) and (4.2) from $t = 0$ to $t = T$.
    Record $(P(T), Q(T))$.
    Let $\varphi_1(P_d^{(i)}, Q_d^{(i)}, V_w^{(i)}) = P(T)$ and $\varphi_2(P_d^{(i)}, Q_d^{(i)}, V_w^{(i)}) = Q(T)$.
End loop.
Determine $\varphi_1$ and $\varphi_2$ via interpolation on the $N_1$ data points obtained.
```

Applying the above procedure to identify the functions φ_1 and φ_2, we obtain a basic model (4.4) and (4.5) that exhibits the same steady-state behavior as that of (4.1) and (4.2).

Step 2: Mimicking the transient responses to staircase inputs

The basic model (4.4) and (4.5) in Figure 4.2(a) is able to match the steady-state response of the analytical model (4.1) and (4.2). However, it fails to produce any kind of transient one would expect with WTCSs because (4.4) and (4.5) are merely static functions mapping the inputs $(P_d(t), Q_d(t), V_w(t))$ to the outputs $(P(t), Q(t))$. To alleviate this drawback, we insert into Figure 4.2(a) first-order linear dynamics between $\varphi_1(\cdot)$ and $P(t)$ and between $\varphi_2(\cdot)$ and $Q(t)$, to arrive at a Hammerstein model (see [71] and Chapter 5.2 of [70]) shown in Figure 4.2(b) and given by

$$\dot{P}(t) = -\tfrac{1}{\tau_1}P(t) + \tfrac{1}{\tau_1}\varphi_1(P_d(t), Q_d(t), V_w(t)), \tag{4.6}$$

$$\dot{Q}(t) = -\tfrac{1}{\tau_2}Q(t) + \tfrac{1}{\tau_2}\varphi_2(P_d(t), Q_d(t), V_w(t)), \tag{4.7}$$

where $\tau_1 > 0$ and $\tau_2 > 0$ are the time constants. Note that in steady-state, (4.6) and (4.7) reduce to (4.4) and (4.5). Hence, (4.6) and (4.7) are able to capture not only the steady-state behavior of the analytical model (4.1) and (4.2), but also the dominant mode of its transient behavior with proper choices of τ_1 and τ_2.

The time constants τ_1 and τ_2 can be identified using a general approach in system identification sometimes known as the prediction-error methods (see Chapter 7 of [70]). With this approach, we first choose specific inputs and use them to simulate the analytical model (4.1) and (4.2) and the model (4.6) and (4.7), the latter with different values of τ_1 and τ_2. We then compare the outputs of the two models and determine the best τ_1 and τ_2, which minimize the output differences. The following procedure details this approach, in which we choose the inputs to be random staircase signals because they tend to bring out the dominant mode in systems, and allow any $\mathcal{L}_p$ norm to be used for measuring the output differences:

Procedure for Step 2

---

1) Pick a large $N_2 \in \mathbb{N}$.
2) Pick $(P_d^{(i)}, Q_d^{(i)}, V_w^{(i)}) \in \mathcal{S}$ for $i = 1, 2, \ldots, N_2$ randomly, independently, and equiprobably.
3) Use the T in Step 1.

```
4) Let $(P_d(t), Q_d(t), V_w(t))=(P_d^{(i)}, Q_d^{(i)}, V_w^{(i)})\ \forall\, t\in[(i-1)T,\ iT)$ for $i=1,2,\ldots,N_2$.
5) Pick any $x(0)$.
6) Simulate the analytical model (4.1) and (4.2) from $t = 0$ to $t = N_2T$.
7) Record $(P(t), Q(t))\ \forall\, t \in [0,\ N_2T]$ as $(P_{an}(t), Q_{an}(t))$.
8) Pick a large $N_3 \in \mathbb{N}$.
9) Pick $\tau_1^{(i)} > 0$ and $\tau_2^{(i)} > 0$ for $i = 1, 2, \ldots, N_3$.
10) Use the $\varphi_1$ and $\varphi_2$ identified in Step 1.
11) Pick any $(P(0), Q(0))$.
12) Loop over $i = 1, 2, \ldots, N_3$.
13) Let $\tau_1 = \tau_1^{(i)}$ and $\tau_2 = \tau_2^{(i)}$.
14) Simulate the model (4.6) and (4.7) from $t = 0$ to $t = N_2T$.
15) Record $(P(t), Q(t))\ \forall\, t \in [0,\ N_2T]$ as $(P_{ap}^{(i)}(t), Q_{ap}^{(i)}(t))$.
16) Calculate
        $J_1(\tau_1^{(i)}) = (\int_{T_1}^{N_2T} |P_{an}(t) - P_{ap}^{(i)}(t)|^{p_1} dt)^{\frac{1}{p_1}},$
        $J_2(\tau_2^{(i)}) = (\int_{T_2}^{N_2T} |Q_{an}(t) - Q_{ap}^{(i)}(t)|^{p_2} dt)^{\frac{1}{p_2}},$
    where $T_1 \in (0,\ N_2T)$, $T_2 \in (0,\ N_2T)$, $p_1 \geq 1$, and $p_2 \geq 1$.
17) End loop.
18) Let $\tau_1 = \underset{\tau\in\{\tau_1^{(1)},\ldots,\tau_1^{(N_3)}\}}{\arg\min} J_1(\tau)$ and $\tau_2 = \underset{\tau\in\{\tau_2^{(1)},\ldots,\tau_2^{(N_3)}\}}{\arg\min} J_2(\tau)$.
```

Remark 4.3. In the above procedure, $\tau_1^{(i)}$ and $\tau_2^{(i)}$ for $i = 1, 2, \ldots, N_3$ represent the search space for the best τ_1 and τ_2; p_1 and p_2 represent the desired $\mathcal{L}_p$ norms; and T_1 and T_2 are introduced to reduce the impact of the initial states (i.e., $x(0)$ of the analytical model (4.1) and (4.2) and $(P(0), Q(0))$ of the model (4.6) and (4.7)) on the parameter estimation process.

Using the preceding procedure to identify the time constants τ_1 and τ_2, we obtain a refined model (4.6) and (4.7) that has more flexibility to better match the behavior of (4.1) and (4.2).

Step 3: Mimicking the responses to realistic inputs

Although the refined model (4.6) and (4.7) in Figure 4.2(b) is more sophisticated than the basic model (4.4) and (4.5) in Figure 4.2(a), it can only produce first-order-like responses. If such responses are indeed what the analytical model (4.1) and (4.2) produces, or if what we desire is just a crude approximation, then the refined model (4.6) and (4.7) may be satisfactory. Otherwise, its accuracy may be unacceptable.

At first glance, this issue can be overcome by replacing the first-order linear dynamics in (4.6) and (4.7) with higher-order ones. This approach, however, has a fundamental limitation: recall from Step 1 that $P_{ss} = \varphi_1(\bar{P}_d, \bar{Q}_d, \bar{V}_w)$ and $Q_{ss} = \varphi_2(\bar{P}_d, \bar{Q}_d, \bar{V}_w)$. Thus, if a WTCS does power regulation and does it well over a wide range of $\bar{V}_w$, then $P_{ss} \approx \bar{P}_d$ and $Q_{ss} \approx \bar{Q}_d$ for any $\bar{V}_w$ in that range. As a result, $\varphi_1(P_d(t), Q_d(t), V_w(t))$ in (4.6) and $\varphi_2(P_d(t), Q_d(t), V_w(t))$ in (4.7) would both be insensitive to $V_w(t)$, so that even large fluctuations in the wind speed $V_w(t)$ would be completely absorbed by $\varphi_1(\cdot)$ and $\varphi_2(\cdot)$, producing no fluctuations in the active and reactive powers $P(t)$ and $Q(t)$, which may be unrealistic.

To bypass this limitation, we introduce two second-order linear filters and add two linear terms to (4.6) and (4.7), to get a modified Hammerstein model depicted in Figure 4.2(c) and defined by

$$\begin{bmatrix} \dot{\mu}_{w1}(t) \\ \ddot{\mu}_{w1}(t) \end{bmatrix} = \begin{bmatrix} 0 & 1 \\ -\omega_{n1}^2 & -2\zeta_1\omega_{n1} \end{bmatrix} \begin{bmatrix} \mu_{w1}(t) \\ \dot{\mu}_{w1}(t) \end{bmatrix} + \begin{bmatrix} 0 \\ \omega_{n1}^2 \end{bmatrix} V_w(t), \tag{4.8}$$

$$\begin{bmatrix}\dot{\mu}_{w2}(t)\\ \ddot{\mu}_{w2}(t)\end{bmatrix}=\begin{bmatrix}0 & 1\\ -\omega_{n2}^2 & -2\zeta_2\omega_{n2}\end{bmatrix}\begin{bmatrix}\mu_{w2}(t)\\ \dot{\mu}_{w2}(t)\end{bmatrix}+\begin{bmatrix}0\\ \omega_{n2}^2\end{bmatrix}V_w(t), \tag{4.9}$$

$$\dot{P}(t)=-\tfrac{1}{\tau_1}P(t)+\tfrac{1}{\tau_1}\varphi_1(P_d(t),Q_d(t),V_w(t))+\gamma_1(V_w(t)-\mu_{w1}(t)), \tag{4.10}$$

$$\dot{Q}(t)=-\tfrac{1}{\tau_2}Q(t)+\tfrac{1}{\tau_2}\varphi_2(P_d(t),Q_d(t),V_w(t))+\gamma_2(V_w(t)-\mu_{w2}(t)), \tag{4.11}$$

where $\mu_{w1}(t)$ and $\mu_{w2}(t)$ are the filter outputs, $\zeta_1 > 0$ and $\zeta_2 > 0$ are the damping ratios, $\omega_{n1} > 0$ and $\omega_{n2} > 0$ are the natural frequencies, and $\gamma_1 \geq 0$ and $\gamma_2 \geq 0$ are scalar gains. To see the rationale behind (4.8)–(4.11), notice that the second-order linear filters in (4.8) and (4.9) are low-pass filters with unity DC gains. Hence, $\mu_{w1}(t)$ and $\mu_{w2}(t)$ may be seen as short-term averages of $V_w(t)$, which catch up to $V_w(t)$ if it ever approaches constant, and $V_w(t) - \mu_{w1}(t)$ and $V_w(t) - \mu_{w2}(t)$ may be viewed as deviations of $V_w(t)$ from its short-term averages, which fluctuate around zero. It follows that the linear terms $\gamma_1(V_w(t) - \mu_{w1}(t))$ and $\gamma_2(V_w(t) - \mu_{w2}(t))$ in (4.10) and (4.11) enable fluctuations in $V_w(t)$ to induce fluctuations in $P(t)$ and $Q(t)$, bypassing the aforementioned limitation and yielding a feature not possessed by the refined model (4.6) and (4.7). Moreover, because the steady-state values of these terms are zero when $V_w(t)$ is constant, (4.10) and (4.11) also preserve the role of φ_1 and φ_2 as constant-inputs-to-steady-state-outputs maps (see Step 1). Finally, due to the "tuning knobs" ζ_1, ω_{n1}, γ_1, ζ_2, ω_{n2}, and γ_2, (4.8)–(4.11) possess considerable (but not excessive) freedom to mimic the way fluctuations in $V_w(t)$ affect $P(t)$ and $Q(t)$ of the analytical model (4.1) and (4.2). All of these explain the rationale behind (4.8)–(4.11), which we will refer to from now on as the *approximate model.*

The parameters ζ_1, ω_{n1}, γ_1, ζ_2, ω_{n2}, and γ_2 can be identified using the general approach adopted in Step 2, i.e., the so-called prediction-error methods [70]. Indeed, a procedure analogous to the one in Step 2 may be constructed as follows:

```
Procedure for Step 3
1) Pick a large $T > 0$.
2) Pick some specific $(P_d(t), Q_d(t), V_w(t)) \, \forall \, t \in [0,\, T]$.
3) Pick any $x(0)$.
4) Simulate the analytical model (4.1) and (4.2) from $t = 0$ to $t = T$.
5) Record $(P(t), Q(t)) \, \forall \, t \in [0,\, T]$ as $(P_{an}(t), Q_{an}(t))$.
6) Pick a large $N_4 \in \mathbb{N}$.
7) Pick $(\zeta_1^{(i)}, \omega_{n1}^{(i)}, \gamma_1^{(i)}, \zeta_2^{(i)}, \omega_{n2}^{(i)}, \gamma_2^{(i)})$ for $i = 1, 2, \ldots, N_4$.
8) Use the $\varphi_1$ and $\varphi_2$ identified in Step 1.
9) Use the $\tau_1$ and $\tau_2$ identified in Step 2.
10) Pick any $(\mu_{w1}(0), \dot{\mu}_{w1}(0), P(0), \mu_{w2}(0), \dot{\mu}_{w2}(0), Q(0))$.
11) Loop over $i = 1, 2, \ldots, N_4$.
12)     Let $(\zeta_1, \omega_{n1}, \gamma_1, \zeta_2, \omega_{n2}, \gamma_2) = (\zeta_1^{(i)}, \omega_{n1}^{(i)}, \gamma_1^{(i)}, \zeta_2^{(i)}, \omega_{n2}^{(i)}, \gamma_2^{(i)})$.
13)     Simulate the model (4.8)–(4.11) from $t = 0$ to $t = T$.
14)     Record $(P(t), Q(t)) \, \forall \, t \in [0,\, T]$ as $(P_{ap}^{(i)}(t), Q_{ap}^{(i)}(t))$.
15)     Calculate
            $J_1(\zeta_1^{(i)}, \omega_{n1}^{(i)}, \gamma_1^{(i)}) = (\int_{T_1}^{T} |P_{an}(t) - P_{ap}^{(i)}(t)|^{p_1} dt)^{\frac{1}{p_1}},$
            $J_2(\zeta_2^{(i)}, \omega_{n2}^{(i)}, \gamma_2^{(i)}) = (\int_{T_2}^{T} |Q_{an}(t) - Q_{ap}^{(i)}(t)|^{p_2} dt)^{\frac{1}{p_2}},$
        where $T_1 \in (0,\, T)$, $T_2 \in (0,\, T)$, $p_1 \geq 1$, and $p_2 \geq 1$.
16) End loop.
17) Let $(\zeta_1, \omega_{n1}, \gamma_1)$ be the $(\zeta_1^{(i)}, \omega_{n1}^{(i)}, \gamma_1^{(i)})$ that minimizes $J_1(\zeta_1^{(i)}, \omega_{n1}^{(i)}, \gamma_1^{(i)})$, and
    $(\zeta_2, \omega_{n2}, \gamma_2)$ be the $(\zeta_2^{(i)}, \omega_{n2}^{(i)}, \gamma_2^{(i)})$ that minimizes $J_2(\zeta_2^{(i)}, \omega_{n2}^{(i)}, \gamma_2^{(i)})$.
```

Remark 4.4. In the above procedure, T may be different from the T in Steps 1 and 2; $P_d(t)$ and $Q_d(t)$ may be, say, staircases, ramps, or from realistic profiles; $V_w(t)$ may be from real data; and $(\zeta_1^{(i)}, \omega_{n1}^{(i)}, \gamma_1^{(i)}, \zeta_2^{(i)}, \omega_{n2}^{(i)}, \gamma_2^{(i)})$ for $i = 1, 2, \ldots, N_4$ represent the search space for the best $(\zeta_1, \omega_{n1}, \gamma_1, \zeta_2, \omega_{n2}, \gamma_2)$.

Note that the three procedures in Steps 1–3 collectively form a parameter identification scheme, which enables sequential determination of all the parameters of the approximate model (4.8)–(4.11) (i.e., φ_1 and φ_2, then τ_1 and τ_2, then the rest).

4.3.2 Approximating the Empirical Model

As was mentioned in Section 4.2.2, in practice we may be given an empirical model of a WTCS, defined by input-output measurement data of the form (4.3), and asked to design a WFC. Thus, it is desirable that our approximate model (4.8)–(4.11)—with suitable choices of parameters—can also imitate the empirical model (4.3), producing outputs that closely resemble the last two columns of (4.3), when the inputs are from the first three columns. To come up with such suitable choices, reconsider the parameter identification scheme from Steps 1–3. Observe that this scheme is not immediately applicable here because Steps 1 and 2 require constant and staircase inputs $(P_d(t), Q_d(t), V_w(t))$, but with the empirical model (4.3) the inputs $(P_d(i\Delta), Q_d(i\Delta), V_w(i\Delta))$ are whatever that are given. To circumvent this issue, below we modify the scheme, allowing it to handle any given inputs, and label the steps involved Steps 1'–3', to distinguish them from, and to stress their parallel with, Steps 1–3 above. The modification yields the second parameter identification scheme, intended just for the empirical case.

Step 1': Identifying the functions φ_1 and φ_2

Parallel to Step 1, the goal of this Step 1' is to construct a procedure for identifying the functions φ_1 and φ_2, so that the basic model (4.4) and (4.5) in Figure 4.2(a) is able to roughly mimic the empirical model (4.3). To do so, observe that the identification of φ_1 (and, similarly, φ_2) can be treated as a curve-fitting problem with domain containing the inputs $(P_d(i\Delta), Q_d(i\Delta), V_w(i\Delta))$ and range containing the output $P(i\Delta)$. Also observe that if we partition the domain into $U_1, U_2, \ldots, U_n$ and write φ_1 as

$$\varphi_1(P_d, Q_d, V_w) = \sum_{j=1}^{n} \alpha_j \mathbf{1}_{U_j}(P_d, Q_d, V_w),$$

where α_j are the parameters and $\mathbf{1}_{U_j}(P_d, Q_d, V_w)$ are the set indicator basis functions (see Chapter 5.4 of [70]), then the optimal α_j in the least-squares sense can be easily computed: each α_j is simply the average of those $P(i\Delta)$ for which $(P_d(i\Delta), Q_d(i\Delta), V_w(i\Delta)) \in U_j$. These observations suggest the following procedure, in which we partition the domain into three-dimensional grids, for simplicity:

Procedure for Step 1'

---

1) Let

$$P_{d,\max} = \max_{0\le i\le D-1} P_d(i\Delta), P_{d,\min} = \min_{0\le i\le D-1} P_d(i\Delta), Q_{d,\max} = \max_{0\le i\le D-1} Q_d(i\Delta),$$
$$Q_{d,\min} = \min_{0\le i\le D-1} Q_d(i\Delta), V_{w,\max} = \max_{0\le i\le D-1} V_w(i\Delta), V_{w,\min} = \min_{0\le i\le D-1} V_w(i\Delta).$$

2) Pick a large $N_5 \in \mathbb{N}$.

3) Let $\delta P_d = \frac{P_{d,\max}-P_{d,\min}}{N_5}$, $\delta Q_d = \frac{Q_{d,\max}-Q_{d,\min}}{N_5}$, and $\delta V_w = \frac{V_{w,\max}-V_{w,\min}}{N_5}$.

4) Loop over $(j,\, k,\, l) \in \{1,\, 2, \ldots,\, N_5\}^3$.

5) Let $I = \{i \in \{0, 1, \ldots, D-1\} \mid P_d(i\Delta) \in [P_{d,\min} + (j-1)\delta P_d,\, P_{d,\min} + j\delta P_d),\ Q_d(i\Delta) \in [Q_{d,\min} + (k-1)\delta Q_d,\, Q_{d,\min} + k\delta Q_d),\ V_w(i\Delta) \in [V_{w,\min} + (l-1)\delta V_w,\, V_{w,\min} + l\delta V_w)\}$.

6) If $I \neq \emptyset$, let

$$\varphi_1\Big(P_{d,\min}+(j-\tfrac{1}{2})\delta P_d, Q_{d,\min}+(k-\tfrac{1}{2})\delta Q_d, V_{w,\min}+(l-\tfrac{1}{2})\delta V_w\Big)=\frac{\sum_{i\in I} P(i\Delta)}{|I|},$$
$$\varphi_2\Big(P_{d,\min}+(j-\tfrac{1}{2})\delta P_d, Q_{d,\min}+(k-\tfrac{1}{2})\delta Q_d, V_{w,\min}+(l-\tfrac{1}{2})\delta V_w\Big)=\frac{\sum_{i\in I} Q(i\Delta)}{|I|},$$

where $|I|$ denotes the cardinality of I.

7) End loop.

8) Determine φ_1 and φ_2 via interpolation on the (at most) N_5^3 data points obtained.

Step 2': Identifying the parameters τ_1 and τ_2

Unlike going from Step 1 to Step 1' where the procedure undergoes significant changes, only minor modifications are needed to make the procedures in Steps 2 and 3 applicable to the empirical model (4.3) in this Step 2' and the next Step 3'. In particular, the inputs now come from the first three columns of (4.3), p_1 and p_2 now represent the desired ℓ_p norms, and n_1 and n_2 now play the role of T_1 and T_2 in nullifying the impact of the initial states:

Procedure for Step 2'

```
1) Rename $(P(i\Delta),Q(i\Delta))$ from the empirical model (4.3) as $(P_{em}(i\Delta),Q_{em}(i\Delta))$.
2) Pick a large $N_6 \in \mathbb{N}$.
3) Pick $\tau_1^{(j)} > 0$ and $\tau_2^{(j)} > 0$ for $j = 1, 2, \ldots, N_6$.
4) Use the $\varphi_1$ and $\varphi_2$ identified in Step 1'.
5) Pick any $(P(0), Q(0))$.
6) Loop over $j = 1, 2, \ldots, N_6$.
7) Let $\tau_1 = \tau_1^{(j)}$ and $\tau_2 = \tau_2^{(j)}$.
8) Simulate the refined model (4.6) and (4.7) from $t = 0$ to $t = (D-1)\Delta$.
```

```
 9) Record $(P(t), Q(t))\ \forall\, t \in [0, (D-1)\Delta]$ as $(P_{ap}^{(j)}(t), Q_{ap}^{(j)}(t))$.
10) Calculate
        $J_1(\tau_1^{(j)}) = (\sum_{n=n_1}^{D-1} |P_{em}(n\Delta) - P_{ap}^{(j)}(n\Delta)|^{p_1})^{\frac{1}{p_1}},$
        $J_2(\tau_2^{(j)}) = (\sum_{n=n_2}^{D-1} |Q_{em}(n\Delta) - Q_{ap}^{(j)}(n\Delta)|^{p_2})^{\frac{1}{p_2}},$
    where $0 < n_1 < D-1$, $0 < n_2 < D-1$, $p_1 \geq 1$, and $p_2 \geq 1$.
11) End loop.
12) Let $\tau_1 = \arg\min_{\tau \in \{\tau_1^{(1)}, \ldots, \tau_1^{(N_6)}\}} J_1(\tau)$, and $\tau_2 = \arg\min_{\tau \in \{\tau_2^{(1)}, \ldots, \tau_2^{(N_6)}\}} J_2(\tau)$.
```

Step 3': Identifying the parameters ζ_1, ω_{n1}, γ_1, ζ_2, ω_{n2}, and γ_2

Procedure for Step 3'

```
 1) Rename $(P(i\Delta), Q(i\Delta))$ from the empirical model (4.3) as $(P_{em}(i\Delta), Q_{em}(i\Delta))$.
 2) Pick a large $N_7 \in \mathbb{N}$.
 3) Pick $(\zeta_1^{(j)}, \omega_{n1}^{(j)}, \gamma_1^{(j)}, \zeta_2^{(j)}, \omega_{n2}^{(j)}, \gamma_2^{(j)})$ for $j = 1, 2, \ldots, N_7$.
 4) Use the $\varphi_1$ and $\varphi_2$ identified in Step 1'.
 5) Use the $\tau_1$ and $\tau_2$ identified in Step 2'.
 6) Pick any $(\mu_{w1}(0), \dot{\mu}_{w1}(0), P(0), \mu_{w2}(0), \dot{\mu}_{w2}(0), Q(0))$.
 7) Loop over $j = 1, 2, \ldots, N_7$.
 8) Let $(\zeta_1, \omega_{n1}, \gamma_1, \zeta_2, \omega_{n2}, \gamma_2) = (\zeta_1^{(j)}, \omega_{n1}^{(j)}, \gamma_1^{(j)}, \zeta_2^{(j)}, \omega_{n2}^{(j)}, \gamma_2^{(j)})$.
 9) Simulate the approximate model (4.8)–(4.11) from $t = 0$ to $t = (D-1)\Delta$.
10) Record $(P(t), Q(t))\ \forall\, t \in [0, (D-1)\Delta]$ as $(P_{ap}^{(j)}(t), Q_{ap}^{(j)}(t))$.
```

11) Calculate

$$J_1(\zeta_1^{(j)}, \omega_{n1}^{(j)}, \gamma_1^{(j)}) = (\sum_{n=n_1}^{D-1} |P_{em}(n\Delta) - P_{ap}^{(j)}(n\Delta)|^{p_1})^{\frac{1}{p_1}},$$

$$J_2(\zeta_2^{(j)}, \omega_{n2}^{(j)}, \gamma_2^{(j)}) = (\sum_{n=n_2}^{D-1} |Q_{em}(n\Delta) - Q_{ap}^{(j)}(n\Delta)|^{p_2})^{\frac{1}{p_2}},$$

where $0 < n_1 < D - 1$, $0 < n_2 < D - 1$, $p_1 \geq 1$, and $p_2 \geq 1$.

12) End loop.

13) Let $(\zeta_1, \omega_{n1}, \gamma_1)$ be the $(\zeta_1^{(j)}, \omega_{n1}^{(j)}, \gamma_1^{(j)})$ that minimizes $J_1(\zeta_1^{(j)}, \omega_{n1}^{(j)}, \gamma_1^{(j)})$, and $(\zeta_2, \omega_{n2}, \gamma_2)$ be the $(\zeta_2^{(j)}, \omega_{n2}^{(j)}, \gamma_2^{(j)})$ that minimizes $J_2(\zeta_2^{(j)}, \omega_{n2}^{(j)}, \gamma_2^{(j)})$.

Remark 4.5. The approximate model (4.8)–(4.11) in this section may be viewed as the WTCS$^\theta$ in Section 4.1, with $\theta = (\varphi_1, \tau_1, \zeta_1, \omega_{n1}, \gamma_1, \varphi_2, \tau_2, \zeta_2, \omega_{n2}, \gamma_2)$. Also, it may be regarded as satisfying (C2) in Section 4.1 because it has isolated static nonlinearities and is relatively simple compared to full-blown WTCS models, such as those in Section 4.4.

4.4 Validation of the Approximate Model

In this section, we validate via simulation the approximate model developed in Section 4.3, showing that it is capable of closely imitating several analytical and empirical WTCS models from the literature and from real data. To enable the validation, we first describe a wind turbine model, followed by the analytical and empirical WTCS models considered. We then describe the validation settings and results.

4.4.1 Wind Turbine Model

Consider a variable-speed wind turbine with a DFIG[1], modeled by the following differential and algebraic equations [4, 63]:

$$
\begin{aligned}
\dot{\varphi}_{ds} &= -\frac{R_s}{\sigma L_s}\varphi_{ds} + \omega_s\varphi_{qs} + \frac{R_sL_m}{\sigma L_sL_r}\varphi_{dr} + v_{ds},\\
\dot{\varphi}_{qs} &= -\omega_s\varphi_{ds} - \frac{R_s}{\sigma L_s}\varphi_{qs} + \frac{R_sL_m}{\sigma L_sL_r}\varphi_{qr} + v_{qs},\\
\dot{\varphi}_{dr} &= \frac{R_rL_m}{\sigma L_sL_r}\varphi_{ds} - \frac{R_r}{\sigma L_r}\varphi_{dr} + (\omega_s - \omega_r)\varphi_{qr} + v_{dr},\\
\dot{\varphi}_{qr} &= \frac{R_rL_m}{\sigma L_sL_r}\varphi_{qs} - (\omega_s - \omega_r)\varphi_{dr} - \frac{R_r}{\sigma L_r}\varphi_{qr} + v_{qr},\\
J\dot{\omega}_r &= T_m - T_e - C_f\omega_r,\\
\varphi_{ds} &= L_si_{ds} + L_mi_{dr}, \quad \varphi_{qs} = L_si_{qs} + L_mi_{qr},\\
\varphi_{dr} &= L_mi_{ds} + L_ri_{dr}, \quad \varphi_{qr} = L_mi_{qs} + L_ri_{qr},\\
P_s &= -v_{ds}i_{ds} - v_{qs}i_{qs}, \quad Q_s = -v_{qs}i_{ds} + v_{ds}i_{qs},\\
P_r &= -v_{dr}i_{dr} - v_{qr}i_{qr}, \quad Q_r = -v_{qr}i_{dr} + v_{dr}i_{qr},\\
P &= P_s + P_r, \quad Q = Q_s + Q_r,
\end{aligned}
$$

where s, r denote the stator and rotor; d, q the dq frame; $\varphi_{ds}, \varphi_{qs}, \varphi_{dr}, \varphi_{qr}$ the fluxes; $v_{ds}, v_{qs}, v_{dr}, v_{qr}$ the voltages; $i_{ds}, i_{qs}, i_{dr}, i_{qr}$ the currents; R_s, R_r the resistances; L_s, L_r, L_m the inductances; $\sigma = 1 - \frac{L_m^2}{L_sL_r}$ the leakage coefficient; ω_s the constant angular velocity of the synchronously rotating reference frame; ω_r the rotor angular velocity; J the rotor moment of inertia; C_f the friction coefficient; $T_m = \frac{1}{2}\rho AC_p(\lambda, \beta)V_w^3/\omega_r$ the mechanical torque; $T_e = \varphi_{qs}i_{ds} - \varphi_{ds}i_{qs}$ the electromagnetic torque; ρ the air density; $A = \pi R^2$ the rotor swept area of radius R; $C_p(\lambda, \beta)$ the C_p-surface; $\lambda = \frac{\omega_rR}{V_w}$ the tip speed ratio; and β the blade pitch angle.

---

[1] Due to space limitation, only DFIG is considered in the model validation. We note, however, that other types of generators, such as IG, may be implemented in a similar manner.

In addition, to have some diversity in the validation, consider the following two distinct sets of values for the wind turbine parameters: the first set of value is adopted from MATLAB/Simulink R2007a and corresponds to a GE 1.5 MW turbine, which is listed in Section 2.4, while the second is adopted from [80, 81] and corresponds to a GE 3.6 MW turbine, whose values are: $R = 52\,\mathrm{m}$, $\omega_s(\mathrm{pu}) = 1$, $R_s(\mathrm{pu}) = 0.0079$, $R_r(\mathrm{pu}) = 0.025$, $L_s(\mathrm{pu}) = 4.47937$, $L_r(\mathrm{pu}) = 4.8$, $L_m(\mathrm{pu}) = 4.4$, $J(\mathrm{pu}) = 10.38$, $C_f(\mathrm{pu}) = 0$, $V_{w\_\mathrm{base}} = 12\,\mathrm{m/s}$, and the C_p-surface is given by $C_p(\lambda, \beta) = \sum_{i=0}^{4} \sum_{j=0}^{4} \alpha_{ij} \beta^i \lambda^j$, where $\alpha_{44} = 4.9686 \times 10^{-10}$, $\alpha_{43} = -7.1535 \times 10^{-8}$, $\alpha_{42} = 1.6167 \times 10^{-6}$, $\alpha_{41} = -9.4839 \times 10^{-6}$, $\alpha_{40} = 1.4787 \times 10^{-5}$, $\alpha_{34} = -8.9194 \times 10^{-8}$, $\alpha_{33} = 5.9924 \times 10^{-6}$, $\alpha_{32} = -1.0479 \times 10^{-4}$, $\alpha_{31} = 5.7051 \times 10^{-4}$, $\alpha_{30} = -8.6018 \times 10^{-4}$, $\alpha_{24} = 2.7937 \times 10^{-6}$, $\alpha_{23} = -1.4855 \times 10^{-4}$, $\alpha_{22} = 2.1495 \times 10^{-3}$, $\alpha_{21} = -1.0996 \times 10^{-2}$, $\alpha_{20} = 1.5727 \times 10^{-2}$, $\alpha_{14} = -2.3895 \times 10^{-5}$, $\alpha_{13} = 1.0683 \times 10^{-3}$, $\alpha_{12} = -1.3934 \times 10^{-2}$, $\alpha_{11} = 6.0405 \times 10^{-2}$, $\alpha_{10} = -6.7606 \times 10^{-2}$, $\alpha_{04} = 1.1524 \times 10^{-5}$, $\alpha_{03} = -1.3365 \times 10^{-4}$, $\alpha_{02} = -1.2406 \times 10^{-2}$, $\alpha_{01} = 2.1808 \times 10^{-1}$, and $\alpha_{00} = -4.1909 \times 10^{-1}$.

4.4.2 WTCS Models

Next, consider four analytical WTCS models from the literature and an empirical WTCS model from real data, labeled as *WTCS1*–*WTCS5* and defined as follows:

WTCS1 is made up of the GE 3.6 MW turbine model and the controller in Rodriguez-Amenedo et al. [1], which regulates $P(t)$ and $Q(t)$ by adjusting $\beta(t)$, $v_{qr}(t)$, and $v_{dr}(t)$ using five PI blocks and a power-speed lookup table, as depicted in Figure 4.3(a). Note that this controller assumes that the d-axis of the synchronously rotating reference frame is aligned with the stator flux vector, i.e., $(\varphi_{ds}(t), \varphi_{qs}(t)) = (1, 0)$, and that the reactive power is solely

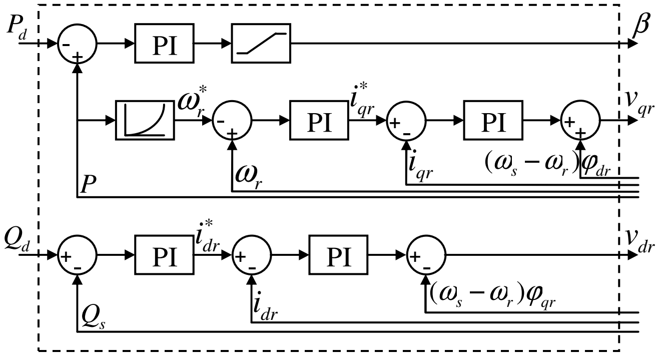

(a) Block diagram of the controller in Rodriguez-Amenedo et al. [1].

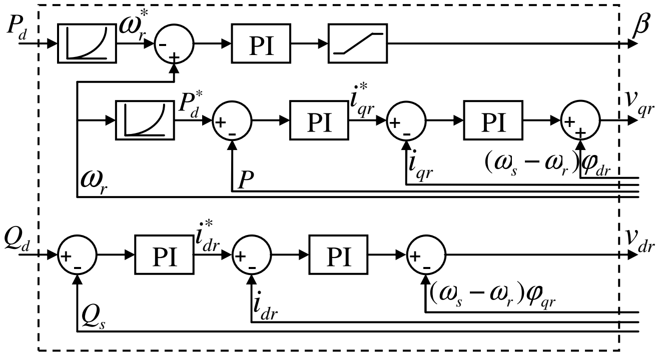

(b) Block diagram of the controller in Fernandez et al. [2].

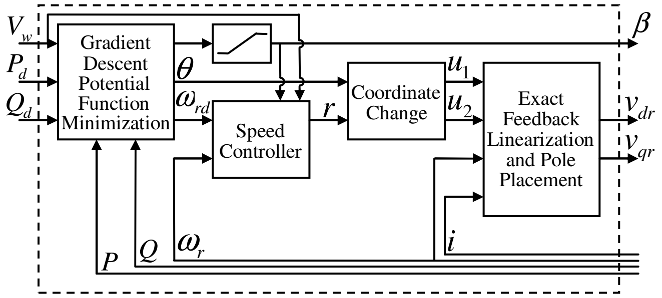

(c) Block diagram of the controller in Tang et al. [3].

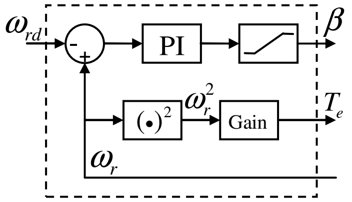

(d) Block diagram of the controller in Johnson et al. [4].

Figure 4.3: Block diagrams of the controllers that yield WTCS1–WTCS4.

coming from the stator, i.e., $Q(t) = Q_s(t)$. For more information about this controller, see [1] and related work [39], [2] (in particular, Figures 3 of [1], 10 of [39], and 6 and 7 of [2]).

WTCS2 is made up of the same GE 3.6 MW turbine model and the controller studied in Fernandez et al. [2] and displayed in Figure 4.3(b). Observe that this controller is similar to the one in [1] except that it uses $\omega_r(t)$ to determine $\beta(t)$ in the outer loop and $P(t)$ to determine $v_{qr}(t)$ in the inner loop, whereas the one in [1] does the opposite. For more details about this controller, see [2] and [5] (especially, Figures 6 and 8 of [2] and 4 of [5]).

WTCS3, unlike WTCS1 and WTCS2, is made up of the smaller GE 1.5 MW turbine model and the nonlinear dual-mode controller in Tang et al. [3], which uses the feedback linearization technique to cancel nonlinearities in the DFIG dynamics, and the gradient descent method to maximize or regulate $P(t)$ and $Q(t)$ including the power factor, as outlined in Figure 4.3(c). Notice that this controller assumes instead that the d-axis is aligned with the stator voltage vector, i.e., $(v_{ds}(t), v_{qs}(t)) = (1, 0)$, and that it does not assume $Q(t) = Q_s(t)$.

WTCS4 is formed by the mechanical dynamics of the GE 1.5 MW turbine model and the controller in Johnson et al. [4], which is implemented on the Controls Advanced Research Turbine (CART) at the National Renewable Energy Laboratory's (NREL's) National Wind Technology Center (NWTC) and also discussed in [12]. Sketched in Figure 4.3(d), this controller maximizes the power capture $T_m(t)\omega_r(t)$ in Region 2 by varying $T_e(t)$ and keeping $\beta(t)$ at its optimum, and prevents the power capture from exceeding the rated value in Region 3 by varying $\beta(t)$ accordingly. In contrast to WTCS1–WTCS3, this WTCS assumes no electrical dynamics and, thus, does not involve $Q_d(t)$ and

$Q(t)$, nor $P_d(t)$.

Finally, **WTCS5**—the only empirical model considered in this chapter—is a black box defined by a set of input-output measurement data taken from an actual GE 1.5 MW turbine within a wind farm located in northwest Oklahoma. This set of data has $D = 34,208$ data points and was collected over 238 days at a sampling period of $\Delta = 10$ minutes. Moreover, the set of data fits the mold of (4.3), containing the mandatory $V_w(i\Delta)$ and $P(i\Delta)$ for $i = 0, 1, \ldots, D-1$, but not the optional $P_d(i\Delta)$, $Q_d(i\Delta)$, and $Q(i\Delta)$. In order to use this data set for second-level simulation in the sequel, we redefine Δ as $\Delta = 10/24$ minutes, assuming that one-day worth of data were taken over an hour.

4.4.3 Validation Settings

Given WTCS1–WTCS5, suppose now we want to construct, for each WTCSi, an approximate model (4.8)–(4.11) that resembles its behavior. To this end, for each WTCSi, we execute the first parameter identification scheme in Steps 1–3 (if WTCSi is analytical), or the second one in Steps 1'–3' (if it is empirical), to obtain a specific approximate model with specific values of φ_1, τ_1, ζ_1, ω_{n1}, γ_1 as well as φ_2, τ_2, ζ_2, ω_{n2}, γ_2 (if the optional $Q(t)$ is indeed an output of WTCSi).

To evaluate how well the five approximate models imitate WTCS1–WTCS5, we consider 30 different scenarios. For each scenario, we generate inputs $(P_d(t), Q_d(t), V_w(t))$ from $t = 0$ to $t = 3600$ seconds, choosing $P_d(t)$ to be a staircase signal with three random staircase values each lasting 1200 seconds, $Q_d(t)$ to be such that the desired power factor $\frac{P_d(t)}{\sqrt{P_d^2(t)+Q_d^2(t)}}$ is kept constant at 0.995, and $V_w(t)$ to be an actual wind profile from the aforementioned wind farm. For each WTCSi and each scenario, we simulate both

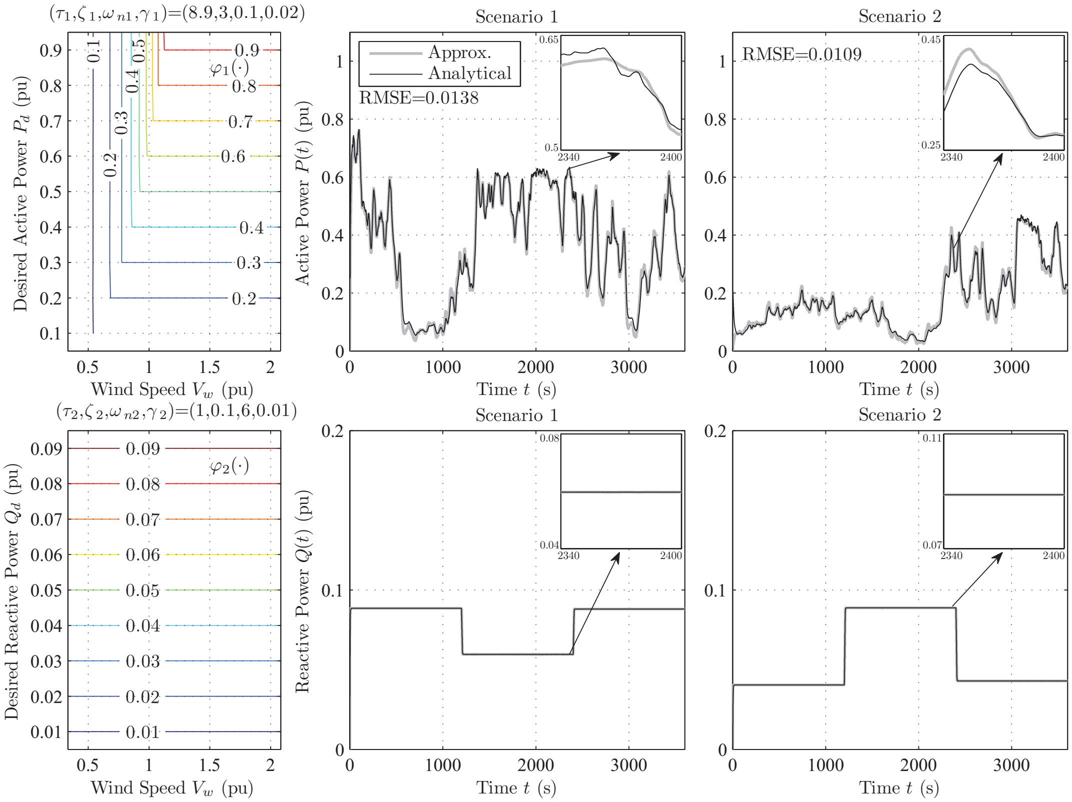

Figure 4.4: Imitating WTCS1 defined by the GE 3.6 MW turbine and the controller in Rodriguez-Amenedo et al. [1].

WTCSi and its corresponding approximate model for 3600 seconds using the *same* inputs $(P_d(t), Q_d(t), V_w(t))$ associated with the scenario, record the outputs $(P(t), Q(t))$ of the two models, and calculate the root-mean-square error (RMSE) in $P(t)$ between the two models after some initial transient. (Obviously, the smaller the RMSE, the better the approximation.)

4.4.4 Validation Results

Figures 4.4–4.8 depict, respectively, the five approximate models and how well they resemble WTCS1–WTCS5. Although the figures have different sizes and styles, they share the same format: the first row of subplots is associated with the active power; the second row, if present, is associated with

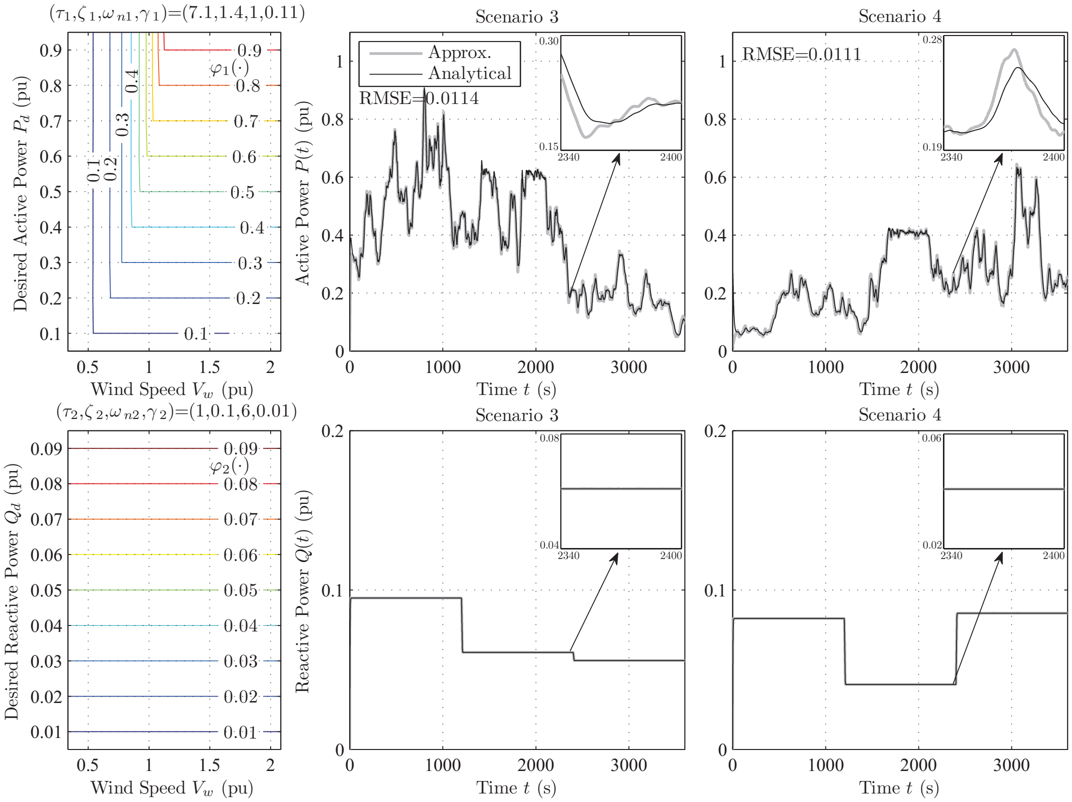

Figure 4.5: Imitating WTCS2 defined by the GE 3.6 MW turbine and the controller in Fernandez et al. [2].

the reactive power; the first column displays the identified values of the approximate model parameters φ_1, τ_1, ζ_1, ω_{n1}, γ_1, φ_2, τ_2, ζ_2, ω_{n2}, γ_2, showing φ_1 and φ_2 as contour plots in Figures 4.4–4.6 and as graphs in Figures 4.7 and 4.8; and the second and third columns each shows, for a selected scenario, the outputs $(P(t), Q(t))$ of WTCSi and those of its corresponding approximate model over 3600 seconds and over 60 seconds, the latter in zoom-in windows. Notice that although, in general, φ_1 and φ_2 are functions of (P_d, Q_d, V_w), for WTCS1–WTCS3 they are functions of only (P_d, V_w) or equivalently (Q_d, V_w) (since $Q_d = 0.1P_d$ in order to obtain a desired power factor of 0.995), and for WTCS4 and WTCS5 they are functions of only V_w (since P_d is not required).

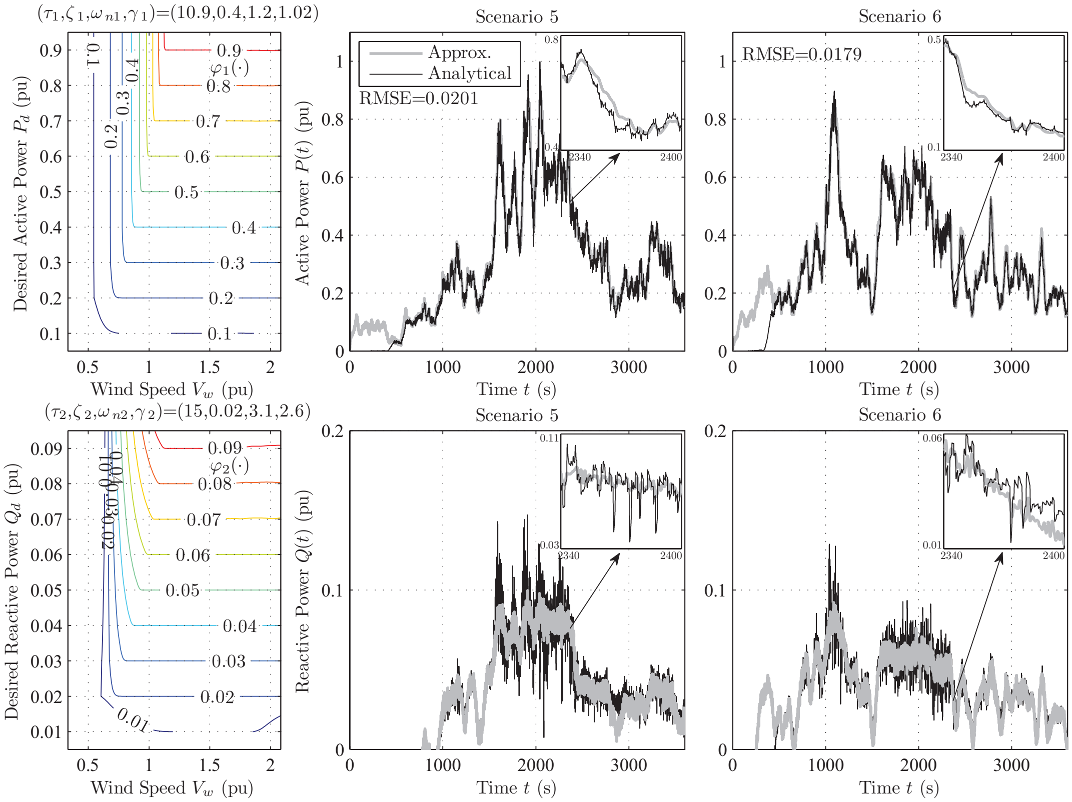

Figure 4.6: Imitating WTCS3 defined by the GE 1.5 MW turbine and the controller in Tang et al. [3].

This explains why φ_1 and φ_2 can be shown as contour plots and graphs. Also note that due to space limitation, for each WTCSi, we could only show the outputs for two selected scenarios (as opposed to showing both the inputs and outputs for all the 30 scenarios). Finally, each gray dot in subplot 1 of Figure 4.8 represents an empirical data point (V_w, P) for WTCS5 and is included just to provide additional insight.

Complementing Figures 4.4–4.8 is Table 4.1, which shows the minimum, maximum, and average RMSE in $P(t)$ between WTCS1–WTCS5 and their corresponding approximate models, taken over all the 30 scenarios. To get a sense of what the numbers in the table mean, one may refer to Figures 4.4–4.8,

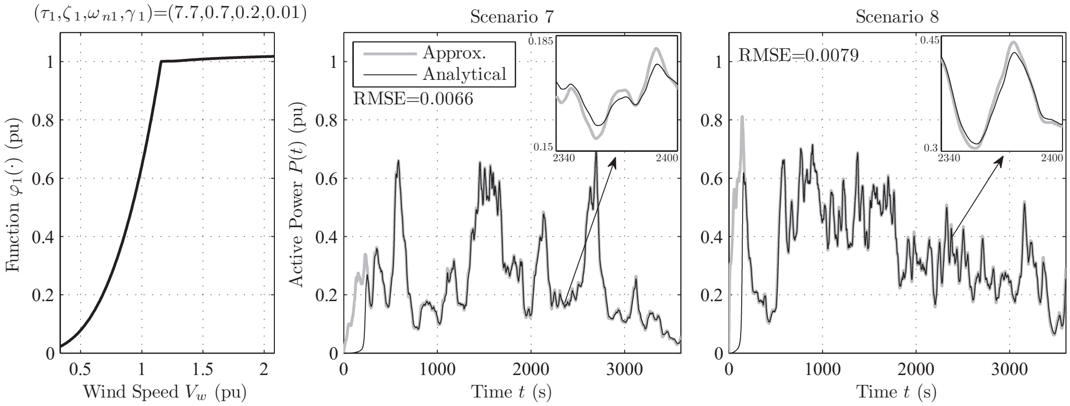

Figure 4.7: Imitating WTCS4 defined by the mechanical dynamics of the GE 1.5 MW turbine and the controller in Johnson et al. [4].

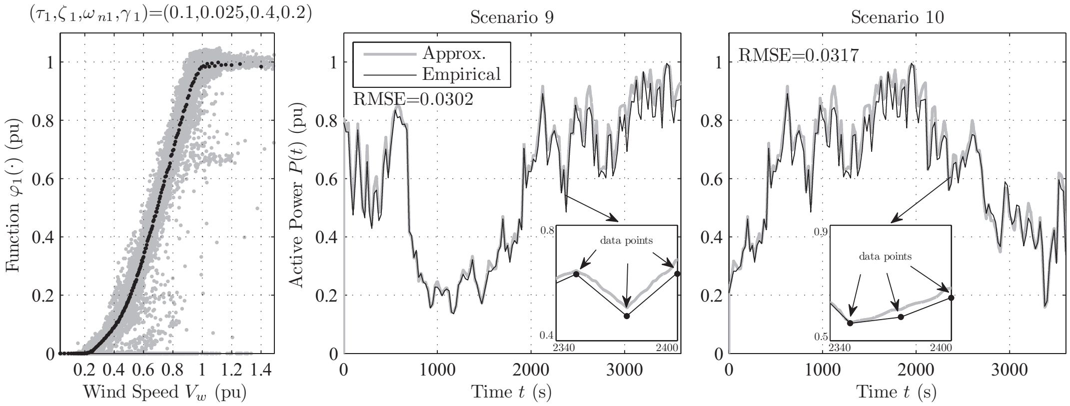

Figure 4.8: Imitating WTCS5 defined by real data from an Oklahoma wind farm.

Table 4.1: Minimum, maximum, and average Root-Mean-Square Error (RMSE) in $P(t)$ taken over 30 scenarios for each WTCSi.

	Min.	Max.	Avg.
WTCS1	0.0103	0.0178	0.0134
WTCS2	0.0111	0.0164	0.0137
WTCS3	0.0111	0.0237	0.0163
WTCS4	0.0056	0.0088	0.0072
WTCS5	0.0223	0.0578	0.0320

which also state the RMSEs of the $P(t)$ curves for the few selected scenarios.

Observe from Figures 4.4–4.8 and Table 4.1 that while the proposed approximate model is not without error, the magnitude of which is generally very small, sometimes even negligible, across all WTCSs and all scenarios. In particular, it is able to produce the right "peaks" and "valleys" at the right moments in all the 3600-seconds subplots and the 60-seconds zoom-in windows—except for the first 500 seconds in Figure 4.6 and first 200 seconds in Figure 4.7, which may be attributed to the approximate and analytical models having different initial states and, hence, different initial transients. These encouraging observations validate the approximate model in Figure 4.2(c), demonstrating its ability to closely replicate the behaviors of the five fairly different analytical and empirical WTCS models considered.

Remark 4.6. The validation in this section may be thought of as verifying (C1) and (C3) in Section 4.1.

4.5 Conclusion

In this chapter, we have presented a simple approximate model, which tries to mimic generic analytical and empirical WTCS models, along with two parameter identification schemes, which determine the approximate model parameters in both cases. We have also demonstrated through simulation the accuracy and versatility of the approximate model in resembling several different analytical and empirical WTCS models from the literature and from real data. From the results, we conclude that the approximate model is a compelling candidate, based on which one may design and analyze a second-to-minute-timescale supervisory wind farm controller using advanced control techniques (e.g., model predictive control [82], distributed cooperative control [83], and quasilinear control [84]), in future research.

Chapter 5 Model Predictive and Adaptive Wind Farm Power Control

5.1 Introduction

Wind farms able to produce power outputs that accurately and smoothly track desired references from a grid operator despite the intermittency of wind, are important for a number of reasons. First, this ability allows them to be treated more or less as "controllable" generation resources, similar to conventional power plants. Second, this ability reduces their reliance on expensive ancillary services, leading to more economic operation. Finally, with the increasing penetration of wind power in the generation portfolios of many countries, this ability of the wind farms becomes especially critical to power system reliability. Therefore, a wind farm controller (WFC), which provides a wind farm with such accurate and smooth tracking ability, is valuable.

To date, a relatively small number of WFCs, developed based on different techniques and for different purposes, have been proposed in the literature [1, 2, 5, 50, 52, 85, 86]. For instance, [52] and [50] adopted an optimization-based approach toward designing WFCs, which could respond to grid operator commands. As another example, [85] utilized a proportional-integral regulator-based method for managing the reactive powers of wind farms. As yet another example, [2] carried out simulation studies that compared the behaviors of a few existing WFCs.

Although these publications provide some understanding on the capability and limitations of specific wind farm control systems (WFCSs), a number of key issues surrounding WFCs design and analysis remain unaddressed. First, majority of the existing work did not attempt optimization, and those that did attempt did not incorporate forecast of wind speeds and future values of the desired wind farm power output, even though they are typically available. It is conceivable that taking into account such information may lead to WFC designs that yield better tracking performance. Second, wind farm power tracking is, mathematically, a problem with a large degree of freedom: as far as the grid operator is concerned, all that matters is that the sum of all the turbine power outputs is approximately equal to the desired reference. Thus, if there are N turbines in the wind farm, there are $N - 1$ degrees of freedom left upon satisfying the aforementioned equality constraint. It is conceivable that these available degrees of freedom may be exploited to achieve other, secondary goals. For example, they may be used to minimize changes in the power commands sent to individual turbines, leading to less changes in the electrical and mechanical turbine states and, thus, possibly less frequent maintenance and longer operational lifetime. Finally, smoothness of the wind farm power output has largely been unaddressed, or addressed merely through simulations studies. To the best of our knowledge, no theoretical analysis on smoothness has been carried out, and no rigorous means of improving smoothness through cooperative control has been developed.

This chapter is devoted to the design and analysis of a WFC that addresses the aforementioned issues. We consider a WFCS comprising a wind farm and its WFC, as shown in Figure 5.1. The wind farm consists of N WTCSs, where each WTCS i is made up of a wind turbine and its con-

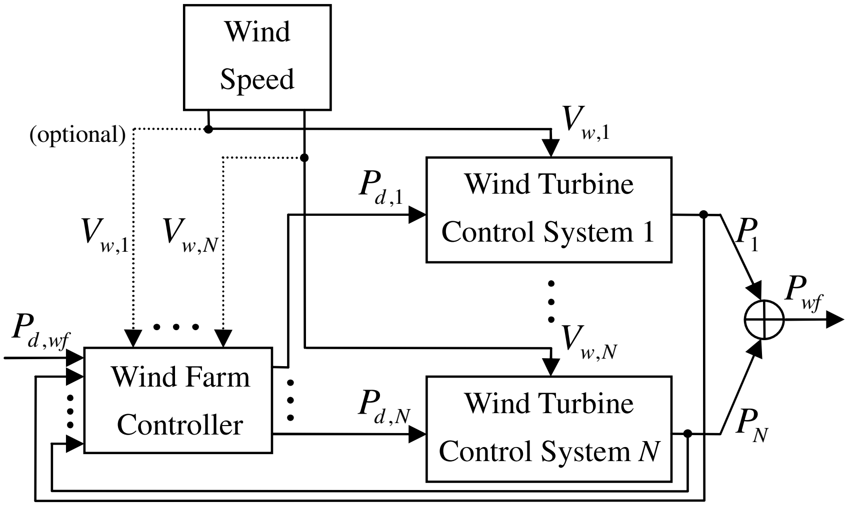

Figure 5.1: Block diagram of the wind farm control system (WFCS).

troller. Accompanying the WFCS is a wind speed block, which produces wind speeds $V_{w,1}, \ldots, V_{w,N}$, where each $V_{w,i}$ affects WTCS i and is possibly measured by the WFC. In addition to accepting $V_{w,i}$, each WTCS i accepts a desired power command $P_{d,i}$ from the WFC and produces power output P_i. Likewise, the WFC uses feedbacks of $P_1, \ldots, P_N$, measurements of $V_{w,1}, \ldots, V_{w,N}$, and a desired wind farm power output $P_{d,wf}$ from the grid operator to determine $P_{d,1}, \ldots, P_{d,N}$ that are sent to each WTCSs. Finally, the wind farm power output P_{wf} is defined as the sum of all the turbine power outputs, i.e., $P_{wf} = \sum_{i=1}^{N} P_i$.

The WFC developed in this chapter is made up of two components: a *model predictive controller* sitting on the outer loop, whose goal is to cooperatively optimize the receding horizon, deterministic tracking performance of the wind farm power output on a longer timescale, and an *adaptive controller* sitting on the inner loop, whose goal is to jointly optimize the steady-state, stochastic smoothness of the wind farm power output on a shorter timescale (see Figure 5.4 for a preview of the WFC). To achieve its goal, the model predictive controller, also known as a receding horizon controller [87], uses forecast of the wind speeds from crude measurements, forecast of the power demand from the grid operator, and feedback of the powers generated by the wind turbines to iteratively determine the desired power trajectories, which drive the WTCSs. Although model predictive control has been successfully utilized in many control applications, we believe its use in wind farm power control has not been reported. More important, this approach in our opinion is highly appropriate for the problem at hand as it addresses two of the three aforementioned issues, namely, exploitation of the available forecasts and design freedoms.

Likewise, to achieve its goal, the adaptive controller, which is of the *self-tuning regulator* [88] type, uses estimated wind speed characteristics (e.g., correlation and diversity) from measurements to adaptively tune the gains of a fully decentralized bank of proportional controllers, which precede the WTCSs. While adaptive control has found widespread use in several industries, we are not aware of its use in wind farm power control. Moreover, we believe this approach is particularly suitable for the problem in consideration as it enables smoothness-driven adaptation of the controller parameters to, for instance, changing wind directions and weather conditions, in addition to enabling smoothness analysis based on stochastic linear systems theory. Consequently, the approach may be regarded as addressing the third aforementioned issue on smoothness of the wind farm power output. Finally, in order to demonstrate the efficacy of the proposed WFC, we carry out several sets of simulations, which test the model predictive controller by itself, the adaptive controller by itself, and the WFC as a whole. We also illustrate the unique attributes of the WFC as compared with an existing WFC from [5].

The outline of this chapter is as follows: Section 5.2 models the wind farm and formulates the control problem. Section 5.3 introduces the proposed wind farm controller framework. Sections 5.4 and 5.5 detail, respectively, the development of the model predictive controller and adaptive controller. Section 5.6 studies via numerical simulation the behavior of the proposed WFC. Finally, Section 5.7 concludes the chapter.

5.2 Modeling and Problem Formulation

Recall from Figure 5.1 that the WFCS is accompanied by a wind speed block and is made up of $N \in \mathbb{N}$ WTCSs and a WFC, where $\mathbb{N} = \{1, 2, \dots\}$. In Section 5.2.1, we introduce a model describing the wind speed block. In Section 5.2.2, we present a model describing each of the N WTCSs. Finally, in Section 5.2.3, we formulate the problem of designing the WFC.

5.2.1 Wind Speed Model

Observe from Figure 5.1 that the wind speed block produces N wind speeds $V_{w,1}(t), \dots, V_{w,N}(t)$ entering turbines 1 through N. For each $i \in \{1, 2, \dots, N\}$, we assume that

$$V_{w,i}(t) = \bar{V}_{w,i}(t) + \tilde{V}_{w,i}(t), \tag{5.1}$$

where $t \geq 0$ denotes time, $\bar{V}_{w,i}(t) \in (0, \infty)$ represents the slow, average component of $V_{w,i}(t)$ on a minute-to-hour timescale, and $\tilde{V}_{w,i}(t) \in \mathbb{R}$ represents the fast, deviation-from-average component of $V_{w,i}(t)$ on a millisecond-to-second timescale. The slow components $\bar{V}_{w,1}(t), \dots, \bar{V}_{w,N}(t)$ are assumed to be deterministic and specified exogenously by, for example, actual empirical data or test signals. In contrast, the fast components $\tilde{V}_{w,1}(t), \dots, \tilde{V}_{w,N}(t)$ are assumed to be stochastic and given by

$$[\tilde{V}_{w,1}(t), \ldots, \tilde{V}_{w,N}(t)]^T = \mathcal{L}^{-1}\{G_w(s)\} * w(t), \tag{5.2}$$

where $*$ denotes the convolution operator, $\mathcal{L}^{-1}$ denotes the inverse Laplace transform, $w(t) \in \mathbb{R}^{N_w}$ is a stationary, zero-mean white Gaussian random process with autocovariance function $E\{w(t)w(\tau)^T\} = W\delta(t-\tau)$, $G_w(s)$ is an N-by-N_w, asymptotically stable transfer function matrix, $N_w \in \mathbb{N}$, E denotes the expectation operator, $W \in \mathbb{R}^{N_w \times N_w}$, $W = W^T > 0$, and δ denotes the Dirac delta function. As it follows from (5.2) and the above assumptions, $\tilde{V}_{w,1}(t), \ldots, \tilde{V}_{w,N}(t)$ are stationary, zero-mean colored Gaussian random processes. Note that because of $\tilde{V}_{w,i}(t)$ being Gaussian, $V_{w,i}(t)$ may be negative with a small probability despite $\bar{V}_{w,i}(t)$ being positive. For simplicity, however, we will allow for that in this chapter. Also note that, in reality, $\tilde{V}_{w,i}(t)$ can be non-stationary due to changes in wind direction, weather conditions, and turbine yaw angle. Again, for simplicity, we assume that such changes are slow, so that $\tilde{V}_{w,i}(t)$ may be considered stationary. Moreover, we let $G_w(s)$ above be a general transfer function matrix, although later on in Section 5.5, we assume a specific $G_w(s)$ for concreteness. Finally, the top portion of Figure 5.2 illustrates the wind speed model as described by (5.1) and (5.2).

5.2.2 Wind Turbine Control System Model

As was mentioned in Sections 4.1 and 5.1, a WTCS comprising a wind turbine and its controller may be a fairly complex nonlinear dynamical system, which creates obstacles in the design and analysis of a sophisticated WFC. This suggests a need to build a suitably simplified, approximate WTCS model, which is accomplished in the previous chapter. More specifically, we proposed

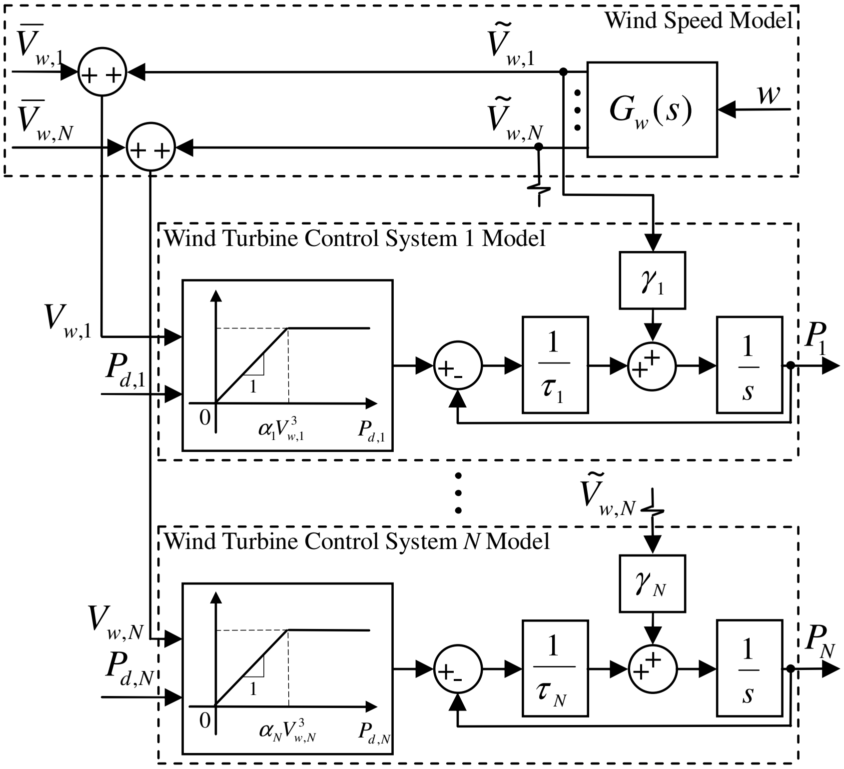

Figure 5.2: Block diagram of the wind speed model and wind turbine control system model.

an approximate model that is structurally simple and yet is capable of closely imitating the active and reactive power dynamics of several different WTCS models from the literature [1–4] and from real data taken from an Oklahoma wind farm. The approximate model is described by (4.8)–(4.11) and is illustrated in a block diagram form in Figure 4.2(c). Moreover, its accuracy has been validated through Section 4.4, which can be seen from Figures 4.4–4.8 and Table 4.1. In this chapter, we consider only the active power and assume that the reactive power is adjusted accordingly by, for example, some turbine-level control loops, so that a constant power factor is always maintained. With this assumption, we will mostly omit the term "active" in the sequel. In addition, with the assumption, the approximate model for each wind turbine i is given by

$$\dot{P}_i(t) = -\frac{1}{\tau_i} P_i(t) + \frac{1}{\tau_i} \varphi_i(P_{d,i}(t), V_{w,i}(t)) + \gamma_i (V_{w,i}(t) - \mu_{w,i}(t)), \tag{5.3}$$

where $P_i(t) \in \mathbb{R}$ is the turbine power output, $P_{d,i}(t) \geq 0$ is the desired power, $\mu_{w,i}(t)$ may be seen as short-term averages of $V_{w,i}(t)$ given by (4.8), φ_i is a static nonlinear function, $\tau_i > 0$ is the (dominant) time constant, and $\gamma_i \geq 0$ is a scalar gain.

Remark 5.1. Note that there is a notational difference between (4.8)–(4.11) and (5.3): because (4.8)–(4.11) consider only *one* turbine but both *active* and *reactive* powers, there is no need to index the turbine, and the subscripts 1 and 2 in (4.8)–(4.11) represent the active and reactive powers, respectively. In contrast, because (5.3) applies to *every* turbine i but considers only the *active* power, there is a need to index each turbine with a subscript i but no need to distinguish between the active and reactive powers.

Although the WTCS model (5.3) is quite simple, it is possible to further simplify it in two ways as follows: first, given that $\mu_{w,i}(t)$ in (5.3) and $\bar{V}_{w,i}(t)$ in (5.1) play similar roles as short-term averages of $V_{w,i}(t)$, we view them as being the same quantity, i.e., $\mu_{w,i}(t) \equiv \bar{V}_{w,i}(t)$, so that $V_{w,i}(t) - \mu_{w,i}(t)$ in (5.3) may be replaced by $\tilde{V}_{w,i}(t)$ in (5.1). This replacement means that the wind speed model of Section 5.2.1, instead of the $\mu_{w,i}(t)$ dynamics (4.8), is used to define the rightmost term of (5.3). Second, as it turns out, the static nonlinear function $\varphi_i(P_{d,i}, V_{w,i})$ in (5.3) can be accurately approximated by a saturation function of $P_{d,i}$ with an upper limit of $\alpha_i V_{w,i}^3$ and a lower limit of 0, i.e.,

$$\varphi_i(P_{d,i}, V_{w,i}) \approx \operatorname{sat}_0^{\alpha_i V_{w,i}^3}(P_{d,i}), \quad \forall\, (P_{d,i},\, V_{w,i}),$$

where $\operatorname{sat}_a^b(x) \triangleq \max\{\min\{x, b\}, a\}$, and $\alpha_i > 0$ is meant to be a unit conversion factor. The upper limit of $\alpha_i V_{w,i}^3$ is motivated by the empirically observed, cubic

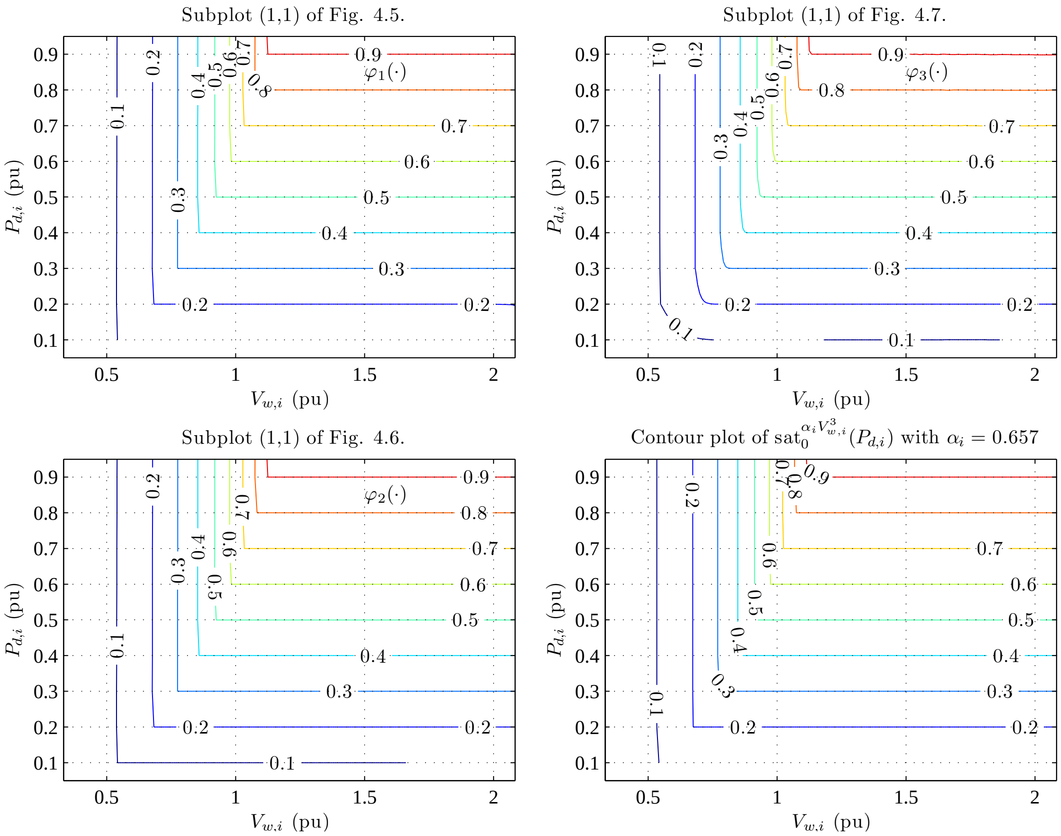
Subplot (1,1) of Fig. 4.5.

Subplot (1,1) of Fig. 4.7.

Subplot (1,1) of Fig. 4.6.

Contour plot of $\mathrm{sat}_0^{\alpha_i V_{w,i}^3}(P_{d,i})$ with $\alpha_i = 0.657$

Figure 5.3: Comparison between the contour plots of the functions φ_i from Subplot (1,1) of Figures 4.4–4.6 and the contour plot of $\mathrm{sat}_0^{\alpha_i V_{w,i}^3}$ with $\alpha_i = 0.657$ shows that the latter is an excellent approximate of the former.

relationship between wind speed and wind power, whereas the lower limit of 0 is due to power output being nonnegative in normal operating regimes. Figure 5.3 shows that this approximation is indeed highly accurate for three analytical WTCS models from the literature (see Section 4.4 for more details), and we believe that majority of well-designed WTCSs available today exhibit similar attributes. As a result, the function $\varphi_i(P_{d,i}, V_{w,i})$ in (5.3) may be replaced by the function $\mathrm{sat}_0^{\alpha_i V_{w,i}^3}(P_{d,i})$.

With the above two modifications to (5.3), we obtain a further simplified model, given by

$$\dot{P}_i(t) = -\frac{1}{\tau_i}P_i(t) + \frac{1}{\tau_i}\,\mathrm{sat}_0^{\alpha_i V_{w,i}^3(t)}(P_{d,i}(t)) + \gamma_i \tilde{V}_{w,i}(t), \tag{5.4}$$

which will be used in all subsequent WFC design and analysis. We note that the WTCS model (5.4) is not without limitations. Because of its high simplicity, it neglects details of the electrical dynamics of the wind turbine, as well as its flexible modes, and captures only its first-order, dominant transient behavior. Nevertheless, the model is simple and makes physical sense: for example, when the wind is strong enough, i.e., $\alpha_i V_{w,i}^3 > P_{d,i}$, saturation does not come into play, so that P_i will track $P_{d,i}$, causing the wind turbine to operate in the PR mode. Otherwise, P_i will track $\alpha_i V_{w,i}^3$, causing it to operate in the MPT mode. Also notice that $\gamma_i \tilde{V}_{w,i}$ enables fast fluctuations in $V_{w,i}$ to induce fluctuations in P_i, making the WTCS dynamics more realistic. Finally, note that (5.4) describes the internal details of each WTCS i block in Figure 5.1 and is also represented in the bottom portion of Figure 5.2.

5.2.3 Problem Formulation

Given the above wind speed model (5.1) and (5.2) and the wind turbine control system model (5.4) or, equivalently, Figure 5.2, the problem addressed in this chapter is to design a wind farm controller by adjusting the $P_{d,i}(t)$'s based on feedbacks of the $P_i(t)$'s and estimates of the $V_{w,i}(t)$'s, so that the wind farm power output $P_{wf}(t)$ closely tracks some desired, possibly time-varying reference $P_{d,wf}(t)$ from the grid operator and, at the same time, is as smooth as possible. The controller may use values of the turbine-dependent parameters (i.e., α_i's, τ_i's, and γ_i's) along with N. Moreover, the controller may use $P_{d,wf}(t)$ including its future values, as well as $P_i(t)$'s (and, thus, $P_{wf}(t)$ since $P_{wf}(t) =$

$\sum_{i=1}^{N} P_i(t)$) as feedback. Although it should not rely on the wind information (i.e., $V_{w,i}(t)$'s, $\bar{V}_{w,i}(t)$'s, $\tilde{V}_{w,i}(t)$'s, $w(t)$'s, N_w, W, $G_w(s)$), the controller may use some crude estimates of $V_{w,i}(t)$'s, which is not an unreasonable assumption.

5.3 Wind Farm Controller Framework

In this and the next two sections, we develop a WFC that addresses the aforementioned problem. This section is intended to describe the high-level rationale behind the WFC architecture and introduce its block diagram representation, while the next two are intended to provide low-level details.

5.3.1 Rationale Behind the Controller Architecture

To begin describing the rationale, recall from Section 5.2.3 that the WFC has two goals to achieve: (i) make the wind farm power output $P_{wf}(t)$ closely track a desired reference $P_{d,wf}(t)$, and (ii) make $P_{wf}(t)$ as smooth as possible, despite the fast wind fluctuations.

Observe from Figure 5.1 that $P_{wf}(t) = \sum_{i=1}^{N} P_i(t)$, so that goal (i) may be restated as

$$\sum_{i=1}^{N} P_i(t) = P_{d,wf}(t). \tag{5.5}$$

Imagine, for a moment, that we may freely specify the values of the N wind turbine power outputs $P_1(t), \ldots, P_N(t)$ in (5.5). Then, (5.5) represents an equality constant, the satisfaction of which leaves us with $N-1$ degrees of freedom, which are abundant given that N is usually large in a wind farm. Obviously, there are two opposing ways to handle such freedom: one may simply ignore it and choose, say, $P_i(t) = \frac{1}{N} P_{d,wf}(t)$ $\forall i \in \{1, 2, \ldots, N\}$ (i.e., uniformly distribute $P_{d,wf}(t)$ to every turbine), or one may opportunistically select $P_1(t), \ldots, P_N(t)$ to meet some secondary goals, in addition to satisfying (5.5). The former is clearly undesirable as it leads to a waste of such freedom, whereas the latter suggests that meaningful secondary goals must be defined.

To this end, we make three observations. First, note from Figure 5.1 that it is the inputs $P_{d,i}(t)$'s of the WTCSs, rather than the outputs $P_i(t)$'s, which may be freely specified. Moreover, dramatic jumps in the $P_{d,i}(t)$'s may lead to rapid changes in the electrical and mechanical turbine states, possibly exciting the high frequency unmodeled turbine dynamics and/or causing undesirable vibrations. Second, note that although wind speeds are, in general, difficult to predict—especially their fast, deviation-from-average components—, their slow, average components do exhibit predictable trends, at least for several minutes and even up to a few hours. Third, note that several-hours-ahead, future values of the desired reference $P_{d,wf}(t)$ are typically available from the grid operator as part of its power system planning.

The above three observations have a series of implications. First, they suggest that the $P_{d,i}(t)$'s may be determined by solving an optimization problem, in which the cost function is a sum of a tracking performance term (motivated by goal (i)) and a control effort term (motivated by the first observation), taken over a finite horizon into the future (motivated by the second and third observations). Given that the forecast of the wind speeds and the desired reference may be revised for better accuracy as time elapses, repeatedly solving the said optimization problem over a receding or moving horizon and applying only the initial portion of the optimal solution $P_{d,i}(t)$'s yield a strategy that incorporates not only the three observations toward achieving goal (i), but also the possibility of revised forecast. As it turns out, this is precisely the philosophy of *model predictive control* [87]. Notice that while the forecast of the desired reference is readily available from the grid operator, the forecast of the wind speeds may not be. Thus, an additional block within the model predictive controller is needed to provide such a functionality.

Up to this point in the development, we have constructed a model predictive controller, which computes the desired power trajectories $P_{d,1}(t), \ldots, P_{d,N}(t)$ that drive the N WTCSs. Although the model predictive controller is well-justified (see the above paragraphs), it suffers from an inherent drawback stemming from the following two factors: first, as was mentioned earlier, it is difficult to accurately predict the fast fluctuating components of the wind speeds. Thus, it is not reasonable to expect the model predictive controller to have access to accurate, high-resolution wind speed forecast over a long period of time. Second, it is well-known that one of the general limitations facing model predictive control is the need to solve optimization problems of potentially very high dimension. In the context of wind farms, this limitation is particularly pronounced due to the large number of turbines, i.e., large N. These two factors collectively prevent the sampling period of a discrete-time model typically used in model predictive control from being small. As a result, the model predictive controller is well-suited to deal with the tracking performance only on a longer timescale, i.e., goal (i), and not on a shorter one, i.e., goal (ii) or, equivalently, the smoothness of the wind farm power output. This represents the inherent drawback of the model predictive controller. As another drawback, model predictive strategies in general is open loop, relying heavily on the assumption that the WTCS model is accurate.

One way to alleviate the drawbacks is to insert, at the point where the $P_{d,i}(t)$'s enter the WTCS models (see Figure 5.1 or 5.2), a *feedback controller* that uses the computed $P_{d,i}(t)$'s (which we will denote as $P_{d,i}^*(t)$'s) and the feedbacks $P_i(t)$'s to calculate the corrected $P_{d,i}(t)$'s, which actually enter the WTCS models. This feedback controller, whose primary aim is to attain goal (ii), sits on the *inner loop* and operates on a shorter timescale compared to the model predictive controller, which sits on the *outer loop.* Although there are many possible choices for this feedback controller, in this chapter we let it be a fully decentralized bank of *proportional controllers* due to their simplicity in both design and analysis. (We note that although not pursued here, extension to more sophisticated controllers is possible.) Since it is well-known from classical control that proportional controllers generally yield non-zero steady-state errors, we precede each proportional controller with an appropriately chosen *feedforward gain* to eliminate such errors. Moreover, we further precede each feedforward gain with a *reference model* which transforms the $P_{d,i}^*(t)$'s into the corresponding references (which we will denote as $P_i^*(t)$'s).

As was mentioned, the proportional controller is intended to deal with the smoothness of the wind farm power output, i.e., goal (ii). Thanks to linearization and to stochastic linear systems theory, one could analytically express the smoothness of the wind farm power output, defined as its steady-state variance, in terms of the proportional controller gains and the wind speed parameters. It follows that for any given set of wind speed parameters, one could, in principle, choose the proportional controller gains to optimize the smoothness, leading to goal (ii). There is, however, a caveat: the wind speed parameters are not readily available. Hence, an additional block is needed to provide estimates of such parameters. Finally, since characteristics of the wind speeds—including their directions and statistical properties— change over time, so would the values of the wind speed parameters. Therefore, this additional block should continuously update their estimates of the wind speed

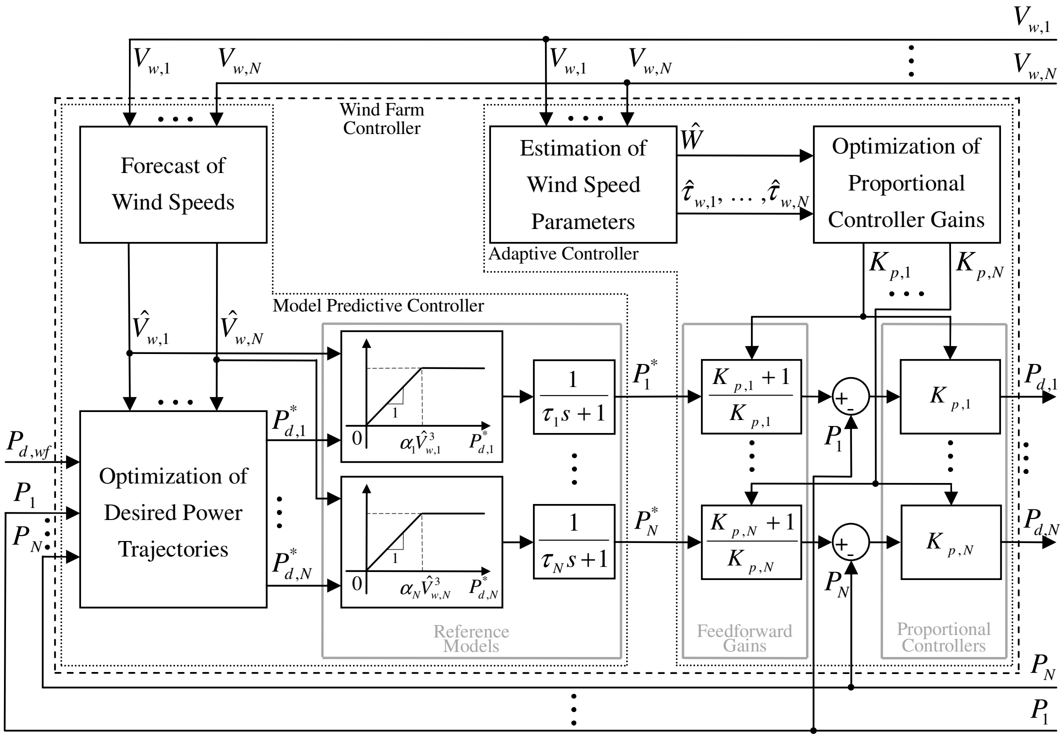

Figure 5.4: Block diagram of the wind farm controller (WFC), comprising a model predictive controller on the outer loop and an adaptive controller on the inner loop.

parameters in real-time, while the proportional gains should be continuously and accordingly tuned in real-time as well. For those who are familiar with *adaptive control* [88], this idea is precisely what underlies the so-called *self-tuning regulator*. Consequently, we refer to this overall scheme on the inner loop as an adaptive controller.

This completes the description of the rationale behind the WFC architecture.

5.3.2 Block Diagram of the Controller

As it follows from the above, the WFC consists of two control loops: an outer loop and an inner one, the block diagram of which is shown in Figure 5.4.

The outer loop implements the model predictive controller, which determines the optimal power trajectories for use by the inner loop, so that the wind farm power output tracks the desired reference as closely as possible. The inner loop, on the other hand, implements the adaptive controller, which calculates the optimal controller parameters so that the wind farm power output is made as smooth as possible.

The model predictive controller consists of three blocks: *Forecast of Wind Speeds*, *Optimization of Desired Power Trajectories*, and *Reference Models*, as shown in the left portion of Figure 5.4. Based on crude estimates of $V_{w,i}(t)$'s, the *Forecast of Wind Speeds* block produces $\hat{V}_{w,i}(t)$'s, forecasts of the future wind speed at each WTCS. The *Optimization of Desired Power Trajectories* block accepts the forecast of power command $P_{d,wf}(t)$ from the grid operator, the forecasts of wind speeds $\hat{V}_{w,i}(t)$'s from the *Forecast of Wind Speeds* block, and the feedbacks of power outputs $P_i(t)$'s from each wind turbine, and generates the optimal desired power trajectories $P^*_{d,i}(t)$'s. Finally, the *Reference Models* block converts $P^*_{d,i}(t)$'s into the optimal power outputs $P^*_i(t)$'s, which enter the adaptive controller described next.

The adaptive controller consists of four blocks: *Estimation of Wind Speed Parameters*, *Optimization of Proportional Controller Gains*, *Feedforward Gains*, and *Proportional Controllers*, as shown in the right portion of Figure 5.4. Based on measurements of the wind speeds $V_{w,i}(t)$'s, the *Estimation of Wind Speed Parameters* block produces an estimate of the covariance matrix $\hat{W}$, and estimates of the time constants $\hat{\tau}_{w,i}(t)$'s, the role of which will be made clear shortly. Based on such information, the *Optimization of Proportional Controller Gains* block generates the optimal controller gains $K_{p,i}$'s. The optimal controller gains are then used to construct the *Feedforward Gains* block and the *Proportional Controllers* block. The *Feedforward Gains* block is intended to amplify the optimal turbine power outputs $P_i^*(t)$'s from the outer loop, so that the steady-state errors are zero. The *Proportional Controllers* block, on the other hand, is intended to use feedbacks of the $P_i(t)$'s to compute the $P_{d,i}(t)$'s, so that the $P_i(t)$'s would track the $P_i^*(t)$'s. Finally, the $P_{d,i}(t)$'s represent the output of the WFC or, equivalently, the inputs to the WTCSs.

Detailed description of both the model predictive controller and the adaptive controller will be given in Sections 5.4 and 5.5, respectively.

5.4 Model Predictive Control Design

As was outlined in Section 5.3, the model predictive controller, which represents the outer loop of the WFC, is made up of three blocks, namely, the *Forecast of Wind Speeds*, *Optimization of Desired Power Trajectories*, and *Reference Models* blocks. In this section, we describe in details each of these blocks.

5.4.1 Forecast of Wind Speeds

The current literature offers a large body of work on wind speed forecasting, developed by researchers across a number of disciplines. See [89–91] for state-of-the-art overviews and the references therein. A variety of techniques have been adopted in these publications, leading to many different wind speed forecasting models for different purposes, including, for example, the autoregressive models proposed in [89]. Because wind speed forecasting has been well-studied and because the topic is not within the scope of this research, in this chapter we assume that one of the available models is used by the *Forecast* *of Wind Speeds* block to provide wind speed forecasts $\hat{V}_{w,1}(t), \ldots, \hat{V}_{w,N}(t)$ based on possibly crude measurements of the wind speeds $V_{w,1}(t), \ldots, V_{w,N}(t)$.

5.4.2 Optimization of Desired Power Trajectories

In this subsection, we describe the *Optimization of Desired Power Trajectories* block of Figure 5.4 by introducing a discrete-time model, formulating a tracking performance optimization problem, and solving the problem to obtain the optimal desired power trajectories.

Discrete-Time Model

Consider the WTCS model given by (5.4). To utilize this model in the model predictive control design, we make two slight modifications to it. For each WTCS i, since the actual wind speed $V_{w,i}(t)$ may not be known but its forecast $\hat{V}_{w,i}(t)$ from Section 5.4.1 is, we first replace $V_{w,i}(t)$ in (5.4) by $\hat{V}_{w,i}(t)$. Moreover, since the mean of the fast component $\tilde{V}_{w,i}(t)$ from (5.2) is zero and since the model predictive controller is intended to operate on a longer timescale, we further disregard $\tilde{V}_{w,i}(t)$ in (5.4). With these two modifications to (5.4), we obtain

$$\dot{P}_i(t) = -\frac{1}{\tau_i} P_i(t) + \frac{1}{\tau_i} \operatorname{sat}_0^{\alpha_i \hat{V}_{w,i}^3(t)}(P_{d,i}(t)). \tag{5.6}$$

Although it is possible to formulate and solve a continuous-time optimal control problem based on the continuous-time model (5.6), doing so in a discrete-time setting is considerably simpler. To this end, we assume that both $\hat{V}_{w,i}(t)$ and $P_{d,i}(t)$ are staircase signals with staircase duration of $T_s > 0$, so that they may be written as $\hat{V}_{w,i}[k]$ and $P_{d,i}[k]$ (with angle brackets), where $k = 0, 1, 2, \ldots$ denotes discrete time instant and $\hat{V}_{w,i}[k] = \hat{V}_{w,i}(t)$ and

$P_{d,i}[k] = P_{d,i}(t)$ for $t \in [kT_s, (k+1)T_s)$. With this assumption and with $P_i[k]$ representing the value of $P_i(t)$ at "sampling instant" $t = kT_s$, the continuous-time model (5.6) may be discretized as if there is a zero-order hold with a sampling period T_s, resulting in a discrete-time linear model

$$P_i[k+1] = a_i P_i[k] + (1 - a_i) P_{d,i}[k], \tag{5.7}$$

where the parameter a_i is given by $a_i = e^{-\frac{T_s}{\tau_i}} \in (0,1)$ and the input $P_{d,i}[k]$ satisfies

$$0 \leq P_{d,i}[k] \leq \alpha_i \hat{V}_{w,i}^3[k]. \tag{5.8}$$

Note that with (5.8), the saturation function appearing in (5.6) does not show up in (5.7).

For convenience, let us introduce the following notations:

$$\begin{aligned}
\mathbf{P}_i^{k_0} &= \begin{bmatrix} P_i[k_0] & P_i[k_0+1] & \cdots & P_i[k_0+K-1] \end{bmatrix}^T, \\
\mathbf{P}_{d,i}^{k_0} &= \begin{bmatrix} P_{d,i}[k_0] & P_{d,i}[k_0+1] & \cdots & P_{d,i}[k_0+K-1] \end{bmatrix}^T, \\
\mathbf{P}_{d,wf}^{k_0} &= \begin{bmatrix} P_{d,wf}[k_0] & P_{d,wf}[k_0+1] & \cdots & P_{d,wf}[k_0+K-1] \end{bmatrix}^T, \\
\mathbf{P}_d^{k_0} &= \begin{bmatrix} (\mathbf{P}_{d,1}^{k_0})^T & (\mathbf{P}_{d,2}^{k_0})^T & \cdots & (\mathbf{P}_{d,N}^{k_0})^T \end{bmatrix}^T,
\end{aligned}$$

where K is a positive integer. With these notations, (5.7) can be written in matrix form as follows:

$$\begin{aligned}
\begin{bmatrix} P_i[k_0+1] \\ P_i[k_0+2] \\ \vdots \\ P_i[k_0+K] \end{bmatrix} &= \begin{bmatrix} (1-a_i) & 0 & \cdots & 0 \\ a_i(1-a_i) & (1-a_i) & \ddots & \vdots \\ \vdots & \ddots & \ddots & 0 \\ a_i^{K-1}(1-a_i) & \cdots & a_i(1-a_i) & (1-a_i) \end{bmatrix} \begin{bmatrix} P_{d,i}[k_0] \\ P_{d,i}[k_0+1] \\ \vdots \\ P_{d,i}[k_0+K-1] \end{bmatrix} \\
&\quad + \begin{bmatrix} a_i \\ a_i^2 \\ \vdots \\ a_i^K \end{bmatrix} P_i[k_0]
\end{aligned}$$

$$\begin{aligned}\mathbf{P}_i^{k_0+1} &= (1-a_i)\underbrace{\begin{bmatrix} 1 & 0 & \dots & 0 \\ a_i & 1 & \ddots & \vdots \\ \vdots & \ddots & \ddots & 0 \\ a_i^{K-1} & \dots & a_i & 1 \end{bmatrix}}_{L_i}\mathbf{P}_{d,i}^{k_0} + a_i\underbrace{\begin{bmatrix} 1 \\ a_i \\ \vdots \\ a_i^{K-1} \end{bmatrix}}_{v_i} P_i[k_0] \\ &= (1-a_i)L_i\mathbf{P}_{d,i}^{k_0} + a_i v_i P_i[k_0], \end{aligned} \tag{5.9}$$

where L_i and v_i are as labeled in (5.9). It follows from (5.9) that

$$\begin{bmatrix} \mathbf{P}_1^{k_0+1} \\ \mathbf{P}_2^{k_0+1} \\ \vdots \\ \mathbf{P}_N^{k_0+1} \end{bmatrix} = \begin{bmatrix} (1-a_1)L_1 & 0 & \dots & 0 \\ 0 & (1-a_2)L_2 & \ddots & \vdots \\ \vdots & \ddots & \ddots & 0 \\ 0 & \dots & 0 & (1-a_N)L_N \end{bmatrix} \mathbf{P}_d^{k_0} + \begin{bmatrix} a_1 v_1 P_1[k_0] \\ a_2 v_2 P_2[k_0] \\ \vdots \\ a_N v_N P_N[k_0] \end{bmatrix}. \tag{5.10}$$

Equation (5.10) will be used shortly.

Tracking Performance Optimization

Having derived the discrete-time WTCS model (5.7), we consider next the following optimization problem: Given an initial time instant $k_0 \geq 1$, a finite horizon $K \geq 1$, forecast of the desired wind farm power output $P_{d,wf}[k]$ for $k = k_0, k_0+1, \dots, k_0+K$, forecast of the wind speeds $\hat{V}_{w,i}[k]$ for $k = k_0, k_0+1, \dots, k_0+K-1$, the initial power outputs $P_i[k_0]$ for $i = 1, 2, \dots, N$, and initial desired powers $P_{d,i}[k_0-1]$ for $i = 1, 2, \dots, N$, find $\mathbf{P}_d^{k_0}$ that minimizes the cost function

$$\begin{aligned} J_1 = &\sum_{k=k_0}^{k_0+K} \eta(k)(\sum_{i=1}^{N} P_i[k] - P_{d,wf}[k])^2 + \sum_{k=k_0}^{k_0+K-1} \sum_{i=1}^{N} \mu_i(k)(P_{d,i}[k] - P_{d,i}[k-1])^2 \\ &+ \sum_{k=k_0}^{k_0+K-1} \sum_{i=1}^{N} \nu_i(k) P_{d,i}^2[k] \end{aligned} \tag{5.11}$$

subject to (5.7) and (5.8) for $k = k_0, k_0+1, \dots, k_0+K-1$ and for $i = 1, 2, \dots, N$. To see the interpretation of this dynamic, inequality-constrained optimization problem, notice that the optimization variable $\mathbf{P}_d^{k_0}$ is a NK-dimensional vector that stacks $P_{d,i}[k]$ for $k = k_0, k_0+1, \ldots, k_0+K-1$ and for $i = 1, 2, \ldots, N$. Also note that the cost function J_1 contains three terms, where the first term is the receding horizon sum of the square of the tracking errors and, thus, reflects the tracking performance, whereas the second and third terms are the receding horizon sum of the square of the control variations and magnitudes and, hence, reflect the control effort. In addition, the weights $\eta(k)$'s, $\mu_i(k)$'s, and $\nu_i(k)$'s are positive constants, which describe the relative importance of the summands at various time instants for various wind turbines. Therefore, solving the optimization problem (5.11) for the optimal $\mathbf{P}_d^{k_0}$ may be regarded as *finding the desired power trajectories, which optimize a possibly time-varying weighted combination of the tracking performance and control effort.*

The dynamic optimization problem (5.11) may be transformed into a static one using (5.10). To see this, observe that the first term of J_1 in (5.11) may be written as

$$\begin{aligned}
&\sum_{k=k_0}^{k_0+K} \eta(k)(\sum_{i=1}^{N} P_i[k] - P_{d,wf}[k])^2 \\
&= \sum_{k=k_0+1}^{k_0+K} \eta(k)(\sum_{i=1}^{N} P_i[k] - P_{d,wf}[k])^2 + \eta(k_0)(\sum_{i=1}^{N} P_i[k_0] - P_{d,wf}[k_0])^2 \\
&= \sum_{k=k_0+1}^{k_0+K} \eta(k)(\sum_{i=1}^{N} P_i[k])^2 - 2\sum_{k=k_0+1}^{k_0+K} \eta(k)\sum_{i=1}^{N} P_i[k]P_{d,wf}[k] + \sum_{k=k_0+1}^{k_0+K} \eta(k)P_{d,wf}^2[k] \\
&\quad + \eta(k_0)(\sum_{i=1}^{N} P_i[k_0] - P_{d,wf}[k_0])^2 \\
&= \begin{bmatrix} \mathbf{P}_1^{k_0+1} \\ \mathbf{P}_2^{k_0+1} \\ \vdots \\ \mathbf{P}_N^{k_0+1} \end{bmatrix}^T \begin{bmatrix} H^{k_0+1} & H^{k_0+1} & \ldots & H^{k_0+1} \\ H^{k_0+1} & H^{k_0+1} & \ldots & H^{k_0+1} \\ \vdots & \vdots & \ddots & \vdots \\ H^{k_0+1} & H^{k_0+1} & \ldots & H^{k_0+1} \end{bmatrix} \begin{bmatrix} \mathbf{P}_1^{k_0+1} \\ \mathbf{P}_2^{k_0+1} \\ \vdots \\ \mathbf{P}_N^{k_0+1} \end{bmatrix}
\end{aligned}$$

$$
-2\begin{bmatrix}\mathbf{P}_{d,wf}^{k_0+1}\\ \mathbf{P}_{d,wf}^{k_0+1}\\ \vdots\\ \mathbf{P}_{d,wf}^{k_0+1}\end{bmatrix}^T\begin{bmatrix}H^{k_0+1} & 0 & \dots & 0\\ 0 & H^{k_0+1} & \ddots & \vdots\\ \vdots & \ddots & \ddots & 0\\ 0 & \dots & 0 & H^{k_0+1}\end{bmatrix}\begin{bmatrix}\mathbf{P}_1^{k_0+1}\\ \mathbf{P}_2^{k_0+1}\\ \vdots\\ \mathbf{P}_N^{k_0+1}\end{bmatrix}
$$

$$
+\sum_{k=k_0+1}^{k_0+K}\eta(k)P_{d,wf}^2[k]+\eta(k_0)(\sum_{i=1}^{N}P_i[k_0]-P_{d,wf}[k_0])^2, \tag{5.12}
$$

where $H^{k_0+1}=\operatorname{diag}(\eta(k_0+1),\eta(k_0+2),\dots,\eta(k_0+K))$. Substituting (5.10) into (5.12) yields

$$
\sum_{k=k_0}^{k_0+K}\eta(k)(\sum_{i=1}^{N}P_i[k]-P_{d,wf}[k])^2
$$

$$
=(\mathbf{P}_d^{k_0})^T\begin{bmatrix}(1-a_1)(1-a_1)L_1^TH^{k_0+1}L_1 & \dots & (1-a_1)(1-a_N)L_1^TH^{k_0+1}L_N\\ \vdots & \ddots & \vdots\\ (1-a_N)(1-a_1)L_N^TH^{k_0+1}L_1 & \dots & (1-a_N)(1-a_N)L_N^TH^{k_0+1}L_N\end{bmatrix}\mathbf{P}_d^{k_0}
$$

$$
+2\begin{bmatrix}a_1v_1P_1[k_0]\\ \vdots\\ a_Nv_NP_N[k_0]\end{bmatrix}^T\begin{bmatrix}(1-a_1)H^{k_0+1}L_1 & \dots & (1-a_N)H^{k_0+1}L_N\\ \vdots & \ddots & \vdots\\ (1-a_1)H^{k_0+1}L_1 & \dots & (1-a_N)H^{k_0+1}L_N\end{bmatrix}\mathbf{P}_d^{k_0}
$$

$$
-2\begin{bmatrix}\mathbf{P}_{d,wf}^{k_0+1}\\ \vdots\\ \mathbf{P}_{d,wf}^{k_0+1}\end{bmatrix}^T\begin{bmatrix}(1-a_1)H^{k_0+1}L_1 & & 0\\ & \ddots & \\ 0 & & (1-a_N)H^{k_0+1}L_N\end{bmatrix}\mathbf{P}_d^{k_0}
$$

$$
-2\sum_{i=1}^{N}a_iP_i[k_0](\mathbf{P}_{d,wf}^{k_0+1})^TH^{k_0+1}v_i+\sum_{i=1}^{N}\sum_{j=1}^{N}a_ia_jP_i[k_0]P_j[k_0]v_i^TH^{k_0+1}v_j
$$

$$
+\sum_{k=k_0+1}^{k_0+K}\eta(k)P_{d,wf}^2[k]+\eta(k_0)(\sum_{i=1}^{N}P_i[k_0]-P_{d,wf}[k_0])^2. \tag{5.13}
$$

Likewise, notice that the second and third terms of J_1 may be expressed as

$$
\sum_{k=k_0}^{k_0+K-1}\sum_{i=1}^{N}\mu_i(k)(P_{d,i}[k]-P_{d,i}[k-1])^2+\sum_{k=k_0}^{k_0+K-1}\sum_{i=1}^{N}\nu_i(k)P_{d,i}^2[k]
$$

$$
=(\mathbf{P}_d^{k_0})^T\begin{bmatrix}U_1+V_1 & 0 & \dots & 0\\ 0 & U_2+V_2 & \ddots & \vdots\\ \vdots & \ddots & \ddots & 0\\ 0 & \dots & 0 & U_N+V_N\end{bmatrix}\mathbf{P}_d^{k_0}
$$

$$- 2\Big(\begin{bmatrix} \mu_1(k_0)P_{d,1}[k_0-1] \\ \mu_2(k_0)P_{d,2}[k_0-1] \\ \vdots \\ \mu_N(k_0)P_{d,N}[k_0-1] \end{bmatrix} \otimes \begin{bmatrix} 1 \\ 0 \\ \vdots \\ 0 \end{bmatrix} \Big)^T \mathbf{P}_d^{k_0} + \sum_{i=1}^{N} \mu_i(k_0) P_{d,i}^2[k_0-1], \quad (5.14)$$

where $\otimes$ denotes the Kronecker product, $U_i = U_i^T > 0$ is given by

$$\begin{bmatrix} \mu_i(k_0)+\mu_i(k_0+1) & -\mu_i(k_0+1) & 0 & 0 & \cdots & 0 \\ -\mu_i(k_0+1) & \mu_i(k_0+1)+\mu_i(k_0+2) & -\mu_i(k_0+2) & 0 & & 0 \\ 0 & -\mu_i(k_0+2) & \mu_i(k_0+2)+\mu_i(k_0+3) & \ddots & \ddots & \vdots \\ 0 & 0 & \ddots & \ddots & -\mu_i(k_0+K-2) & 0 \\ \vdots & & \ddots & -\mu_i(k_0+K-2) & \mu_i(k_0+K-2)+\mu_i(k_0+K-1) & -\mu_i(k_0+K-1) \\ 0 & 0 & \cdots & 0 & -\mu_i(k_0+K-1) & \mu_i(k_0+K-1) \end{bmatrix},$$

and $V_i = V_i^T > 0$ is given by

$$V_i = \operatorname{diag}(\nu_i(k_0), \nu_i(k_0+1), \ldots, \nu_i(k_0+K-1)).$$

(To understand the structure of U_i, note that by ignoring the constant $\mu_i(k_0)$ on its first row and first column, U_i may be regarded as a weighted Laplacian matrix of an undirected path graph.) Expressions (5.13) and (5.14) together suggest that the cost function J_1 is a quadratic function of the optimization variable $\mathbf{P}_d^{k_0}$, i.e.,

$$J_1 = (\mathbf{P}_d^{k_0})^T S \mathbf{P}_d^{k_0} + b^T \mathbf{P}_d^{k_0} + c$$

for some $S \in \mathbb{R}^{NK \times NK}$, $b \in \mathbb{R}^{NK}$, and $c \in \mathbb{R}$, which can be determined from (5.13) and (5.14). A closer look at these expressions also reveals that $S = S^T > 0$. Thus, by leveraging the dynamics (5.10), the dynamic optimization problem (5.11) may be converted into a static, convex quadratic optimization problem with "box" constraints, the latter due to (5.8).

Optimal Desired Power Trajectories

That the cost function J_1 is strongly convex and the constraint is compact and convex imply that there always exists a unique solution $\mathbf{P}_d^{k_0}$ to the optimization problem. Unfortunately however, such a solution cannot, in general, be analytically obtained [92]. Nevertheless, effective and reliable numerical algorithms, capable of solving the optimization problem in a few tens of seconds when its dimension NK is up to several thousands, are currently available (e.g., the interior point methods [92]). Hence, in what follows we will assume that one such numerical algorithm is in place.

Thus far, we have presented an optimization-based approach for computing, at any given time instant $k = k_0$, the desired power trajectory $P_{d,i}[k]$ of every turbine $i \in \{1, 2, \ldots, N\}$ from that time instant to a later time instant $k = k_0 + K - 1$. The computation is carried out based on forecast of the wind speeds $\hat{V}_{w,1}[k], \ldots, \hat{V}_{w,N}[k]$ and forecast of the desired wind farm power output $P_{d,wf}[k]$ over the same time interval, i.e., from $k = k_0$ to $k = k_0 + K - 1$. Since forecast of the value of a signal at a certain time generally becomes more accurate as we draw closer to the given time, and since more accurate forecast generally translates into more meaningful desired power trajectories, it is conceivable that solving the optimization problem at each time instant using the latest available forecast and applying only the first step of the solution represent a sensible way to reap the benefit of revised forecast. This idea, which belongs to the realm of *model predictive control* [87], is particularly suitable here as forecast of both $\hat{V}_{w,1}[k], \ldots, \hat{V}_{w,N}[k]$ and $P_{d,wf}[k]$ usually becomes more accurate as time progresses.

Consequently, in the sequel we adopt a model predictive controller, which operates as follows: At each time instant $k_0 \geq 1$, the controller solves the optimization problem for $P_{d,i}[k]$ for $k = k_0, \ldots, k_0 + K - 1$ and for $i = 1, 2, \ldots, N$, but only applies $P_{d,i}[k_0]$ for $i = 1, 2, \ldots, N$ between time k_0 and $k_0 + 1$. Since the $P_{d,i}[k]$ that gets computed is not the same as the $P_{d,i}[k]$ that gets applied, to avoid confusion, we will denote the latter as $P^*_{d,i}[k]$.

Note that the above paragraph describes only the operation of the model predictive controller at each time instant $k_0 \geq 1$ but not its initialization at time instant 0. Examining the description, however, we can see that the only initial conditions that we need to assume are $P_{d,i}[0]$ and $P_i[0]$ for $i = 1, 2, \ldots, N$.

5.5 Adaptive Control Design

Having described the model predictive controller on the outer loop of the WFC, we now consider the adaptive controller, which sits on the inner loop and is made up of four blocks: the *Estimation of Wind Speed Parameters*, *Optimization of Proportional Controller Gains*, *Feedforward Gains*, and *Proportional Controllers* blocks. In this section, we describe in details each of these blocks.

5.5.1 Proportional Controllers and Feedforward Gains

As was mentioned in Section 5.3.1, due to the limitations of the model predictive controller, we insert a fully decentralized bank of proportional controllers between $P_i^*(t)$'s, the outputs of the model predictive controller, and $P_{d,i}(t)$'s, the inputs of the WTCSs. Moreover, to eliminate steady-state errors, we precede each proportional controller with a feedforward gain, as was shown in Figure 5.4. Therefore, $P_{d,i}(t)$ that enters each WTCS i can be written as

$$P_{d,i}(t) = K_{p,i}\Big(\frac{1 + K_{p,i}}{K_{p,i}} P_i^*(t) - P_i(t)\Big), \tag{5.15}$$

where $K_{p,i} > 0$ is the proportional controller gain. Equation (5.15) says that the difference between $P_i(t)$ and an appropriately scaled version of $P_i^*(t)$ is used to compute a "corrective" action $P_{d,i}(t)$ which drives each WTCS i.

5.5.2 Optimization of Proportional Controller Gains

In this subsection, we describe the *Optimization of Proportional Controller Gains* block of Figure 5.4 by introducing an augmented model, formulating a smoothness optimization problem, and solving the problem to obtain the optimal proportional controller gains $K_{p,i}$'s.

Augmented Model: Linearized Model plus Specific Wind Speed Model

Consider the model (5.2) which describes the fast wind speed components. To utilize this model in our design, we assume that $N_w = N$, so that the stationary, zero-mean white Gaussian random process $w(t)$ has N components, where each $w_i(t)$ is associated with WTCS i. Moreover, we let the generic transfer function matrix $G_w(s)$ take a specific form, i.e.,

$$G_w(s) = \operatorname{diag}\Big(\frac{1}{\tau_{w,1}s+1}, \frac{1}{\tau_{w,2}s+1}, \ldots, \frac{1}{\tau_{w,N}s+1}\Big), \tag{5.16}$$

where $\tau_{w,i} > 0$ represents the time constant. From (5.2) and (5.16), we obtain

$$\dot{\tilde{V}}_{w,i}(t) = -\frac{1}{\tau_{w,i}}\tilde{V}_{w,i}(t) + \frac{1}{\tau_{w,i}}w_i(t). \tag{5.17}$$

Thus, for each WTCS i, the fast wind speed component $\tilde{V}_{w,i}(t)$ is a zero-mean colored Gaussian random process driven by $w_i(t)$.

Next, consider the WTCS model given by (5.4). For simplicity, we assume that the saturation block does not come into play, and note that this assumption is not uncommon in control systems literature, as it simplifies the design and analysis while maintaining reasonable validity. With this assumption and by substituting (5.15) into (5.4), we obtain for each WTCS i

$$\dot{P}_i(t) = -\frac{1+K_{p,i}}{\tau_i}P_i(t) + \frac{1+K_{p,i}}{\tau_i}P_i^*(t) + \gamma_i\tilde{V}_{w,i}(t), \tag{5.18}$$

where $P_i^*(t)$ is relatively slow-varying, since the outer loop model predictive controller is running on a much longer timescale. Assuming that $P_i^*(t)$ is so slow that it can be regarded as constant, the system (5.18) without the "disturbance" $\tilde{V}_{w,i}(t)$ has a unique equilibrium point $P_{i,eq}$ given by

$$P_{i,eq} = P_i^*(t). \tag{5.19}$$

In addition, the steady-state value of $P_{d,i}(t)$ corresponding to this equilibrium point, denoted as $P_{d,i,eq}$, is given by

$$P_{d,i,eq} = P_i^*(t). \tag{5.20}$$

To obtain a linearized model about this equilibrium point, let us introduce

$$\Delta P_i(t) = P_i(t) - P_{i,eq}, \tag{5.21}$$

$$\Delta P_{d,i}(t) = P_{d,i}(t) - P_{d,i,eq}. \tag{5.22}$$

Note from (5.15) and (5.19)–(5.22) that

$$\Delta P_{d,i}(t) = -K_{p,i}\Delta P_i(t), \tag{5.23}$$

and from (5.18), (5.19), and (5.21) that

$$\Delta \dot{P}_i(t) = -\frac{1+K_{p,i}}{\tau_i}\Delta P_i(t) + \gamma_i \tilde{V}_{w,i}(t). \tag{5.24}$$

Combining (5.17) and (5.24), we obtain the following *augmented model* with state variables $(\tilde{V}_{w,i}(t), \Delta P_i(t))$ for each wind turbine i:

$$\begin{bmatrix} \dot{\tilde{V}}_{w,i}(t) \\ \Delta \dot{P}_i(t) \end{bmatrix} = \begin{bmatrix} -\frac{1}{\tau_{w,i}} & 0 \\ \gamma_i & -\frac{1+K_{p,i}}{\tau_i} \end{bmatrix} \begin{bmatrix} \tilde{V}_{w,i}(t) \\ \Delta P_i(t) \end{bmatrix} + \begin{bmatrix} \frac{1}{\tau_{w,i}} \\ 0 \end{bmatrix} w_i(t). \tag{5.25}$$

Since (5.25) applies to every wind turbine i, we can write the augmented model in matrix form as

$$\begin{bmatrix} \dot{\tilde{V}}_w(t) \\ \Delta \dot{P}(t) \end{bmatrix} = \underbrace{\begin{bmatrix} A_{11} & 0 \\ A_{21} & A_{22} \end{bmatrix}}_{A} \begin{bmatrix} \tilde{V}_w(t) \\ \Delta P(t) \end{bmatrix} + \underbrace{\begin{bmatrix} -A_{11} \\ 0 \end{bmatrix}}_{B} w(t), \tag{5.26}$$

where $A \in \mathbb{R}^{2N\times 2N}$ and $B \in \mathbb{R}^{2N\times N}$ are as labeled in (5.26), and

$$\begin{aligned}
\tilde{V}_w(t) &= \left[\tilde{V}_{w,1}(t)\ \tilde{V}_{w,2}(t)\ \cdots\ \tilde{V}_{w,N}(t)\right]^T, \\
\Delta P(t) &= \left[\Delta P_1(t)\ \Delta P_2(t)\ \cdots\ \Delta P_N(t)\right]^T, \\
A_{11} &= \operatorname{diag}\Big(-\frac{1}{\tau_{w,1}}, -\frac{1}{\tau_{w,2}}, \dots, -\frac{1}{\tau_{w,N}}\Big), \\
A_{21} &= \operatorname{diag}(\gamma_1, \gamma_2, \dots, \gamma_N), \\
A_{22} &= \operatorname{diag}\Big(-\frac{1+K_{p,1}}{\tau_1}, -\frac{1+K_{p,2}}{\tau_2}, \dots, -\frac{1+K_{p,N}}{\tau_N}\Big).
\end{aligned}$$

Note that since $\tau_{w,i} > 0$, $\tau_i > 0$, and $K_{p,i} > 0$, the system (5.26) or matrix A is asymptotically stable.

Smoothness Optimization

Having derived the augmented model (5.26), we consider next the following optimization problem: Given the positive definite covariance matrix W and time constants $\tau_{w,i} > 0$ for $i = 1, 2, \dots, N$, find the proportional controller gains $K_p = [K_{p,1}\ K_{p,2}\ \cdots\ K_{p,N}]^T$ that minimize the cost function

$$J_2 = \lim_{t\to\infty} E\{(\sum_{i=1}^{N} \Delta P_i(t))^2 + \sum_{i=1}^{N} \epsilon_i \Delta P_{d,i}^2(t)\}. \tag{5.27}$$

Note that the cost function J_2 contains two terms, where the first term (including the limit and expectation) represents the steady-state variance of the regulation error reflecting the smoothness of the wind farm power output, whereas the second term represents the sum of the steady-state variance of the control magnitudes reflecting the control effort. In addition, the weights ϵ_i's are positive constants, which describe the relative importance of the summands for various wind turbines. Therefore, solving the optimization problem (5.27) for the optimal K_p may be viewed as *finding the proportional gains that optimize a weighted combination of the smoothness and control effort.*

Substituting (5.23) into (5.27) yields

$$\begin{aligned} J_2 &= \lim_{t\to\infty} E\{(\sum_{i=1}^{N} \Delta P_i(t))^2 + \sum_{i=1}^{N} \epsilon_i K_{p,i}^2 \Delta P_i^2(t)\} \\ &= \lim_{t\to\infty} E\{\begin{bmatrix}\tilde{V}_w(t)^T & \Delta P(t)^T\end{bmatrix} \underbrace{\begin{bmatrix}0 & 0\\ 0 & Q_{22}\end{bmatrix}}_{Q} \begin{bmatrix}\tilde{V}_w(t)\\ \Delta P(t)\end{bmatrix}\}, \end{aligned} \tag{5.28}$$

where $Q \in \mathbb{R}^{2N\times 2N}$ is as labeled in (5.28) and $Q_{22} = Q_{22}^T > 0$ is given by

$$Q_{22} = \begin{bmatrix} 1+\epsilon_1 K_{p,1}^2 & 1 & \dots & 1 \\ 1 & 1+\epsilon_2 K_{p,2}^2 & \ddots & \vdots \\ \vdots & \ddots & \ddots & 1 \\ 1 & \dots & 1 & 1+\epsilon_N K_{p,N}^2 \end{bmatrix}.$$

From stochastic linear systems theory [93], we know that

$$J_2 = \mathrm{trace}(SQ), \tag{5.29}$$

where $S = S^T > 0$ is the unique solution of the Lyapunov equation

$$0 = AS + SA^T + BWB^T. \tag{5.30}$$

For convenience, let $S \in \mathbb{R}^{2N\times 2N}$ be partitioned as

$$S = \begin{bmatrix} S_1 & S_2 \\ S_2^T & S_3 \end{bmatrix},$$

where $S_1 = S_1^T \in \mathbb{R}^{N\times N}$, $S_2 \in \mathbb{R}^{N\times N}$, and $S_3 = S_3^T \in \mathbb{R}^{N\times N}$. With this partitioning and that of A and B from (5.26), we may rewrite (5.30) as

$$\begin{bmatrix} A_{11} & 0 \\ A_{21} & A_{22} \end{bmatrix} \begin{bmatrix} S_1 & S_2 \\ S_2^T & S_3 \end{bmatrix} + \begin{bmatrix} S_1 & S_2 \\ S_2^T & S_3 \end{bmatrix} \begin{bmatrix} A_{11} & A_{21} \\ 0 & A_{22} \end{bmatrix} + \begin{bmatrix} A_{11} W A_{11} & 0 \\ 0 & 0 \end{bmatrix} = 0$$

and, thus, as

$$\begin{aligned} &\begin{bmatrix} A_{11} S_1 & A_{11} S_2 \\ A_{21} S_1 + A_{22} S_2^T & A_{21} S_2 + A_{22} S_3 \end{bmatrix} + \begin{bmatrix} S_1 A_{11} & S_1 A_{21} + S_2 A_{22} \\ S_2^T A_{11} & S_2^T A_{21} + S_3 A_{22} \end{bmatrix} \\ &+ \begin{bmatrix} A_{11} W A_{11} & 0 \\ 0 & 0 \end{bmatrix} = 0. \end{aligned}$$

Since A_{11} is asymptotically stable, the Lyapunov equation

$$A_{11}S_1 + S_1A_{11} = -A_{11}WA_{11}$$

admits a unique solution $S_1 = S_1^T > 0$ given by

$$S_1 = [S_{1,ij}]_{\substack{1\leq i\leq N\\1\leq j\leq N}} = \left[\frac{W_{ij}}{\tau_{w,i} + \tau_{w,j}}\right]_{\substack{1\leq i\leq N\\1\leq j\leq N}}, \tag{5.31}$$

where the subscripts ij denote the ith row and jth column of the matrix. Next, since A_{22} is asymptotically stable as well, the Sylvester equation

$$A_{11}S_2 + S_2A_{22} = -S_1A_{21}$$

admits a unique solution S_2 given by

$$S_2 = [S_{2,ij}]_{\substack{1\leq i\leq N\\1\leq j\leq N}} = \left[\frac{\gamma_j S_{1,ij}}{\frac{1}{\tau_{w,i}} + \frac{1+K_{p,j}}{\tau_j}}\right]_{\substack{1\leq i\leq N\\1\leq j\leq N}}. \tag{5.32}$$

Finally, in a similar way, by solving the Lyapunov equation

$$A_{22}S_3 + S_3A_{22} = -A_{21}S_2 - S_2^TA_{21},$$

S_3 can be calculated as

$$S_3 = [S_{3,ij}]_{\substack{1\leq i\leq N\\1\leq j\leq N}} = \left[\frac{\gamma_i S_{2,ij} + \gamma_j S_{2,ji}}{\frac{1+K_{p,i}}{\tau_i} + \frac{1+K_{p,j}}{\tau_j}}\right]_{\substack{1\leq i\leq N\\1\leq j\leq N}}. \tag{5.33}$$

Therefore, with the partitioning of S and Q, the cost function J_2 can be written as

$$\begin{aligned} J_2 &= \mathrm{trace}(SQ) = \mathrm{trace}(S_3Q_{22}) \\ &= \sum_{i=1}^{N}\sum_{j=1}^{N} S_{3,ij} + \sum_{i=1}^{N} \epsilon_i K_{p,i}^2 S_{3,ii}, \end{aligned} \tag{5.34}$$

where, as pointed out before, the first term represents the smoothness of the wind farm power output, while the second term represents the control effort.

Optimal Proportional Controller Gains

Observe from (5.31)–(5.34) that J_2 is a function of the turbine parameters τ_i's and γ_i's which are known, the wind speed parameters W and $\tau_{w,i}$'s which may be estimated, the weights ϵ_i's which may be chosen, and the proposed controller gains $K_{p,i}$'s. Thus, the optimal proportional controller gains K_p^* that minimize the cost function J_2, in principle, may be determined based on quantities which are either known, may be estimated, or may be chosen. To compute such a K_p^*, we consider a steepest descent optimization approach:

$$\begin{bmatrix} \dot{K}_{p,1} \\ \dot{K}_{p,2} \\ \vdots \\ \dot{K}_{p,N} \end{bmatrix} = -\varepsilon \begin{bmatrix} \frac{\partial J_2}{\partial K_{p,1}} \\ \frac{\partial J_2}{\partial K_{p,2}} \\ \vdots \\ \frac{\partial J_2}{\partial K_{p,N}} \end{bmatrix}, \tag{5.35}$$

which is guaranteed to find a local minimizer. In (5.35), $\varepsilon > 0$ is a design parameter, and the partial derivatives $\frac{\partial J_2}{\partial K_{p,i}}$'s can be calculated in a straightforward manner using (5.31)–(5.34).

5.5.3 Estimation of Wind Speed Parameters

As was pointed out above, the cost function J_2 depends on the wind speed parameters W and $\tau_{w,1}, \ldots, \tau_{w,N}$, which is not readily available and must be explicitly estimated. Hence, to implement (5.35) for solving the smoothness optimization problem, an *Estimation of Wind Speed Parameters* block is needed as shown in Figure 5.4, which provides an estimate $\hat{W}$ of the covariance matrix W and estimates $\hat{\tau}_{w,1}, \ldots, \hat{\tau}_{w,N}$ of the time constants based on measurements of the wind speeds $V_{w,i}(t)$'s. As the design of such a block is not within the scope of this research (we refer the reader to [70] for methods to do so), we assume that such a block is given.

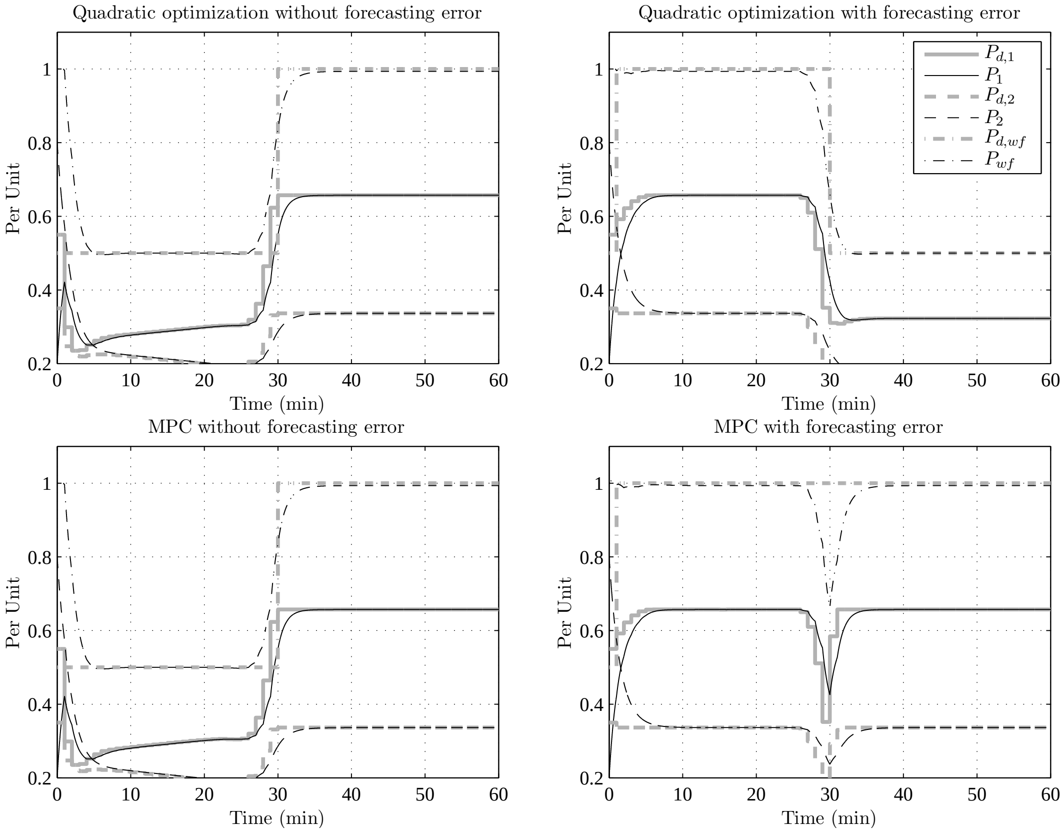

Figure 5.5: One-shot quadratic optimization vs. Iterative MPC

5.6 Simulation Studies

To demonstrate the effectiveness of the WFC presented above, numerical simulations have been carried out, where we test the model predictive controller, the adaptive controller, and the proposed WFC, respectively.

5.6.1 Simulation Results for the Model Predictive Controller

In this subsection, we first demonstrate that by repeatedly solving the optimization problem (5.11), the model predictive controller takes advantage of the updated forecast. The simulation settings are as follows: We consider a wind farm with two turbines. The values of the parameters are $\alpha_1 = 0.657$,

$\tau_1 = 60\,\text{sec}$, $\alpha_2 = 0.657$, $\tau_2 = 90\,\text{sec}$, and constant wind speeds $V_{w,1}(t) = 1\,\text{pu}$ and $V_{w,2}(t) = 0.8\,\text{pu}$. For the controller, we choose its parameters $T_s = 1\,\text{min}$, the length of the time horizon $K = 200\,\text{min}$, $\eta(k) = 1$, $\mu_1(k) = 1$, $\nu_1(k) = 10^{-6}$, $\mu_2(k) = 2$, $\nu_2(k) = 10^{-6}$. Moreover, we assume that the wind speed forecasts are accurate. The simulation results are as follows: we compare the model predictive controller with the quadratic optimization method, which only solves the optimization problem (5.11) based on forecast of the wind speeds and the desired power reference at time $t = 0$. Simulations are carried out to show the key differences between them. Figure 5.5 shows the simulation results. Note that when there is no forecast error on the wind farm power demand $P_{d,wf}(t)$, the two controllers generate very similar results, as shown in the left two subplots in Figure 5.5; when forecast error does happen, the quadratic optimization method cannot incorporate the updated forecast, while the model predictive controller can. As was shown in the right subplots in Figure 5.5, at $t = 0$, the power demand forecast has a sharp drop from $1.0\,\text{pu}$ to $0.5\,\text{pu}$ at time $t = 30\,\text{min}$. Both controllers reduce the power output accordingly. At $t = 30\,\text{min}$, when the updated demand forecast cancels the drop and restores constant power output, the model predictive controller quickly increases the power output to react, whereas the quadratic optimization method does not react at all.

Next, we illustrate the attributes of the model predictive controller compared with a well-known WFC [5] comprising a proportional controller and an even distribution according to available wind power of each turbines. To carry out the illustration, consider the same set of parameters as above, and let the proportional controller gain $K_p = 10$ and the wind farm power demand experience step changes between 1.0 and $0.5\,\text{pu}$. Also assume that the wind speed

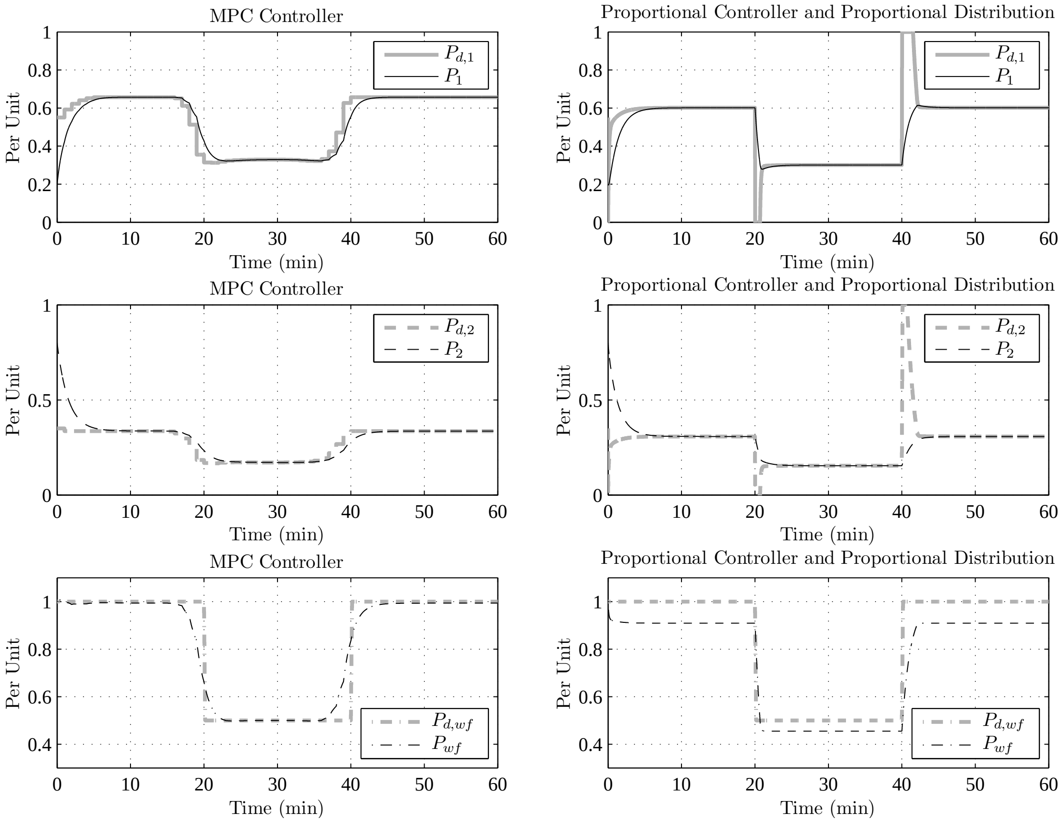

Figure 5.6: MPC vs a WFC comprising a proportional controller and an even distribution of wind power load [5].

forecasts are accurate. The simulation results are shown in Figure 5.6, from which several observations can be made: first, due to utilization of the forecasts, the model predictive controller is able to begin taking actions in advance, which is important to the current wind turbines with large size and inertia. For example, when the demand drops from 1.0 to 0.5 pu at time equals to 20 min, based on the accurate forecast, the model predictive controller reduces the wind farm power output even before the power demand drops, thereby avoiding the sharp drop in the wind farm power output. Second, without integral action, the model predictive controller is able to generate the right amount of power according to the power demand, if the wind is large enough, whereas the proportional controller has steady-state errors. Although not considered, it is conceivable that even with an integral term, the resulting proportional-integral controller would still suffer from the well-known anti-windup issue. Third, by properly adjusting the weights in the cost function, the model predictive controller is able to achieve a balance between fast, abruptly changing power demands $P_{d,i}(t)$'s, and slow, smoothly varying ones.

5.6.2 Simulation Results for the Adaptive Controller

In this subsection, we first introduce, for the fast wind speed components, the following four different types of wind speed correlation and the corresponding covariance matrix W, as shown in Figure 5.7:

- *Moderately correlated.* This case may correspond to a row of wind turbines, where the wind is blowing from left to right. The distance between two adjacent turbines are neither too close nor too far away, so that the correlation between the fast wind speeds at two nearby turbines is moderate.

- *Strongly correlated.* This one may correspond to a row of wind turbines and the wind is blowing toward them simultaneously. The distance between two turbines is relatively close, so that the correlation between the fast wind speeds at two turbines is strong.

- *Totally uncorrelated.* This case is similar to the first one, except that the turbines are very far apart, so that the fast wind speeds are totally uncorrelated.

- *Negatively correlated.* This one relates to the situation where turbines are so close to each other, that some may locate in the turbulence and

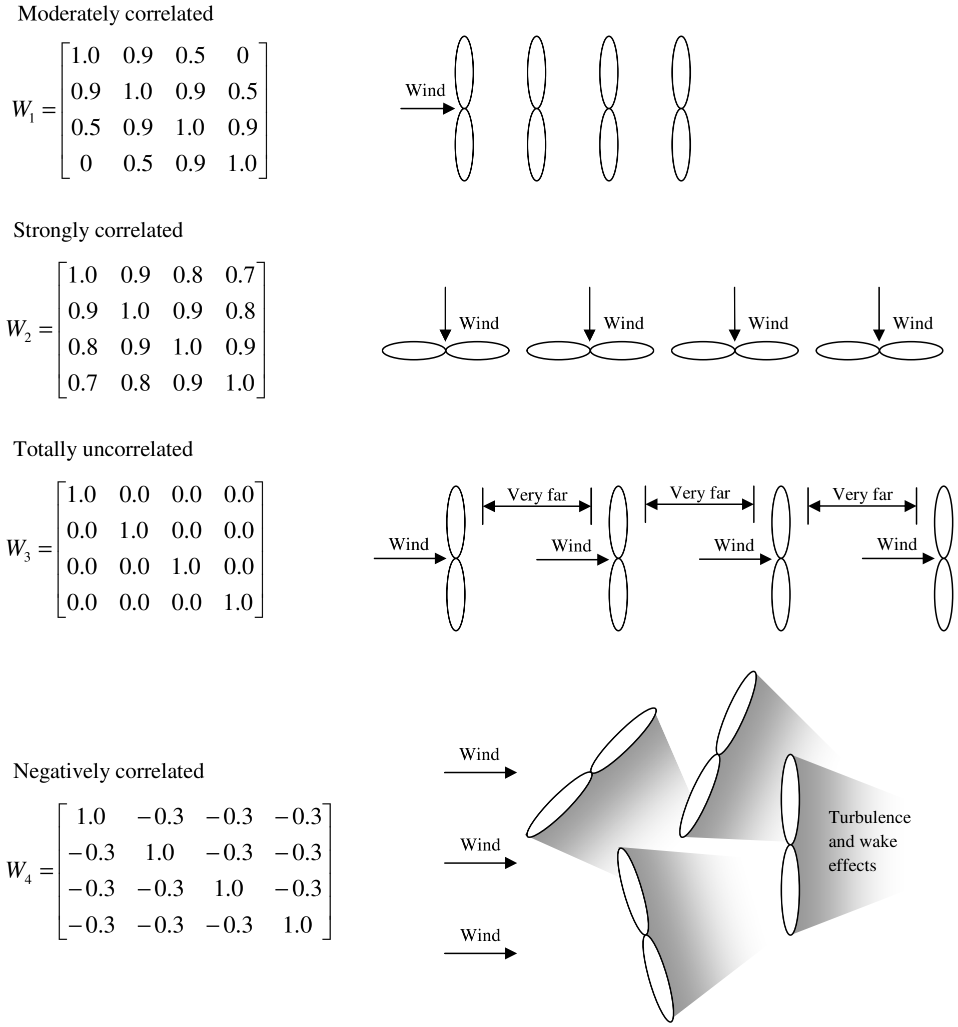

Figure 5.7: Different correlations and the fast wind speed components.

wake area of the others. Hence, if some turbines grab too much wind energy, others will experience weaker wind. Thus, the wind speeds at two turbines are likely negatively correlated.

Next, if we let all the ϵ_i's in (5.34) be equal and denote it simply as ϵ, (5.34) can be written as

$$J_2 = \sum_{i=1}^{N} \sum_{j=1}^{N} S_{3,ij} + \epsilon \sum_{i=1}^{N} K_{p,i}^2 S_{3,ii}, \tag{5.36}$$

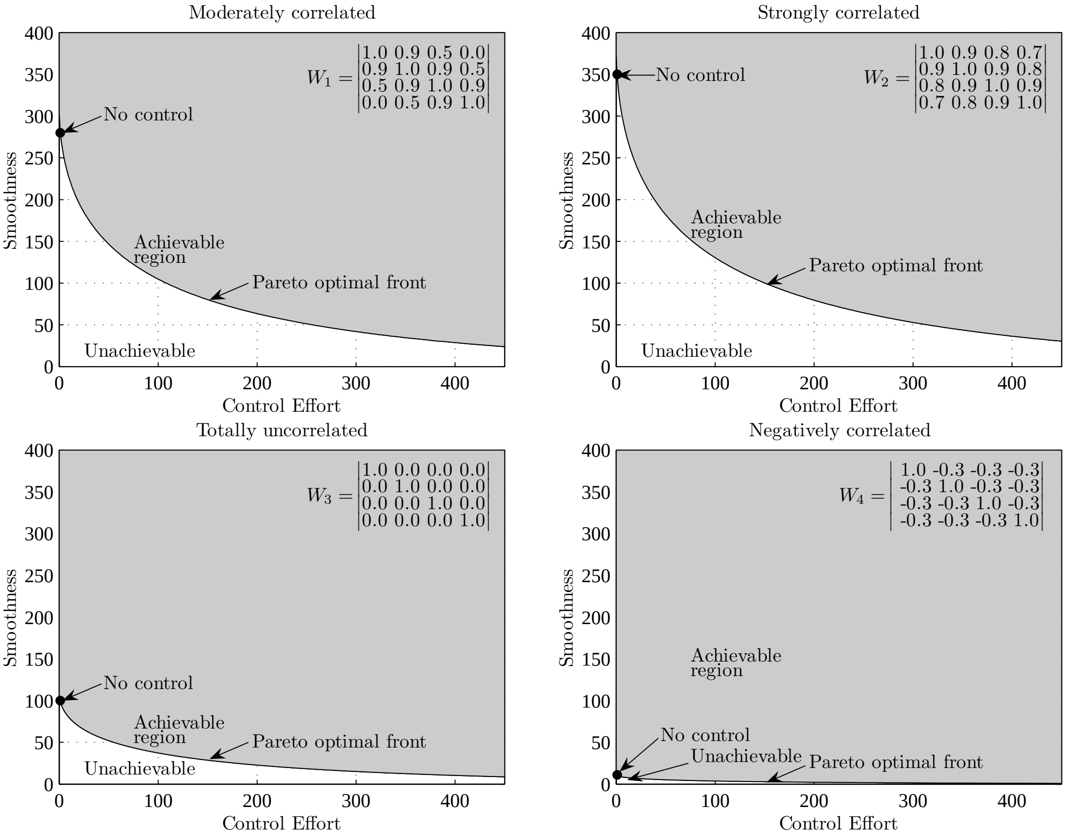

Figure 5.8: Pareto optimal curves.

where $\epsilon > 0$. Equation (5.36) forms a Pareto optimal between the smoothness of the wind farm power output and the control effort for each $\epsilon > 0$. Hence, if we let ϵ vary over a large range, it forms a Pareto optimal curve. For the four different types of correlation considered above, we draw the Pareto optimal curve for each type of correlation, respectively, as shown in Figure 5.8. Moreover, the region containing all the achievable points is marked in gray. Finally, in Figure 5.9, we superimpose the four Pareto optimal curves together. Observe that, for a given control effort, the case where W is negatively correlated yields the best smoothness among the four types. The next best smoothness comes from the totally uncorrelated case, which is not surprising as this shows the

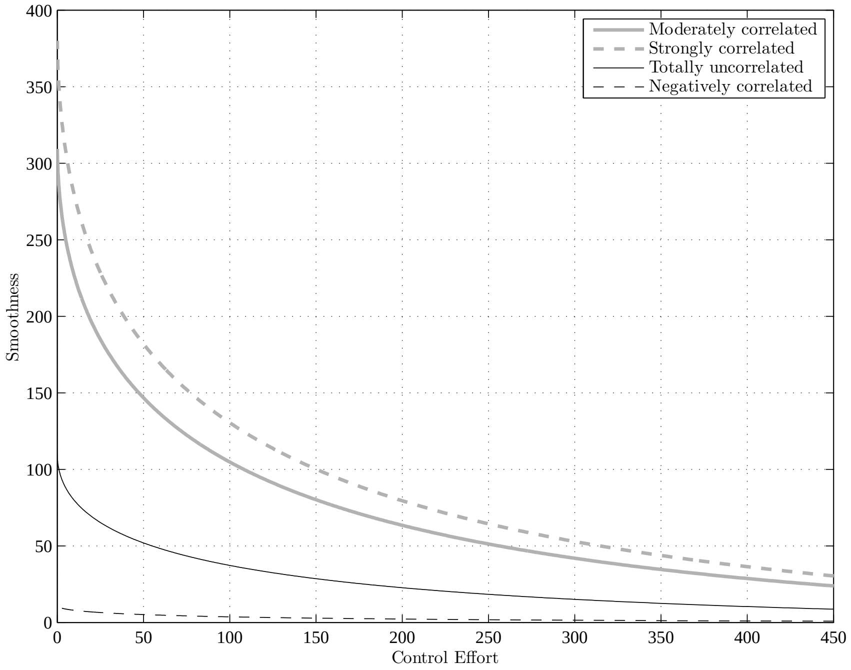

Figure 5.9: Superimposed Pareto optimal curves.

benefit of having diversity. Finally, the strongly correlated case has the worst smoothness, followed by the moderately correlated case.

5.6.3 Simulation Results for the Proposed WFC

In this subsection, we demonstrate the capability and effectiveness of the proposed WFC by carrying out simulation in MATLAB. The simulation settings are as follows: We consider a wind farm with $N = 10$ wind turbines of the same type, whose parameters take the following values: $\tau_i = 60\,\text{seconds}$, $\alpha_i = 0.657$, $\gamma_i = 0.02$, $T_s = 60\,\text{seconds}$, and $K = 100$. Moreover, we let the values of the optimization parameters be: $\eta(k) = 1$, $\mu_1(k) = \mu_6(k) = 1$, $\mu_2(k) = \mu_7(k) = 2$, $\mu_3(k) = \mu_8(k) = 4$, $\mu_4(k) = \mu_9(k) = 8$, $\mu_5(k) = \mu_{10}(k) = 16$, $\nu_i(k) = 1 \times 10^{-6}$, $\epsilon_i = 1$, and $\epsilon = 1$. Note that we intentionally choose the $\mu_i(k)$'s so that changes in the $P_{d,i}[k]$'s are least penalized for turbines 1

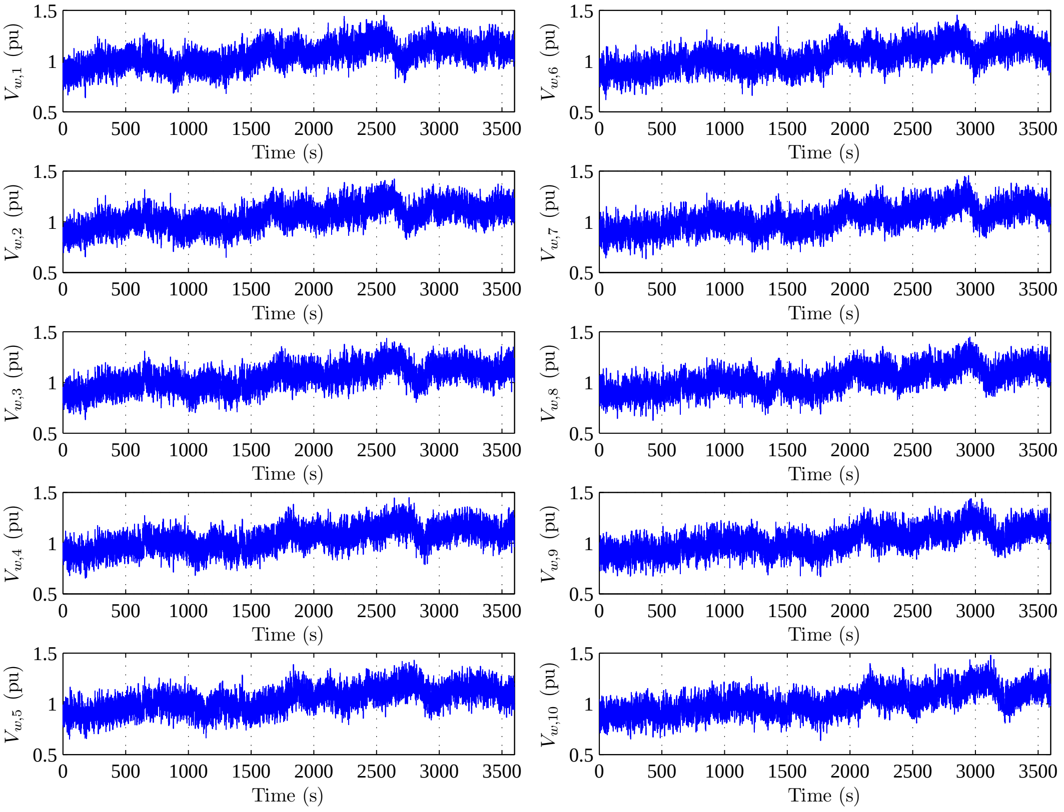

Figure 5.10: Wind speeds $V_{w,i}(t)$'s used in the simulation of the proposed WFC.

and 6, followed by turbines 2 and 7, and so on. In addition, we let the values of the specific wind speed model parameters be $\tau_{w,i} = 1\,\text{second}$ and be such that the entry in the ith row and jth column of the covariance matrix W is $W_{ij} = 0.99^{|i-j|\sigma}$, where $\sigma = 10$. Note that for simplicity, we assume that both the $\tau_{w,i}$'s and W are constant over time, and that the Estimation of Wind Speed Parameters block operates ideally, so that $\hat{\tau}_{w,i} = \tau_{w,i}$ for all $i = 1, 2, \ldots, N$ and $\hat{W} = W$. It follows from gradient-based numerical optimization that the optimal proportional controller gains K_p^* are given by $[1.7380\ 1.9038\ 2.0252\ 2.1041\ 2.1430\ 2.1430\ 2.1041\ 2.0252\ 1.9038\ 1.7380]^T$. As for the slow, average components of $V_{w,i}(t)$'s, i.e., $\bar{V}_{w,i}(t)$'s, we let $\bar{V}_{w,1}(t)$ be defined by an actual wind profile from a wind farm located in northwest

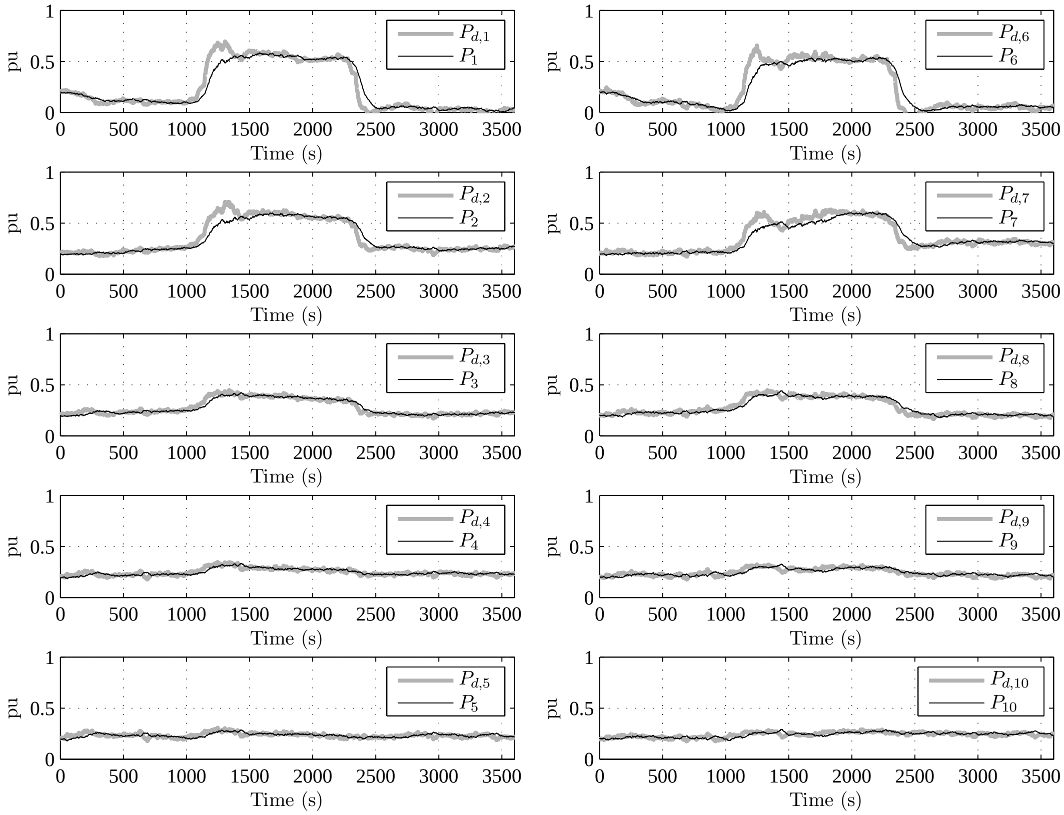

Figure 5.11: Wind turbine desired power outputs $P_{d,i}(t)$'s and actual power outputs $P_i(t)$'s in the simulation of the proposed WFC.

Oklahoma, and let $\bar{V}_{w,i}(t)$ be defined by shifting $\bar{V}_{w,1}(t)$ by $(i-1)$ minutes for $i = 2, 3, \ldots, N$. The resulting wind speeds $V_{w,i}(t)$'s are shown in Figure 5.10. Finally, we choose the initial conditions to be $P_{d,i}[0] = 0.2$ and $P_i[0] = 0.2$ for $i = 1, 2, \ldots, N$ and consider a scenario where the desired wind farm power output $P_{d,wf}(t)$ experiences large step changes between 2 pu and 4 pu.

The simulation results are as follows: First, Figure 5.11 shows wind turbine desired power outputs $P_{d,i}(t)$'s and actual power outputs $P_i(t)$'s in the simulation of the proposed WFC of each turbine, from which we can observe that for each i, $P_{d,i}(t)$ undergoes larger variations if μ_i is relatively small (e.g., in the case of turbines 1 and 6) and smaller variations otherwise (e.g., in the case

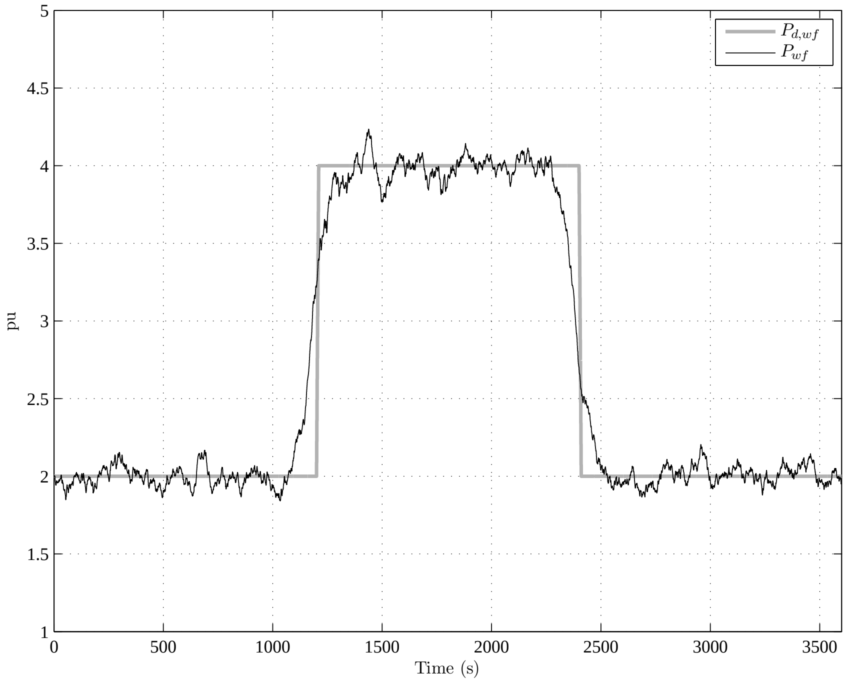

Figure 5.12: Wind farm desired power output $P_{d,wf}(t)$ and actual power output $P_{wf}(t)$ in the simulation of the proposed WFC.

of turbines 5 and 10). More important, every $P_i(t)$ closely tracks $P_{d,i}(t)$ despite the significant wind fluctuations as shown in Figure 5.11. Second, Figure 5.12 shows wind farm desired power output $P_{d,wf}(t)$ and actual power output $P_{wf}(t)$ in the simulation of the proposed WFC, from which we can observe that $P_{wf}(t)$ accurately and smoothly tracks $P_{d,wf}(t)$, achieving the ultimate objective of the proposed WFC. Moreover, due to the built-in feature of the model predictive controller—namely, an ability to incorporate (revised) forecasts—the wind farm is able to take actions in advance, enabling $P_{wf}(t)$ to react to an impending change in $P_{d,wf}(t)$ as can be seen from time 1200 seconds and time 2400 seconds of Figure 5.12.

5.7 Conclusion

In this chapter, we have developed a wind farm controller, which enables the wind farm power output to accurately and smoothly track the desired power reference. The controller comprises a model predictive controller cooperatively optimizing the tracking performance of the wind farm power output on a longer timescale, as well as a self-tuning regulator-type adaptive controller jointly optimizing the smoothness of the power output on a shorter timescale. Simulation has been carried out, and the results illustrate the positive features of the proposed controller.

Chapter 6 Wind Farms with Kinetic Energy Release: A Control Perspective

6.1 Introduction

In this chapter, we consider an MPT controller augmented with a proportional inertia response (PIR) controller, and obtain analytical answers to some of the open questions. More specifically, we first analyze the resulting, nonlinear wind turbine control system and show that, under some conditions, the system contains an asymptotically stable equilibrium point, which is desirable. There are, however, other conditions under which the nonlinearity can cause problems. We then linearize the system and show that its transfer function contains a zero at the origin, which may lead to some potential issues. Finally, we study the stability of the power system frequency response model and show that the MPT-inertia response controller will not cause instability when only the reheat steam turbine generating units are considered.

The remainder of this chapter is organized as follows. Section 6.2 describes a variable-speed wind turbine model as well as a power system frequency response model. Section 6.3 analyzes the behavior of the MPT controller with inertia response. Finally, Section 6.4 concludes this chapter.

6.2 Modeling

In this section, we first introduce, in Section 6.2.1, a variable-speed wind turbine model. We then describe, in Section 6.2.2, a power system frequency response model, which builds upon the one in Section 6.2.1.

6.2.1 Variable-Speed Wind Turbine Model

Consider a variable-speed wind turbine model given by

$$J\frac{d}{dt}\omega_r = T_m - T_e, \tag{6.1}$$

$$P_e = T_e\omega_r, \tag{6.2}$$

where $J > 0$ is the moment of inertia, $\omega_r > 0$ is the rotor angular velocity, T_m is the mechanical torque, T_e is the electromagnetic torque, and P_e is the generated electrical power. The mechanical torque T_m is given by

$$T_m = \frac{P_m}{\omega_r} = \frac{\frac{1}{2}\rho\pi R^2 C_p(\lambda,\beta)V_w^3}{\omega_r}, \tag{6.3}$$

where P_m is the mechanical power captured by the wind turbine, $\rho > 0$ is the air density, $R > 0$ is the rotor blade radius, $V_w > 0$ is the wind speed, and C_p is the performance coefficient, which is a function of the tip speed ratio $\lambda = \frac{R\omega_r}{V_w} > 0$ and the blade pitch angle β. In this chapter, we assume that the $C_p(\lambda,\beta)$ surface satisfies the following conditions:

(A1) There exists a unique (λ^*,β^*) such that $C_p^* \triangleq C_p(\lambda^*,\beta^*) \geq C_p(\lambda,\beta)$ for all (λ,β);

(A2) $\frac{\partial}{\partial\lambda}C_p(\lambda^*,\beta^*) = 0$;

(A3) For every $\lambda < \lambda^*$ and for $\beta = \beta^*$, $C_p(\lambda,\beta) > \frac{C_p^*}{(\lambda^*)^3}\lambda^3$.

Note that (A1) and (A2) are common assumptions on $C_p(\lambda,\beta)$ surfaces, whereas (A3) is a standard assumption adopted in [4] to establish MPT.

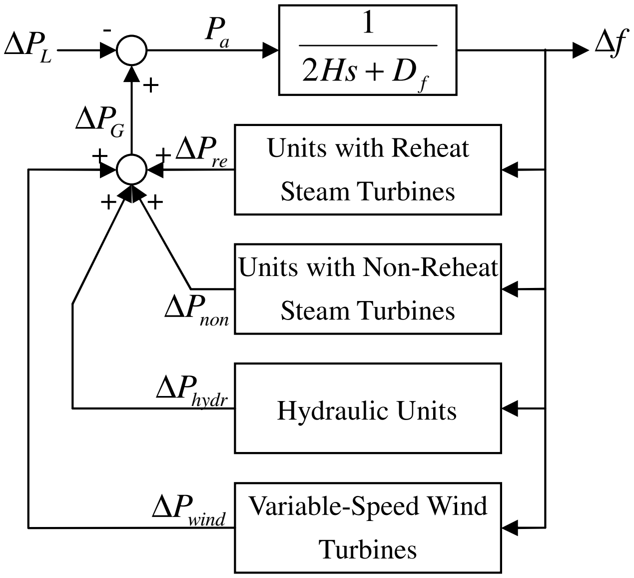

Figure 6.1: Power system frequency response model.

6.2.2 Power System Frequency Response Model

Next, consider a power system frequency response model [94] as shown in Figure 6.1, where synchronizing oscillations among generators are filtered out and only the average and collective frequency behaviors are retained. In the figure, $H > 0$ is the lumped inertia constant, $D_f > 0$ is the damping factor (representing the frequency-dependent portion of the load), s is the Laplace operator, P_a is the accelerating power, and Δf is the power system frequency deviation. In addition, ΔP_{re}, ΔP_{non}, ΔP_{hydr}, and ΔP_{wind} are the incremental powers from Units with Reheat Steam Turbines, Units with Non-Reheat Steam Turbines, Hydraulic Units, and Variable-Speed Wind Turbines, respectively. Moreover, $\Delta P_G = \Delta P_{re} + \Delta P_{non} + \Delta P_{hydr} + \Delta P_{wind}$ and ΔP_L are the incremental powers from all the generating units and all the loads. In this chapter, we assume that for the first three conventional types of generating units, their transfer functions are given by [95]

$$\frac{\Delta P_{re}(s)}{\Delta f(s)} = \sum_i (-\frac{1 + sF_{H,i}T_{R,i}}{R_i(1 + sT_{G,i})(1 + sT_{CH,i})(1 + sT_{R,i})}), \tag{6.4}$$

$$\frac{\Delta P_{non}(s)}{\Delta f(s)} = \sum_i (-\frac{1}{R_i(1 + sT_{G,i})(1 + sT_{CH,i})}), \tag{6.5}$$

$$\frac{\Delta P_{hydr}(s)}{\Delta f(s)} = \sum_i (-\frac{(1 + sT_{R,i})(1 - sT_{W,i})}{R_i(1 + sT_{G,i})(1 + s\frac{R_{T,i}}{R_{P,i}}T_{R,i})(1 + 0.5sT_{W,i})}), \tag{6.6}$$

where i represents the ith unit and the definition of all the constant parameters can be found in [95]. For the fourth type of generating unit, namely, the variable-speed wind turbines, its transfer function may be obtained by linearizing the nonlinear model in Section 6.2.1, which will be carried out in Section 6.3.2.

6.3 Analysis

In this section, we study the frequency behaviors of a large power system to sudden load disturbances. We first analyze, in Section 6.3.1, the equilibrium points of the wind turbine with an MPT controller augmented with a PIR controller. Based on the equilibrium point analysis, we next linearize, in Section 6.3.2, the nonlinear wind turbine model and discuss its implication. Finally, in Section 6.3.3, we study the stability of a simplified power system frequency model that assumes an equivalent single machine lumping of multiple and the linearized wind turbine models.

6.3.1 Equilibrium Point Analysis

Consider the widely-studied, MPT controller proposed in [4] and given by

$$T_e = K^* \omega_r^2, \tag{6.7}$$

where $K^* = \frac{1}{2}\rho\pi R^5 \frac{C_p^*}{(\lambda^*)^3}$. It has been shown in [4] that with (6.7) and with constant blade pitch angle $\beta = \beta^*$, constant wind speed V_w, and Assumptions (A1)–(A3), the MPT is always achieved, i.e., $\lambda \to \lambda^*$ or equivalently $\omega_r \to \omega_r^* \triangleq \frac{\lambda^* V_w}{R}$ as time goes to infinity. Moreover, the control law (6.7) decouples the wind turbine and the power system in the sense that it prevents the wind turbine from responding to the system frequency changes. In order to introduce some inertia response in such a wind turbine, an additional torque T_{iner} is added to the electromagnetic torque control law (6.7). Several different control strategies may be used to determine T_{iner}. In this paper, we consider the proportional controller investigated in [58], of the form

$$T_{iner} = -K_p(f - f_d), \tag{6.8}$$

where $K_p > 0$ is the proportional gain, f is the system frequency, and f_d is the nominal frequency. Combining (6.1)–(6.3), (6.7), and (6.8), we obtain a nonlinear state space form

$$\begin{aligned} \dot{\omega}_r &= \frac{1}{J}\Big[\frac{\frac{1}{2}\rho\pi R^2 C_p(\lambda,\beta) V_w^3}{\omega_r} - (K^*\omega_r^2 - K_p(f - f_d))\Big] \\ &\triangleq F_1(\omega_r, \beta, V_w, f - f_d), \qquad (6.9) \\ P_e &= (K^*\omega_r^2 - K_p(f - f_d))\omega_r \triangleq F_2(\omega_r, f - f_d), \qquad (6.10) \end{aligned}$$

where ω_r is the state, β, V_w, and $f - f_d$ are the inputs, and F_1 and F_2 are nonlinear functions.

For analysis purposes, let us assume that $\beta = \beta^*$, and that both V_w and $f - f_d$ are constant. To find the equilibrium points, set $F_1(\omega_r, \beta^*, V_w, f - f_d) = 0$, i.e.,

$$\begin{aligned}
-K_p(f - f_d) &= \frac{\frac{1}{2}\rho\pi R^2 C_p(\lambda, \beta^*) V_w^3}{\omega_r} - K^* \omega_r^2, \\
&= \frac{1}{2}\rho\pi R^3 V_w^2 \left(\frac{C_p(\lambda, \beta^*)}{\lambda} - \frac{C_p^*}{(\lambda^*)^3}\lambda^2\right).
\end{aligned}$$

Multiplying both sides by λ, we get

$$-K_p(f - f_d)\lambda = \frac{1}{2}\rho\pi R^3 V_w^2 \left(C_p(\lambda, \beta^*) - \frac{C_p^*}{(\lambda^*)^3}\lambda^3\right). \tag{6.11}$$

Note that the left-hand side of (6.11) is a *linear* function of λ, whose slope is determined by the product of $K_p(f - f_d)$. In addition, the right-hand side of (6.11) is a *nonlinear* function of λ, which depends on the specific expression of $C_p(\lambda, \beta)$. Figures 6.2 and 6.3 represent the left-hand side for different values of $K_p(f - f_d)$. Also shown is the right-hand side as a function of λ, so that any λ (or, equivalently, any ω_r since $\lambda = \frac{R\omega_r}{V_w}$) at which the two curves intersect represents an equilibrium point. We note that the figures are generated with the following values: $V_w = 1$ (pu), $\lambda^* = 1$ (pu), $\beta^* = 0$ (deg), and the expression of $C_p(\lambda, \beta)$ is adopted from MATLAB/Simulink R2007a and also given in [3]. Also illustrated in the figures is the stability or lack thereof of each equilibrium point, which is marked by the moving directions of λ (or, equivalently, ω_r).

From these two figures, several different cases can be observed:

Case I: No bias, i.e., $f - f_d = 0$. In this case, $T_{iner} = -K_p(f - f_d) = 0$ so that the system behaves as if the PIR controller is absent. It follows from Figure 6.2 that there is only one equilibrium point, at $\lambda = \lambda^*$. In addition, the equilibrium point is asymptotic stable, implying that the MPT mode takes

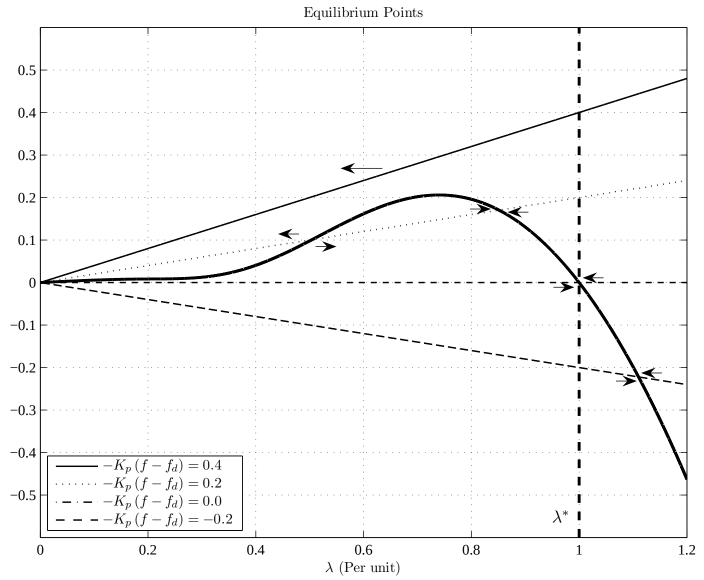

Figure 6.2: Equilibrium points.

place. This also agrees with the stability analysis of the MPT controller (6.7) given in [4].

Case II: Negative bias, i.e., $f - f_d < 0$. This case is of interest because it is possible that, in a large power system, even with inertia response, the frequency f recovers so slowly that $f - f_d$ is approximately a negative bias for an extended period of time. In this case, $T_{iner} = -K_p(f - f_d) > 0$ so that the PIR controller is activated. Unlike Case I, here different values of $-K_p(f - f_d)$ may lead to different number of equilibrium points, each with different characteristics. To see this, note that if $-K_p(f - f_d) = 0.4$, there is *no* equilibrium point and ω_r will keep decreasing until the turbine stops. If $-K_p(f - f_d) = 0.02$, there is a *unique* asymptotically stable equilibrium point. If $-K_p(f - f_d) = 0.2$, there are *two* equilibrium points, one asymptotically stable and one unstable, so that either ω_r approaches the stable equilibrium point or the turbine eventually stops, depending on the initial condition. If

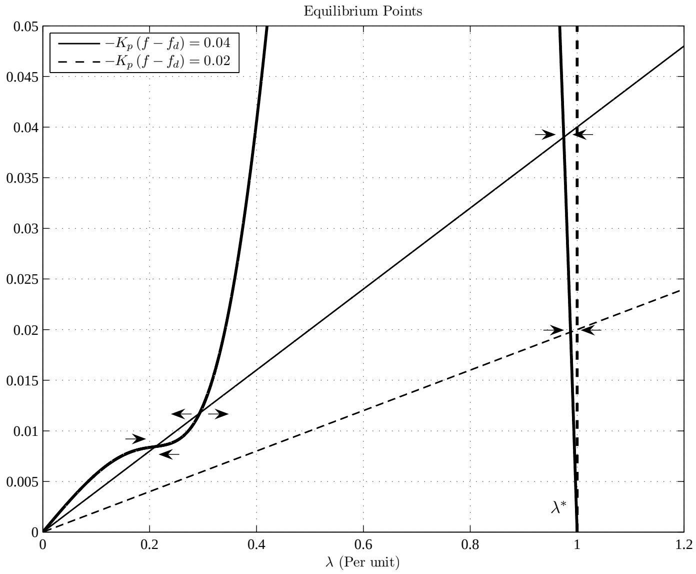

Figure 6.3: Equilibrium points (zoom in).

$-K_p(f - f_d) = 0.04$, there are *three* equilibrium points, two asymptotically stable and one unstable. In this subcase, ω_r converges to either of the two stable equilibrium points (unless it starts at the unstable one), and the turbine does not stop. Finally, note that in each of these four subcases, the equilibrium point λ is to the left of λ^*, suggesting that the system operates to the *left* of the peak of the C_p-curve.

Case III: Positive bias, i.e., $f - f_d > 0$. This case is not as common as Case II but is possible. In this case, $T_{iner} = -K_p(f - f_d) < 0$ so that the PIR controller is also activated. Similar to Case I, there is an asymptotically stable equilibrium point, at $\lambda > \lambda^*$. This means that the system operates to the *right* of the peak of the C_p-curve.

As it follows from the above, the combination of the MPT controller (6.7) and the PIR controller (6.8) works as one would expect under some conditions. However, when these conditions are violated, it may lead to undesirable behaviors such as making the turbine stop or causing it to operate in the vicinity of other equilibrium points.

6.3.2 Model Linearization

From the above equilibrium point analysis, we see that if there is no bias in the power system frequency (i.e., $f - f_d = 0$)—which is the typical case—the nonlinear function (6.9) has only one asymptotically stable equilibrium point at $\lambda = \lambda^*$. In the sequel, we linearize the nonlinear wind turbine control system (6.9) and (6.10) around the operating point $\omega_r^* = \frac{\lambda^* V_w}{R}$ to obtain

$$\frac{d}{dt}\Delta\omega_r = A\Delta\omega_r + B\Delta f, \tag{6.12}$$

$$\Delta P_e = C\Delta\omega_r + D\Delta f, \tag{6.13}$$

where $\Delta\omega_r = \omega_r - \omega_r^*$ is the state, $\Delta f = f - f_d$ is the input, and $\Delta P_e = F_2(\omega_r, f - f_d) - F_2(\omega_r^*, 0)$ is the output. The model parameter A in (6.12) can be determined as follows:

$$\begin{aligned} A &= \frac{\partial F_1}{\partial \omega_r}(\omega_r^*, \beta^*, V_w, 0), \\ &= \frac{1}{2J}\rho\pi R^2 V_w^3 \frac{\frac{\partial}{\partial\lambda}C_p(\lambda^*, \beta^*)\frac{R}{V_w}\omega_r^* - C_p(\lambda^*, \beta^*)}{(\omega_r^*)^2} - \frac{2}{J}K^*\omega_r^*. \end{aligned}$$

Using Assumption (A2) and $K^* = \frac{1}{2}\rho\pi R^5 \frac{C_p^*}{(\lambda^*)^3}$, A may be simplified to

$$\begin{aligned} A &= -\frac{1}{2J}\rho\pi R^2 V_w^3 \frac{C_p^*}{(\omega_r^*)^2} - \frac{2}{J}K^*\omega_r^*, \\ &= -\frac{1}{2J}\rho\pi R^2 (\frac{R\omega_r^*}{\lambda^*})^3 \frac{C_p^*}{(\omega_r^*)^2} - \frac{2}{J}K^*\omega_r^*, \\ &= -\frac{3}{J}K^*\omega_r^* = -\frac{3\lambda^* K^*}{JR}V_w. \end{aligned}$$

Similarly, B in (6.12), and C and D in (6.13) can be computed as follows:

$$B = \frac{\partial F_1}{\partial f}(\omega_r^*, \beta^*, V_w, 0) = \frac{1}{J}K_p,$$

$$
\begin{aligned}
C &= \frac{\partial F_2}{\partial \omega_r}(\omega_r^*, 0) = 3K^*(\omega_r^*)^2 = \frac{3(\lambda^*)^2 K^*}{R^2} V_w^2, \\
D &= \frac{\partial F_2}{\partial f}(\omega_r^*, 0) = -K_p \omega_r^* = -\frac{\lambda^*}{R} K_p V_w.
\end{aligned}
$$

Note that, interestingly,

$$BC = \frac{3(\lambda^*)^2 K^*}{JR^2} K_p V_w^2 = AD.$$

As a result, the transfer function of the linearized model (6.12) and (6.13) simplifies to

$$\frac{\Delta P_e(s)}{\Delta f(s)} = \frac{BC}{s-A} + D = \frac{Ds + BC - AD}{s-A} = \frac{Ds}{s-A} = \frac{-\frac{\lambda^*}{R} K_p V_w s}{s + \frac{3\lambda^* K^*}{JR} V_w}. \tag{6.14}$$

Notice that the transfer function (6.14) reveals two potential issues with the MPT-PIR controller (6.7) and (6.8). First, it has a zero at the origin, which may cause undesirable oscillatory behavior in ΔP_e when the frequency error Δf is noisy, because a zero at the origin differentiates noise. Second, if the PIR controller (6.8) is replaced by a proportional-integral (PI) controller (perhaps as an attempt to eliminate steady-state error), K_p in B and D needs to be replaced by $\frac{K_p s + K_I}{s}$, so that (6.14) becomes

$$\frac{\Delta P_e(s)}{\Delta f(s)} = \frac{-\frac{\lambda^*}{R} V_w s}{s + \frac{3\lambda^* K^*}{JR} V_w} \frac{K_p s + K_I}{s},$$

suggesting that there is an impending pole-zero cancellation. As is well known in controls, pole-zero cancellations are undesirable and should be avoided whenever possible.

6.3.3 Stability Analysis

Finally, we study the stability of the power system frequency response model. To simplify the analysis, we adopt the idea in [94], which is to use an equivalent single machine to represent the dynamic behaviors of the same type of machines in a large system. For this idea to be valid, it is necessary that: (i) the disturbance to the system is small compared to the total rating of the system, (ii) the equivalent machine is able to absorb this change, and (iii) a constant power factor for all the machines. This concept reduces the power system model shown in Figure 6.1 to one described by a minimum number of equations and also widely used in [96–98] to study load shedding when a serious disturbance happens in the power system. As a result, each of the four generating unit blocks in Figure 6.1 may be viewed as an equivalent single machine. For example, we may use the above transfer function of the linearized wind turbine model (6.14) to represent the *Variable-Speed Wind Turbines* block by appropriately choosing the equivalent model parameters V_w and K_p, assuming that the wind speed across the wind farm is roughly the same and assuming that the proportional gains are all identical.

In the stability analysis below, for simplicity we assume that there is only one type of conventional generating units in the power system, namely, the reheat steam turbines. In addition, we assume that these units can be represented by an equivalent single machine, and that its transfer function given earlier in (6.4) can be simplified to

$$\frac{\Delta P_{re}(s)}{\Delta f(s)} = -\frac{K_m(1 + F_H T_R s)}{R_R(1 + T_R s)}, \tag{6.15}$$

where $K_m > 0$ is the mechanical power gain factor, $0 < F_H < 1$ is the fraction of total power generated by the HP turbine, $T_R > 0$ is the reheat time constant, and $R_R > 0$ is the governor regulation gain (see [94] for more details). With these assumptions, Figure 6.1 simplifies to Figure 6.4.

Note from Figure 6.4 that the transfer function of the closed-loop system

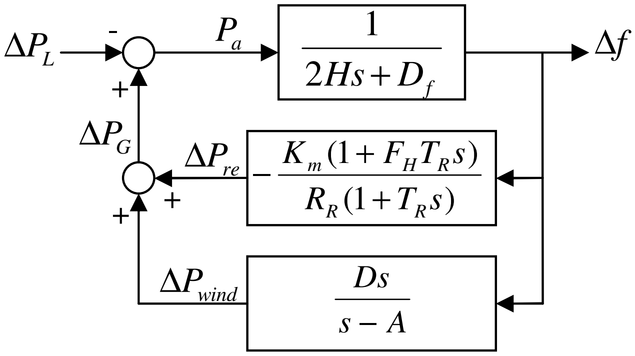

Figure 6.4: A simplified power system model derived from Figure 6.1.

is given by

$$\begin{aligned}\frac{\Delta f(s)}{\Delta P_L(s)} &= \frac{-\frac{1}{2Hs+D_f}}{1-\frac{1}{2Hs+D_f}(-\frac{K_m(1+F_H T_R s)}{R_R(1+T_R s)}+\frac{Ds}{s-A})},\\ &= -\frac{b_0 s^2+b_1 s+b_2}{a_0 s^3+a_1 s^2+a_2 s+a_3}, \qquad (6.16)\end{aligned}$$

where a_0, a_1, a_2, a_3, b_0, b_1, and b_2 are defined as

$$a_0 = 2HR_RT_R,$$

$$a_1 = 2HR_R - 2AHR_RT_R + D_fR_RT_R + K_mF_HT_R - DR_RT_R,$$

$$a_2 = -2AHR_R + D_fR_R - AD_fR_RT_R + K_m - AF_HK_mT_R - DR_R,$$

$$a_3 = -AD_fR_R - AK_m,$$

$$b_0 = R_RT_R,$$

$$b_1 = R_R - AR_RT_R,$$

$$b_2 = -AR_R.$$

Since A and D in (6.14) are both negative and since all the constant parameters are positive, all the a_i's defined above are positive. Thus, the denominator of (6.16) satisfies the necessary stability condition. In addition, with some straightforward manipulation, it can be shown that $a_1a_2 - a_0a_3 > 0$. Applying the Routh-Hurwitz stability criterion to the denominator of (6.16), we see that the closed-loop system is *always* asymptotically stable. This finding shows that when only reheat steam turbines are considered, the MPT-PIR controller is a reasonable design choice that will not compromise the system stability.

Finally, we stress that the above analysis may be carried out in a similar fashion for more than one types of conventional generating units and without the equivalent single machine assumption. Unfortunately, the analysis would become much more involved because of the very high order of the resulting closed-loop transfer function. One way to overcome this difficulty is to resort to Nyquist graphical stability methods. We believe this is possibly a fruitful future research direction.

6.4 Conclusion

In this chapter, we have analyzed the behavior of a variable-speed wind turbine equipped with a standard MPT controller and a PIR controller using classic control and basic nonlinear systems theory. The analysis has revealed several performance issues, which may hamper the ability of such turbines in providing short-term frequency support through inertia response. The finding suggests that more research may be needed to fully understand the severity of such issues and how to alleviate them.

Chapter 7 Conclusions

7.1 Overall Summary

In this dissertation, we have designed and analyzed a novel, diverse collection of controllers for variable-speed wind turbines and large-scale wind farms, which significantly advance the state of the art.

We have developed a feedback/feedforward nonlinear controller, which accounts for the nonlinearities in variable-speed wind turbines with DFIGs, and bypasses the need for approximate linearization. Its development is based on applying a mixture of linear and nonlinear control design techniques on three timescales, including feedback linearization, pole placement, and gradient-based minimization of a Lyapunov-like potential function. Simulation results have shown that the proposed scheme not only effectively controls the active and reactive powers in both the MPT and PR modes, it also ensures seamless switching between the two.

We have also constructed a controller based on a fifth-order, electromechanically coupled, nonlinear model of the wind turbine by integrating several control strategies and exploiting timescale separation in the dynamics. As an extension of the previous one, the controller does not require knowledge of the C_p-surface, air density, friction coefficient, and wind speed. Simulation has been carried out using realistic wind profiles, and the results demonstrate the capability and effectiveness of the controller.

In addition, we have presented a structurally simple, approximate WTCS model, which tries to mimic generic analytical and empirical WTCS models, along with two parameter identification schemes, which determine the approximate model parameters in both cases. We have also demonstrated through simulation the accuracy and versatility of the approximate model in resembling several different analytical and empirical WTCS models from the literature and from real data. From the results, we conclude that the approximate model is a compelling candidate in research of wind farm power control.

Furthermore, we have developed a wind farm controller, which enables the wind farm power output to accurately and smoothly track the desired power reference. The controller comprises a model predictive controller cooperatively optimizing the tracking performance of the wind farm power output on a longer timescale, as well as a self-tuning regulator-type adaptive controller jointly optimizing the smoothness of the power output on a shorter timescale. Simulation has been carried out, and the results illustrate the positive features of the proposed controller.

Finally, we have analyzed the behavior of a variable-speed wind turbine equipped with a standard MPT controller and a proportional inertia response controller using classic control and basic nonlinear systems theory. The analysis has revealed several performance issues, which may hamper the ability of such turbines in providing short-term frequency support through inertia response. The finding suggests that more research may be needed to fully understand the severity of such issues and how to alleviate them.

7.2 Future Work

Although this dissertation has addressed a number of key problems and pressing issues in the area of wind turbine and wind farm control, there are several possible future research directions, which may be of interest:

- *Analysis of the transient characteristics of the proposed wind farm controller.* While simulation results show that the wind farm controller developed in Chapter 5 is promising, deeper theoretical understanding of its capability and limitations, especially its transient characteristics, is valuable. Such characteristics may include the response time at various wind speed and direction, the corresponding overshoot or lack thereof, and the steady-state error, when the wind farm power reference experiences step changes.

- *Wind farm sequential kinetic energy release.* Currently, kinetic energy release for power system frequency support is carried out at wind turbine level in an autonomous way. The hierarchical architecture of a wind farm control system adopted in Chapters 4 and 5 offers a richer set of options on how kinetic energy may be released, which take advantage of the potential cooperations among the turbines, and the diversity of wind speeds they experience.

Bibliography

[1] J. L. Rodriguez-Amenedo, S. Arnalte, and J. C. Burgos, “Automatic generation control of a wind farm with variable speed wind turbines,” *IEEE Transactions on Energy Conversion*, vol. 17, no. 2, pp. 279–284, June 2002.

[2] L. M. Fernandez, C. A. Garcia, and F. Jurado, “Comparative study on the performance of control systems for doubly fed induction generator (DFIG) wind turbines operating with power regulation,” *Energy*, vol. 33, no. 9, pp. 1438–1452, September 2008.

[3] C. Y. Tang, Y. Guo, and J. N. Jiang, “Nonlinear dual-mode control of variable-speed wind turbines with doubly fed induction generators,” *IEEE Transactions on Control Systems Technology*, vol. 19, no. 4, pp. 744–756, July 2011.

[4] K. E. Johnson, L. Y. Pao, M. J. Balas, and L. J. Fingersh, “Control of variable-speed wind turbines: standard and adaptive techniques for maximizing energy capture,” *IEEE Control Systems Magazine*, vol. 26, no. 3, pp. 70–81, June 2006.

[5] A. D. Hansen, P. Sorensen, F. Iov, and F. Blaabjerg, “Centralised power control of wind farm with doubly fed induction generators,” *Renewable Energy*, vol. 31, no. 7, pp. 935–951, June 2006.

[6] P. B. Eriksen, T. Ackermann, H. Abildgaard, P. Smith, W. Winter, and J. M. Rodriguez Garcia, “System operation with high wind penetration,” *IEEE Power and Energy Magazine*, vol. 3, no. 6, pp. 65–74, November/December 2005.

[7] “20% wind energy by 2030—increasing wind energy’s contribution to U.S. electricity supply,” U.S. Department of Energy, Washington, DC, Tech. Rep., 2008.

[8] “System disturbance on 4 November 2006,” Union for the Co-ordination of Transmission of Electricity, Brussels, Belgium, Final report, 2007.

[9] "European wind turbine testing procedure developments," Riso National Laboratory, Roskilde, Denmark, Tech. Rep., 2001.

[10] "Controls Advanced Research Turbine (CART) commissioning and baseline data collection," National Renewable Energy Laboratory, Golden, CO, Tech. Rep., 2002.

[11] T. Thiringer and J. Linders, "Control by variable rotor speed of a fixed-pitch wind turbine operating in a wide speed range," *IEEE Transactions on Energy Conversion*, vol. 8, no. 3, pp. 520–526, September 1993.

[12] L. Y. Pao and K. E. Johnson, "Control of wind turbines: Approaches, challenges, and recent developments," *IEEE Control Systems Magazine*, vol. 31, no. 2, pp. 44–62, April 2011.

[13] K. E. Johnson, L. J. Fingersh, M. J. Balas, and L. Y. Pao, "Methods for increasing region 2 power capture on a variable-speed wind turbine," *Journal of Solar Energy Engineering*, vol. 126, no. 4, pp. 1092–1100, November 2004.

[14] E. Iyasere, M. Salah, D. Dawson, and J. Wagner, "Nonlinear robust control to maximize energy capture in a variable speed wind turbine," in *Proc. American Control Conference*, Seattle, WA, 2008, pp. 1824–1829.

[15] V. Galdi, A. Piccolo, and P. Siano, "Designing an adaptive fuzzy controller for maximum wind energy extraction," *IEEE Transactions on Energy Conversion*, vol. 23, no. 2, pp. 559–569, June 2008.

[16] R. Datta and V. T. Ranganathan, "A method of tracking the peak power points for a variable speed wind energy conversion system," *IEEE Transactions on Energy Conversion*, vol. 18, no. 1, pp. 163–168, March 2003.

[17] Q. Wang and L. Chang, "An intelligent maximum power extraction algorithm for inverter-based variable speed wind turbine systems," *IEEE Transactions on Power Electronics*, vol. 19, no. 5, pp. 1242–1249, September 2004.

[18] E. Koutroulis and K. Kalaitzakis, "Design of a maximum power tracking system for wind-energy-conversion application," *IEEE Transactions on Industrial Electronis*, vol. 53, no. 2, pp. 486–494, April 2006.

[19] K. S. M. Raza, H. Goto, H.-J. Guo, and O. Ichinokura, "A novel algorithm for fast and efficient speed-sensorless maximum power point tracking in wind energy conversion systems," *IEEE Transactions on Industrial Electronics*, vol. 58, no. 1, pp. 29–36, January 2011.

[20] M. Komatsu, H. Miyamoto, H. Ohmori, and A. Sano, "Output maximization control of wind turbine based on extremum control strategy," in *Proc. American Control Conference*, Arlington, VA, 2001, pp. 1739–1740.

[21] J. Creaby, Y. Li, and J. E. Seem, "Maximizing wind turbine energy capture using multivariable extremum seeking control," *Wind Engineering*, vol. 33, no. 4, pp. 361–388, June 2009.

[22] E. Muljadi and C. P. Butterfield, "Pitch-controlled variable-speed wind turbine generation," *IEEE Transactions on Industry Applications*, vol. 37, no. 1, pp. 240–246, January/February 2001.

[23] M. M. Hand and M. J. Balas, "Non-linear and linear model based controller design for variable-speed wind turbines," in *Proc. ASME/JSME Joint Fluids Engineering Conference*, San Francisco, CA, 1999, pp. 18–23.

[24] ——, "Systematic controller design methodology for variable-speed wind turbines," *Wind Engineering*, vol. 24, no. 3, pp. 169–187, May 2000.

[25] T. Burton, D. Sharpe, N. Jenkins, and E. Bossanyi, *Wind Energy Handbook*. New York, NY: John Wiley & Sons, 2001.

[26] A. D. Wright and M. J. Balas, "Design of state-space-based control algorithms for wind turbine speed regulation," *Journal of Solar Energy Engineering*, vol. 125, no. 4, pp. 386–395, November 2003.

[27] ——, "Design of modern controls for the controlled advanced research turbine (CART)," in *Proc. ASME Wind Energy Symposium*, Reno, NV, 2003, pp. 304–316.

[28] K. E. Johnson and L. J. Fingersh, "Adaptive pitch control of variable-speed wind turbines," *Journal of Solar Energy Engineering*, vol. 130, no. 3, pp. 1–7, August 2008.

[29] S. A. Frost, M. J. Balas, and A. D. Wright, "Direct adaptive control of a utility-scale wind turbine for speed regulation," *International Journal of Robust and Nonlinear Control*, vol. 19, no. 1, pp. 59–71, January 2009.

[30] ——, "Augmented adaptive control of a wind turbine in the presence of structural modes," in *Proc. American Control Conference*, Baltimore, MD, 2010, pp. 2760–2765.

[31] H. Geng and G. Yang, "Robust pitch controller for output power levelling of variable-speed variable-pitch wind turbine generator systems," *IET Renewable Power Generation*, vol. 3, no. 2, pp. 168–179, June 2009.

[32] A. Kumar and K. Stol, "Scheduled model predictive control of a wind turbine," in *Proc. AIAA/ASME Wind Energy Symposium*, Orlando, FL, 2009, pp. 1–18.

[33] E. A. Bossanyi, "Individual blade pitch control for load reduction," *Wind Energy*, vol. 6, no. 2, pp. 119–128, April/June 2003.

[34] ——, "Further load reductions with individual pitch control," *Wind Energy*, vol. 8, no. 4, pp. 481–485, October/December 2005.

[35] T. Larsen, H. Madsen, and K. Thomsen, "Active load reduction using individual pitch based on local blade flow measurements," *Wind Energy*, vol. 8, no. 1, pp. 67–80, January/March 2005.

[36] K. Stol, W. Zhao, and A. D. Wright, "Individual blade pitch control for the controls advanced research turbine CART," *Journal of Solar Energy Engineering*, vol. 128, no. 4, pp. 498–505, November 2006.

[37] M. Geyler and P. Caselitz, "Robust multivariable pitch control design for load reduction on large wind turbines," *Journal of Solar Energy Engineering*, vol. 130, no. 3, pp. 1–12, August 2008.

[38] K. Selvam, S. Kanev, J. W. van Wingerden, T. van Engelen, and M. Verhaegen, "Feedback-feedforward individual pitch control for wind turbine load reduction," *International Journal of Robust and Nonlinear Control*, vol. 19, no. 1, pp. 72–91, January 2009.

[39] R. Pena, J. C. Clare, and G. M. Asher, "Doubly fed induction generator using back-to-back PWM converters and its application to variable-speed wind-energy generation," *IEE Proc. Electric Power Applications*, vol. 143, no. 3, pp. 231–241, May 1996.

[40] S. Muller, M. Deicke, and R. W. De Doncker, "Doubly fed induction generator systems for wind turbines," *IEEE Industry Applications Magazine*, vol. 8, no. 3, pp. 26–33, May/June 2002.

[41] R. Datta and V. Ranganathan, "Variable-speed wind power generation using double fed wound rotor induction machine: A comparison with alternative schemes," *IEEE Transactions on Energy Conversion*, vol. 17, no. 3, pp. 414–421, September 2002.

[42] M. Tazil, V. Kumar, R. C. Bansal, S. Kong, Z. Y. Dong, and W. Freitas, "Three-phase doubly fed induction generators: an overview," *IET Electric Power Applications*, vol. 4, no. 2, pp. 75–89, February 2010.

[43] B. Hopfensperger, D. J. Atkinson, and R. A. Lakin, "Stator-flux-oriented control of a doubly-fed induction machine with and without position encoder," *IEE Proc. Electric Power Applications*, vol. 147, no. 4, pp. 241–250, July 2000.

[44] S. Peresada, A. Tilli, and A. Tonielli, "Power control of a doubly fed induction machine via output feedback," *Control Engineering Practice*, vol. 12, pp. 41–57, January 2004.

[45] L. Xu and P. Cartwright, "Direct active and reactive power control of dfig for wind energy generation," *IEEE Transactions on Energy Conversion*, vol. 21, no. 3, pp. 750–758, September 2006.

[46] D. Zhi and L. Xu, "Direct power control of DFIG with constant switching frequency and improved transient performance," *IEEE Transactions on Energy Conversion*, vol. 22, no. 1, pp. 110–118, March 2007.

[47] A. Monroy, L. Alvarez-Icaza, and G. Espinosa-Perez, "Passivity-based control for variable speed constant frequency operation of a DFIG wind turbine," *International Journal of Control*, vol. 81, no. 9, pp. 1399–1407, September 2008.

[48] J. R. Kristoffersen and P. Christiansen, "Horns Rev offshore windfarm: its main controller and remote control system," *Wind Engineering*, vol. 27, no. 5, pp. 351–360, September 2003.

[49] P. Sorensen, A. D. Hansen, K. Thomsen, H. Madsen, H. A. Nielsen, N. K. Poulsen, F. Iov, F. Blaabjerg, and B. K. Okkels, "Simulation and optimisation of wind farm controllers," in *Proc. European Wind Energy Conference and Exhibition*, London, UK, 2004, pp. 1–7.

[50] C. F. Moyano and J. A. Pecas Lopes, "An optimization approach for wind turbine commitment and dispatch in a wind park," *Electric Power Systems Research*, vol. 79, no. 1, pp. 71–79, January 2009.

[51] A. D. Hansen, P. Sorensen, F. Iov, and F. Blaabjerg, "Control of variable speed wind turbines with doubly-fed induction generators," *Wind Engineering*, vol. 28, no. 4, pp. 411–434, June 2004.

[52] R. G. de Almeida, E. D. Castronuovo, and J. A. Pecas Lopes, "Optimum generation control in wind parks when carrying out system operator requests," *IEEE Transactions on Power Systems*, vol. 21, no. 2, pp. 718–725, May 2006.

[53] J. Ekanayake and N. Jenkins, "Comparison of the response of doubly fed and fixed-speed induction generator wind turbines to changes in network frequency," *IEEE Transactions on Energy Conversion*, vol. 19, no. 4, pp. 800–802, December 2004.

[54] L. Holdsworth, J. Ekanayake, and N. Jenkins, "Power system frequency response from fixed speed and doubly fed induction generator-based wind turbines," *Wind Energy*, vol. 7, no. 1, pp. 21–35, January/March 2004.

[55] A. Mullane and M. O'Malley, "The inertial response of induction-machine-based wind turbines," *IEEE Transactions on Power Systems*, vol. 20, no. 3, pp. 1496–1503, August 2005.

[56] G. Lalor, A. Mullane, and M. O'Malley, "Frequency control and wind turbine technologies," *IEEE Transactions on Power Systems*, vol. 20, no. 4, pp. 1905–1913, November 2005.

[57] O. Anaya-Lara, F. M. Hughes, N. Jenkins, and G. Strbac, "Contribution of DFIG-based wind farms to power system short-term frequency regulation," *IEE Proc. Generation, Transmission, and Distribution*, vol. 153, no. 2, pp. 164–170, March 2006.

[58] J. Morren, J. Pierik, and S. W. H. de Haan, "Inertial response of variable speed wind turbines," *Electric Power Systems Research*, vol. 76, no. 11, pp. 980–987, July 2006.

[59] N. R. Ullah, T. Thiringer, and D. Karlsson, "Temporary primary frequency control support by variable speed wind turbines—potential and applications," *IEEE Transactions on Power Systems*, vol. 23, no. 2, pp. 601–612, May 2008.

[60] M. Kayikci and J. V. Milanovic, "Dynamic contribution of DFIG-based wind plants to system frequency disturbances," *IEEE Transactions on Power Systems*, vol. 24, no. 2, pp. 859–867, May 2009.

[61] B. G. Rawn, M. Gibescu, and W. L. Kling, "A static analysis method to determine the availability of kinetic energy from wind turbines," in *Proc. Power and Energy Society General Meeting*, Minneapolis, MN, 2010, pp. 1–8.

[62] B. K. Bose, *Modern Power Electronics and AC Drives.* Upper Saddle River, NJ: Prentice Hall, 2002.

[63] R. Fadaeinedjad, M. Moallem, and G. Moschopoulos, "Simulation of a wind turbine with doubly fed induction generator by FAST and Simulink," *IEEE Transactions on Energy Conversion*, vol. 23, no. 2, pp. 690–700, June 2008.

[64] Y. Lei, A. Mullane, G. Lightbody, and R. Yacamini, "Modeling of the wind turbine with a doubly fed induction generator for grid integration studies," *IEEE Transactions on Energy Conversion*, vol. 21, no. 1, pp. 257–264, March 2006.

[65] F. D. Bianchi, H. De Battista, and R. J. Mantz, *Wind Turbine Control Systems: Principles, Modelling, and Gain Scheduling Design.* London, England: Springer, 2007.

[66] H. K. Khalil, *Nonlinear Systems*, 3rd ed. Upper Saddle River, NJ: Prentice Hall, 2001.

[67] C.-T. Chen, *Linear System Theory and Design*, 3rd ed. New York, NY: Oxford University Press, 1999.

[68] S. Heier, *Grid Integration of Wind Energy Conversion Systems*, 2nd ed. West Sussex, England: John Wiley & Sons, 2006.

[69] W. L. Brogan, *Modern Control Theory*, 3rd ed. Upper Saddle River, NJ: Prentice Hall, 1991.

[70] L. Ljung, *System Identification: Theory for the User*, 2nd ed. Upper Saddle River, NJ: Prentice Hall, 1999.

[71] K. Narendra and P. Gallman, "An iterative method for the identification of nonlinear systems using a Hammerstein model," *IEEE Transactions on Automatic Control*, vol. 11, no. 3, pp. 546–550, July 1966.

[72] P. C. Krause, O. Wasynczuk, and S. D. Sudhoff, *Analysis of Electric Machinery and Drive Systems*, 2nd ed. Piscataway, NJ: Wiley-IEEE Press, 2002.

[73] R. G. de Almeida and J. A. Pecas Lopes, "Participation of doubly fed induction wind generators in system frequency regulation," *IEEE Transactions on Power Systems*, vol. 22, no. 3, pp. 944–950, August 2007.

[74] L.-R. Chang-Chien and Y.-C. Yin, "Strategies for operating wind power in a similar manner of conventional power plant," *IEEE Transactions on Energy Conversion*, vol. 24, no. 4, pp. 926–934, December 2009.

[75] L.-R. Chang-Chien, W.-T. Lin, and Y.-C. Yin, "Enhancing frequency response control by DFIGs in the high wind penetrated power systems," *IEEE Transactions on Power Systems*, vol. 26, no. 2, pp. 710–718, May 2011.

[76] H. T. Ma and B. H. Chowdhury, "Working towards frequency regulation with wind plants: combined control approaches," *IET Renewable Power Generation*, vol. 4, no. 4, pp. 308–316, July 2010.

[77] Y. Guo, S. H. Hosseini, J. N. Jiang, C. Y. Tang, and R. G. Ramakumar, "Voltage/pitch control for maximization and regulation of active/reactive powers in wind turbines with uncertainties," *IET Renewable Power Generation*, vol. 6, no. 2, pp. 99–109, March 2012.

[78] H. Li, K. L. Shi, and P. G. McLaren, "Neural-network-based sensorless maximum wind energy capture with compensated power coefficient," *IEEE Transactions on Industry Applications*, vol. 41, no. 6, pp. 1548–1556, November/December 2005.

[79] B. Beltran, T. Ahmed-Ali, and M. El Hachemi Benbouzid, "Sliding mode power control of variable-speed wind energy conversion systems," *IEEE Transactions on Energy Conversion*, vol. 23, no. 2, pp. 551–558, June 2008.

[80] N. W. Miller, J. J. Sanchez-Gasca, W. W. Price, and R. W. Delmerico, "Dynamic modeling of GE 1.5 and 3.6 MW wind turbine-generators for stability simulations," in *Proc. PES General Meeting*, Toronto, Canada, 2003, pp. 1977–1983.

[81] W. Qiao, W. Zhou, J. M. Aller, and R. G. Harley, "Wind speed estimation based sensorless output maximization control for a wind turbine driving a DFIG," *IEEE Transactions on Power Electronics*, vol. 23, no. 3, pp. 1156–1169, May 2008.

[82] E. F. Camacho and C. B. Alba, *Model Predictive Control*, 2nd ed. London, England: Springer, 2007.

[83] J. Shamma, *Cooperative Control of Distributed Multi-Agent Systems.* Chichester, England: John Wiley & Sons, 2008.

[84] S. Ching, Y. Eun, C. Gokcek, P. T. Kabamba, and S. M. Meerkov, *Quasilinear Control: Performance Analysis and Design of Feedback Systems with Nonlinear Sensors and Actuators.* New York, NY: Cambridge University Press, 2010.

[85] G. Tapia, A. Tapia, and J. X. Ostolaza, "Proportional-integral regulator-based approach to wind farm reactive power management for secondary voltage control," *IEEE Transactions on Energy Conversion*, vol. 22, no. 2, pp. 488–498, June 2007.

[86] P. Li, P.-K. Keung, and B.-T. Ooi, "Development and simulation of dynamic control strategies for wind farms," *IET Renewable Power Generation*, vol. 3, no. 2, pp. 180–189, June 2009.

[87] J. A. Rossiter, *Model-Based Predictive Control: A Practical Approach.* Boca Raton, FL: CRC Press, 2003.

[88] K. J. Astrom and B. Wittenmark, *Adaptive Control*, 2nd ed. Upper Saddle River, NJ: Prentice Hall, 1994.

[89] B. G. Brown, R. W. Katzand, and A. H. Murphy, "Time series models to simulate and forecast wind speed and wind power," *Journal of Applied Meteorology*, vol. 23, no. 8, pp. 1184–1195, August 1984.

[90] C. Monteiro, R. Bessa, V. Miranda, A. Boterrud, J. Wang, and G. Conzelmann, "Wind power forecasting: State-of-the-art 2009," Argonne National Laboratory, Argonne, IL, Technical Report, 2009.

[91] G. Giebel, R. Brownsword, and G. Kariniotakis, "The state of the art in short-term prediction of wind power: A literature overview," Online.

[92] S. Boyd and L. Vandenberghe, *Convex Optimization.* New York, NY: Cambridge University Press, 2004.

[93] H. Kwakernaak and R. Sivan, *Linear Optimal Control Systems.* New York, NY: Wiley-Interscience, 1972.

[94] P. M. Anderson and M. Mirheydar, "A low-order system frequency response model," *IEEE Transactions on Power Systems*, vol. 5, no. 3, pp. 720–727, August 1990.

[95] P. Kundur, *Power System Stability and Control*, 1st ed. Columbus, OH: McGraw-Hill, 1994.

[96] S.-J. Huang and C.-C. Huang, "An adaptive load shedding method with time-based design for isolated power systems," *International Journal of Electrical Power and Energy Systems*, vol. 22, no. 1, pp. 51–58, January 2000.

[97] D. L. H. Aik, "A general-order system frequency response model incorporating load shedding: Analytic modeling and applications," *IEEE Transactions on Power Systems*, vol. 21, no. 2, pp. 709–717, May 2006.

[98] I. Egido, F. Fernandez-Bernal, P. Centeno, and L. Rouco, "Maximum frequency deviation calculation in small isolated power systems," *IEEE Transactions on Power Systems*, vol. 24, no. 4, pp. 1731–1738, November 2009.